



THE HONG KONG  
POLYTECHNIC UNIVERSITY

香港理工大學

Pao Yue-kong Library

包玉剛圖書館

---

## Copyright Undertaking

This thesis is protected by copyright, with all rights reserved.

**By reading and using the thesis, the reader understands and agrees to the following terms:**

1. The reader will abide by the rules and legal ordinances governing copyright regarding the use of the thesis.
2. The reader will use the thesis for the purpose of research or private study only and not for distribution or further reproduction or any other purpose.
3. The reader agrees to indemnify and hold the University harmless from and against any loss, damage, cost, liability or expenses arising from copyright infringement or unauthorized usage.

If you have reasons to believe that any materials in this thesis are deemed not suitable to be distributed in this form, or a copyright owner having difficulty with the material being included in our database, please contact [lbsys@polyu.edu.hk](mailto:lbsys@polyu.edu.hk) providing details. The Library will look into your claim and consider taking remedial action upon receipt of the written requests.

*The Hong Kong Polytechnic University*  
**mechanical engineering**



**Broadband Wave Reflection by  
Fluid-Plate Interaction**

Jun Han

A thesis submitted in partial fulfilment of the requirements for  
the Degree of Master of Philosophy at  
The Hong Kong Polytechnic University

Department of Mechanical Engineering

September, 2005

## **Acknowledgements**

I would like to express my heartfelt thanks and appreciation to my supervisor, Dr. Huang, who guides me into my research area of acoustics during my MPhil studies, and lets me know what research is all about. His kindness, patience, encouragement and support make this thesis possible. Without his generous help during the past two years, the project cannot be finished. During the past two years, I experienced the transfer from an undergraduate to a postgraduate with a comprehension about what characteristics a researcher should have, and it has a great influence on my future academic exploration.

I would also like to thank Dr. YS Choy, for her kindly help and support during the past two years.

Finally, I am forever indebted to my parents for their unconditional understanding, endless patience and encouragement when required. Without their sacrifice, support and deep love, I cannot successfully finish my former studies and pursue further education.

## **Certificate of Originality**

I hereby declare that this thesis is my own work and that, to the best of my knowledge and belief, it reproduces no material previously published or written, nor material that has been accepted for the award of any other degree or diploma, except where due acknowledgement has been made in the text.

---

Jun Han

## Table of Contents

<b>ACKNOWLEDGEMENTS.....</b>	<b>I</b>
<b>CERTIFICATE OF ORIGINALITY .....</b>	<b>II</b>
<b>TABLE OF CONTENTS.....</b>	<b>III</b>
<b>ABSTRACT .....</b>	<b>VI</b>
<b>LIST OF FIGURES .....</b>	<b>IX</b>
<b>CHAPTER 1: INTRODUCTION .....</b>	<b>1</b>
1.1 INTRODUCTION TO NOISE SOURCES .....	1
1.2 NOISE CONTROL METHODS.....	2
1.2.1 Dissipative noise control method: .....	3
1.2.2 Reactive noise control method .....	4
1.2.3 Active noise control method .....	6
1.3 DRUMLIKE SILENCER.....	7
1.4 RATIONALE OF USING PLATE TO REPLACE MEMBRANE .....	10
1.5 LITERATURE SURVEY ON VIBROACOUSTICS .....	12
1.6 LITERATURE SURVEY ON PLATE SILENCERS .....	19
1.6.1 Active noise control .....	20
1.6.2 Passive noise control .....	21
<b>CHAPTER 2: REAL-PLATE MODEL IN TWO-DIMENSIONS.....</b>	<b>28</b>

---

---

2.1 INTRODUCTION .....	28
2.2 MINDLIN-PLATE MODEL .....	30
2.2.1 THE THEORETICAL MODEL .....	30
2.2.2 IMPLEMENTATION IN THE FINITE ELEMENT METHOD .....	37
2.2.3 RESULTS .....	44
2.3 PLANE-STRESS MODEL .....	47
2.3.1 PLANE-STRESS MODEL VS PLANE-STRAIN MODEL .....	47
2.3.2 THE THEORETICAL MODEL .....	49
2.3.3 RESULTS .....	50
2.4 NON-UNIFORM PLATE MODEL .....	52
2.5 MODAL ANALYSIS .....	63
2.5.1 THE SIMPLY-SUPPORTED UNIFORM PLATE .....	63
2.5.2 THE CLAMPED NON-UNIFORM PLATE .....	75
<b>CHAPTER 3: THREE-DIMENSIONAL EFFECTS .....</b>	<b>78</b>
3.1 INTRODUCTION .....	78
3.2 CLAMPED LATERAL EDGES .....	82
3.2.1 UNIFORM THICKNESS IN THE LATERAL DIRECTION .....	82
3.2.2 NON-UNIFORM THICKNESS IN THE LATERAL DIRECTION .....	91
3.3 CORRUGATED PLATE .....	94
<b>CHAPTER 4: CHOICE OF PLATE MATERIAL &amp; STRUCTURE .....</b>	<b>98</b>
4.1 INTRODUCTION .....	98

---

---

4.2 DETERMINATION OF MATERIAL PROPERTIES .....	99
4.2.1 Static method .....	99
4.2.2 Dynamic method .....	101
4.3 ACOUSTIC MEASUREMENT .....	105
4.4 EXPERIMENTAL RESULTS .....	111
4.4.1 Two-dimensional model .....	111
4.4.2 Three-dimensional model .....	118
4.5 RESULTS FOR HONEYCOMB STRUCTURE .....	122
4.5.1 Choice of plate material/structure .....	122
4.5.2 Implementation in experiment .....	128
<b>CHAPTER 5: CONCLUSIONS AND FUTURE WORK .....</b>	<b>132</b>
5.1 CONCLUSIONS .....	132
5.2 FUTURE WORK .....	135
<b>REFERENCES .....</b>	<b>136</b>

## **Abstract**

Sound reflection is a very useful tool to control low to medium frequency noise in a duct. Recently, a device utilizing the full interaction between a tensioned membrane and sound is introduced to achieve broadband sound reflection. The membrane is backed by a rigid-walled cavity external to the duct to prevent breakout noise. The performance of this device, called drum-like silencer, has been thoroughly characterized and tested. Before the device can be applied in engineering use, two technical problems emerge: one is the difficulty to apply the required high tension on a thin membrane whose edges are slippery, and the other is that the tension may also vary with environmental temperature. To overcome these problems, it is proposed that the membrane is replaced by a light and yet stiff plate, which relies on its bending stiffness to restore structural equilibrium instead of the applied tensile force. The new prototype is called a plate silencer. The plate silencer is shown, theoretically, to have even better performance than the drum-like silencer. Literature survey shows that the use of a plate as a side-branch sound reflector is novel, and the present thesis reports the full numerical study using finite element and preliminary experimental study of the new device.

To analyse the performance of the plate-type wave reflector, a coupled two-dimensional system, including an acoustic domain and a structural-mechanics domain, is introduced. Two different models, mindlin-plate model and the plane-stress model, are used to simulate the plate with various boundary conditions. A comparison between the results of different boundary conditions shows that a simply-supported boundary condition has a better performance than the clamped boundaries since the former allows more freedom for the plate to respond to incident sound. However, it is difficult to achieve a simply-supported boundary condition in practice. A non-uniform plate in which the thickness is reduced at the clamped ends is used to approximate the design of simply-supported uniform plate. The finite element simulation shows that, by changing the length of the two thinner ends, four peaks appear in the spectrum of the transmission loss, and they are well connected producing a wide stopband. Modal analysis has been conducted for both the simply-supported uniform plate and the clamped non-uniform plate. Typically, spectral peaks appear at the frequency where there is no interference between the even modes and the odd modes of the in-vacuo plate vibration. The energy flux of the sound reflected by the odd modes is simply added to that from the even modes.

The above model is two dimensional for both the acoustics in air and the plate, which is in fact a beam. In reality, such model can only be implemented by a three dimensional plate with a very small gap between the plate and the lateral duct walls. Further numerical simulation is conducted for the leakage effect of the gap.

The result shows that, if the gap size is smaller than about 0.5% of the duct width, the effect on the transmission loss is insignificant. The study also shows that the performance deteriorates drastically if a three dimensional plate is used with all edges fixed.

Experimental studies for both two-dimensional and three-dimensional models are conducted to validate the theoretical results. The methods used for the transmission loss measurement and the material property quantification are described. In the experiment, a 3mm-thick uniform foam plate is used. This plate does not conform to the optimal parameters predicted by the theory, but the experimental results do validate the theoretical findings corresponding to the actual material properties. It is hoped that, when the optimal material and structural properties are found, the broadband transmission loss spectrum can be realized for the device.

## List of Figures

Figure 1. 1:	Theoretical model of drumlike silencer .....	8
Figure 2. 1:	Configuration of a plate-type wave reflector with simply-supported uniform plates.....	31
Figure 2. 2:	The configuration of the geometry .....	33
Figure 2. 3:	A stacked view of the transmission loss spectra of simply-supported plate-type wave reflector with different bending stiffness.....	45
Figure 2. 4:	The comparison between the performances of the simply-supported uniform plates with (a) $m=0$ and (b) $m=1$ .....	47
Figure 2. 5:	Comparison between the results of the plane stress model and the mindlin plate model with the same parameter $m=1$ , $E=6550$ .....	50
Figure 2. 6:	The comparison between the optimal performances of a clamped uniform plate model ( $E=6550$ ) and a simply-supported plate model ( $E=12480$ ) with the same mass ratio $m=1$ . .....	52
Figure 2. 7:	Configuration of a non-uniform plate.....	53
Figure 2. 8:	The first three mode shape of the non-uniform plate with $L_1=3$ and $h_b=0.015$ .....	54
Figure 2. 9:	Effect of the length of the middle part on optimal bending stiffness and silencer bandwidth when mass ratio=1. ....	56
Figure 2. 10:	Transmission loss spectra of the non-uniform plate with $L_1=4.0, 3.8, 3.4, 3.2$ , and the same dimensionless density $\rho=20$ .....	57
Figure 2. 11:	The normalized error spectrum of the numerical model for a non-uniform plate .....	60
Figure 2. 12:	Comparison about the optimal performance between the simply-supported uniform plate and the clamped non-uniform plate ( $L_1=3.4$ ), both of which have the same mass ratio $m=0.776$ . The solid line is the result of the	

---

clamped non-uniform plate with $L_1=3.4$ , and the dotted line is that of the simply-supported uniform plate.....	61
Figure 2. 13: Effect of the mass ratio on optimal bending stiffness and silencer bandwidth.....	62
Figure 2. 14: Modal reflections. The first column is the modal amplitude $ V_j $ , the second column is the modal reflection coefficient $ R_j $ , the third column is the single mode reflection $ V_j R_j $ , and the last column is the modal contribution $\gamma_j$ . The top row is the TL spectrum as a reference of some important frequencies. ....	64
Figure 2. 15: Transmission loss spectrum of the simply-supported plate with $m=1$ & $D=0.13$ .....	69
Figure 2. 16: The response of the plate at the first peak $f_1=0.038$ , P1. (a) shows the velocity amplitude of each mode, $ V_j $ . (b) is the amplitude of the modal reflection coefficient $ R_j $ . (c) is the sound reflection by each mode alone, $ R_j V_j $ . (d) shows how the complex modal contributions add up. (e) is the real and imaginary parts of the plate vibration velocity distribution, $V(x)$ .....	70
Figure 2. 17: The response of the plate at the second peak.....	72
Figure 2. 18: The response of the plate at the third peak $f_3=0.122$ .....	73
Figure 2. 19: Relationships between the peak positions in the transmission loss spectra and the interference between the even modes and odd modes .....	74
Figure 2. 20: The comparisons of the vibration velocity distributions at the peak points between the clamped non-uniform plate (the left column, from (a) to (d)) and the simply-supported uniform plate (the right column, from (e) to (g)). .....	76
Figure 3. 1: The configuration of a three-dimensional plate-type wave reflector with two identical bending stiffness plates. Each cavity has a length of $L$ , depth $h_c$ and width $w$ .....	78
Figure 3. 2: Top view the non-uniform plate and the duct with a gap of specified dimensions $\tau$ between them.....	79

---

Figure 3. 3:	Configuration of the non-uniform plate with non-uniform thickness along the longitudinal direction and uniform thickness in the lateral direction....	83
Figure 3. 4:	Illustrations of the unstructured mesh method (a) and extruded mesh method (b) .....	85
Figure 3. 5:	The optimal transmission loss spectra with the changing length of the middle part $L_1$ .....	89
Figure 3. 6:	The comparisons between the transmission loss spectra with the changing length of the middle part $L_1$ under the dimensionless bending stiffness $D=0.001$ .....	90
Figure 3. 7:	Configuration of the non-uniform plate with non-uniform thickness along both the longitudinal and lateral directions .....	91
Figure 3. 8:	The stacked view of the optimal transmission loss spectra with the changing length of the middle part $L_1$ .....	92
Figure 3. 9:	Comparison between the plates with 2 thinner edges (solid line) and with 4 thinner edges (dotted line).....	94
Figure 3. 10:	Configuration of a sinusoidal corrugated plate.....	95
Figure 4. 1:	The configuration of the experimental setup .....	99
Figure 4. 2:	Relationship between the applied loading and extension.....	100
Figure 4. 3:	(a): Experiment setup of the vibration testing using laser vibrometer, and (b) is the configuration of the 3mm-thick foam with two testing points.....	102
Figure 4. 4:	Natural frequencies of the 3mm-thick foam with two fixed ends	103
Figure 4. 5:	The first two <i>in vacuo</i> modes of the 3mm-thick foam plate when $E = 54.4MPa$ .....	104
Figure 4. 6:	The set-up for the standing wave decomposition and the two-load method.....	106
Figure 4. 7:	The set-up of the Experiment .....	108

---

---

Figure 4. 8:	A comparison about the TL curve between the simulation result and the experiment result (a), and the measured absorption coefficient of the expansion chamber (b) .....	110
Figure 4. 9:	Comparisons between the simulation result and experimental result of two-dimensional model using 3mm-thick uniform foam plate. The open circles are the measured data, and the solid line is the simulation result .....	113
Figure 4. 10:	Experiment setup of the vibration testing using laser vibrometer	115
Figure 4. 11:	The response of the plate along the longitudinal direction. The left column is the response at the first peak frequency, and the right column is the response at the second peak frequency. ....	116
Figure 4. 12:	The response of the plate along the lateral direction. The first row is the response at the first peak frequency, and the second row is the response at the second peak frequency .....	117
Figure 4. 13:	Comparisons between the simulation result and experimental result of three-dimensional model using 3mm-thick uniform foam plate. The open circles are the measured data, and the solid line is the simulation result.....	119
Figure 4. 14:	The response of the plate along the longitudinal direction. The first column is the response at the first peak frequency, and the second column is the response at the second peak frequency. ....	120
Figure 4. 15:	The response of the plate along the longitudinal direction. The left column is the response at the first peak frequency, and the right column is the response at the second peak frequency. ....	121
Figure 4. 16:	The Load-extension curve of the Nomex honeycomb structure of 5mm thick.....	125
Figure 4. 17:	Load-extension Curve of Nomex honeycomb structure of 10mm thick.....	126
Figure 4. 18:	The configuration and dimensions of the non-uniform honeycomb structure.....	129
Figure 4. 19:	The experimental results of a two-dimensional model using a non-uniform honeycomb structure. ....	130

---

## **Chapter 1: Introduction**

### ***1.1 Introduction to noise sources***

Acoustic noise problems become more and more evident as increased numbers of large industrial equipment such as engines, blowers, fans, transformers, and compressors are in use. In addition, the growth of high-density housing increases the exposure of the population to noise from a variety of sources. Furthermore, cost constraints have resulted in a tendency to use lighter materials for buildings and transportation equipment, which also results in an increase in environmental noise. Acoustic noise needs not be limited to air; underwater or hydroacoustic noise is a problem in certain marine settings and could also arise in laboratory instruments and ultrasonic medical scanning applications. Mechanical vibration is another related type of noise that commonly creates problems in all areas of transportation and manufacturing, as well as with many household appliances.

For a long time, duct acoustics is an area of continuous interest for its theoretical and practical importance. Nowadays, the noises of engines, turbomachinery, wind tunnels, ventilation systems, public halls and transport tunnels keep increasing. This calls for our better understanding of the propagation of complex noise sources and effective techniques for their prediction and abatement under realistic conditions.

---

Generally speaking, the noise sources can be divided into three kinds: structure vibration, pressure change on structures and turbulence. This division is made from the physical perspective. Mathematically, the noise sources can also be divided into three categories: monopole, dipole and quadrupole. For example, fan noise comes from the unsteady flow features, which is dipole in nature, and it can also be caused by vibrations, which are caused by the unbalance or friction of the rotating parts in the machine.

Typical duct noise is dominated by low-frequency noise, whose wavelength is larger than typical ventilation duct cross section. Low-frequency noise is very annoying and difficult to control. Various methods have been developed to reduce it. In the following section, we will make a general description about some basic mechanisms of noise control methods.

## ***1.2 Noise control methods***

The traditional approach to acoustic noise control uses passive techniques such as enclosures, barriers, and silencers to attenuate the undesired noise. Passive silencers either use the energy loss caused by sound propagation in a duct lined with sound-absorbing material to provide the silencing (resistive silencers), or use the concept of impedance change caused by a combination of baffles and tubes to

---

silence the undesired sound (reactive silencer). The former method is the dissipative noise control method, and the latter method is the reactive noise control method, although they normally function together.

With the development of electronics and computers, active noise control (ANC), which involves an electroacoustic or electromechanical system, is used as an additional control method. Acoustic ANC is developing rapidly because it permits improvements in noise control, often with potential benefits in size, weight, volume, and cost. In addition, noise may be reduced at the listener's position without physical modification or rearrangement of existing noise sources. We will describe these control methods in details.

### ***1.2.1 Dissipative noise control method:***

Dissipative control method tends to be independent of the effects of source and the termination impedance, by the very nature of the mode of operation. It is generally favored for the attenuation of high frequency noise, due to its simple and cheap construction and great effectiveness over a broad frequency range.

Owing to the acting sound pressure, the air molecules, in addition to their random thermal motion, oscillate in the interstices of a porous material with the frequency of the exciting sound wave. The oscillations result in frictional losses. Changes in flow direction and expansions and contractions of the flow through irregular pores

---

result in loss of momentum in the direction of wave propagation. These two phenomena account for most of the energy losses at high frequencies. At low frequencies, heat conduction is another source for the energy loss, but the performance is generally low.

In the recent years, there have been a wide variety of applications of dissipative noise control in many commercial and industrial services. For examples: elementary absorbers, lined ducts and dissipative silencers. However, they are relatively large, costly, and ineffective at low frequencies. The attenuation of passive silencers is low when the acoustic wavelength is large compared to the silencer dimensions, such as body length or lining thickness. Furthermore, these silencers often create an undesired backpressure of considerable magnitude if there is airflow in the duct. What's more, it also has environmental problems as fibers exposed to flow trap dusts.

### ***1.2.2 Reactive noise control method***

Reactive noise control is another passive noise control. This method is based upon reflection or source sound power output suppression, and makes use of impedance discontinuities, such as an expansion chamber and Helmholtz resonator, to reflect sound. In reality, it is shown that reactive devices are favored for the control of medium frequency noise as they tend to be more compact than dissipative devices

to achieve the same attenuation. Similarly, reactive noise control has the same benefits as that of dissipative one—easy to control and cheap in cost.

However, it is also found that there are some drawbacks in the reactive noise control. When the frequency is too low, the length required of a reactive device, such as the expansion chamber, becomes too large. And when the frequency is too high, the high order modes make reflection less effective and the design rather difficult. Furthermore, passband is also a problem in the expansion chamber. Here, passband is defined as a frequency range in which the transmission loss ( $TL$ ) is zero or low. Passband exists in reactive silencer such as the expansion chamber.

Vibration problems are another area where passive techniques have limitations. Passive vibration control is achieved by spring-mass-damper decoupling, which is the mechanical analog of a lowpass filter. The resonant frequency, below which vibrational isolation is ineffective, is inversely proportional to the square root of the spring compliance and the mass. Thus, with the frequency of interest decreasing, the mass or compliance must increase, eventually becoming impractical or too expensive to implement. Therefore, like acoustic noise, the effectiveness of passive vibration noise control techniques is limited at low frequencies.

### **1.2.3 Active noise control method**

Active noise control (ANC) is becoming more and more popular owing to the rapid development of electronic technology during these years. Basically speaking, ANC is achieved by introducing a canceling “antinoise” wave through an appropriate array of secondary sources. These secondary sources are interconnected through an electronic system using a specific signal processing algorithm for the particular cancellation scheme. It involves an electroacoustic or electromechanical system that cancels the primary (unwanted) noise based on the principle of superposition.

The amount of primary-noise cancellation depends on the accuracy of the amplitude and phase of the generated antinoise. The ANC system efficiently attenuates low-frequency noise where passive methods are either ineffective or very expensive or bulky. Thus, application of the ANC technique is a modern supplement to conventional passive systems.

Notwithstanding its benefits, the drawbacks of the active noise control cannot be neglected. Many modern ANC systems rely heavily on signal processing with fewer electroacoustic or electromechanical elements and an increasing number of elaborate adaptive filtering schemes. However, if the physical arrangement is not properly organized, the digital signal processing may not be able to compensate for the shortcomings, and the system can fail. What’s more, the range of noise control problems that can be solved by means of an active system is still rather limited;

---

only noise at relatively low frequencies can be effectively attenuated by such methods. All of the drawbacks make the active noise control not a good method to be widely used.

According to the three noise control methods, a variety of silencers have been developed. In the next section, a drumlike silencer, which is based on passive mechanism, is introduced.

### **1.3 Drumlike silencer**

An ideal silencer in either exhaust system or air conditioning system has to allow a free air passage without extensive pressure loss while reducing the noise as much as possible. Pressure loss always leads to the need for higher power consumption and higher cost, and the higher power also leads to extra noises from the flow driving system. Therefore, side-mounting silencer without insertion of any splitter in the middle of the main duct, namely a flow-through silencer, would be an ideal configuration for noise control.

As mentioned above, reflection can be caused by any discontinuity boundary. Apart from cross sectional area change, the alternation of density and phase speed can also constitute a discontinuity condition. Basing on this mechanism, during the past years, Huang and Choy (1999, 2000, 2002, 2004) have conducted many

---

research projects on this topic, and developed a passive noise control method by using tensioned membranes on the duct wall. The drumlike silencer is characterized as active adaptation of a passive control and shows a good performance in reducing the low-frequency duct noise. It mainly makes use of the appropriate interactions between sound and flexible panels sandwiched in the rigid duct walls, as shown in Figure 1. 1.

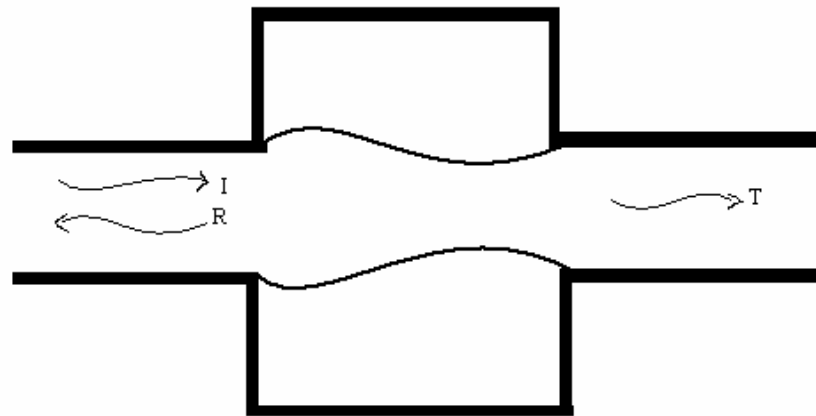


Figure 1.1: Theoretical model of drumlike silencer

Noise reduction is achieved by the combination of two basic mechanisms: wave reflection of the panel and the damping of excited flexural waves by the membrane viscosity. First, when waves travel in a passage with considerable cross section dispensability, fluid compressibility gives way to wall compliance as the main mechanism controlling the pace of wave propagation (Lighthill, 1978), and a wave speed ( $c$ ) much less than the isentropic speed of sound in free space ( $c_0$ ) ensues.

The change of wave speed from  $c_0$  to  $c \ll c_0$  leads to substantial wave scattering and reflection at the panel where the duct cross sections remain constant.

In this section, we introduce the drumlike silencer. This silencer can achieve the low-frequency noise reduction, and the frequency bandwidth is wide. However, there are still also some unsatisfactory aspects of the drumlike silencer. Because the thickness of the membrane is very small, it is difficult to install. As a special parameter in the drumlike silencer, discussed in the study of (Choy & Huang, 2002), the tension is also a difficult parameter to fix. It's also difficult to control the tension. We cannot easily adjust and maintain the tension to our desired value. Besides, the device of tension-controlling system is very complicated, but, if we cannot correctly adjust and keep the tension, the performance of the drumlike silencer will be greatly reduced. This also increases the difficulty of the installation and maintenance. Besides, the tension may vary with temperature and membrane relaxation. These drawbacks mean that the drumlike silencer can only be localized in limited places, and is difficult to be widely used in the practical applications.

Because there are some drawbacks of the drumlike silencer, we design another type of silencer-panel wave reflector, which has more practical and simpler operation structure. In the following section, we will describe the plate-type wave reflector.

## **1.4 Rationale of using plate to replace membrane**

The plate-type wave reflector is an idea derived from the drumlike silencer. One of the differences of the two silencers is that surfaces whose stiffness is negligible compared with the restoring force due to tension are called membranes; while, when the stiffness is the important factor, the structure is called plates. Their mechanisms are similar to each other, both making use of the wave reflection mechanism. From the perspective of acoustic energy conservation, the mechanism can be explained as follows: when the plate vibrates, it radiates sound in two directions. The part travelling to the upstream, where incident sound comes from, is identified as reflection waves. The part travelling downstream will combine with the incident wave and form the transmitted wave. The energy flux of the incident waves is equal to the sum of those of the reflected waves and the transmitted waves. Whenever there are reflected waves, the energy flux of the transmitted waves is reduced, thus achieving the purpose of noise reduction.

To further comprehend the advantages of the plate-type wave reflector, we will make a comparison between three kinds of silencers: drumlike silencer, plate-type wave reflector, and expansion chamber, which can be imagined as a drumlike silencer with membrane replaced by an air layer. Under the excitation of the incident waves, the membrane, plate and air layer vibrate in different mode shapes. Among the different order modes, higher order modes are less effective in

reflecting sound than the lower order modes as waves radiated by most parts of the surface simply cancel themselves out. In fact, the first mode has the best performance in sound reflection. When the covering is excited and vibrates in the first mode, there are no reflected waves cancelled; while, when the covering vibrates in the second mode, the reflected waves from the upstream part of the membrane and the downstream part of the membrane will largely cancel each other, and less reflected waves survive, and the same thing happens to the higher order modes. Therefore, the domination of the lower order modes is preferable. It has to be pointed out that, although the first mode is the most effective mode for the membrane/plate radiation efficiency, it is hard to excite as it is prohibited by the cavity stiffness.

With this conclusion, it is found that the expansion chamber has the worst performance in noise reflection among the three silencers. For an expansion chamber, it can be imagined that there is an air layer covering the cavity. Because the air layer has no tension, nor bending stiffness. When it is excited by the incident waves, it will follow the modes of the incident waves. Therefore, it will easily vibrate in higher order modes, and cannot produce much reflected wave. While for the tensioned membrane, the tension plays the role of a restoring force, and it can vibrate in lower order modes, and hence can efficiently reflect waves. For the plate, its bending stiffness plays the role of structural restoring force. Similarly, lower order modes are promoted and good performance of wave

---

reflection occurs at low frequencies. The fact that the plate type reflector performs better than the membrane type is later explained as a result of better interaction between the reflection waves caused by the odd modes and that caused by the even modes.

During the past years, researchers have also conducted many researches on vibrating plates. These researches can be generally divided into two categories: plate vibroacoustics and plate silencers. The plate vibroacoustics mainly investigates the properties of the sound field induced by plate, and the plate silencers mainly focus on developing new kinds of silencers using plates, basing on various noise control mechanisms. In the next two sections, a literature survey about these two categories is made.

### ***1.5 Literature survey on vibroacoustics***

To find effective methods to reduce the noises from different sources with different frequencies, an accurate understanding about the sound field induced by different sources is needed. Many experiments have been done to get a clear comprehension about the sound field, and plates are often used in the experiments, although they play different roles in these researches. Some researchers focus on the sound field radiated by the plates; some researchers are interested in the characteristics of the

---

plates when they are excited by waves, and others were interested in the effects of the plates in sound transmission. A few are described below.

Cheng (1994) investigates the coupling of sound with cylindrical shells simulating aircraft cabins, the purpose being to identify the noisiest structural modes in the cabin. In his study, he presents a theoretical study of a plate-ended circular cylindrical shell radiating sound into its enclosed cavity, and a general formulation considering the full coupling between the subsystems (plate, shell and cavity) is developed. The structure vibration and the generated sound field inside the cavity are presented. His model is a free vibration model in which full coupling between the shell and the plate as well as the coupling of the whole mechanical envelope with the acoustic medium are considered. The purpose is to obtain a deep understanding of the coupling phenomena, which is a key factor to understand the mechanism of the mechanical energy transfer between the plate and the shell and mechanical-acoustical energy transfer from the structure to the acoustic medium.

Considering the elevated structure noise in room acoustics, an experiment is conducted (Sakagami, 1997) on the steel plate girders, the main source of the elevated structure noise. A radiated sound field generated by a baffled elastic plate strip of infinite length is studied, which is the simplest model of the web of a steel plate girder. To learn the properties of the sound radiation from a baffled elastic plate strip of infinite length, three kinds of possible concentrated forces, a line

---

force, a point force, and a concentrated moment, are used. The noise radiated by the plate has the main component in the audio-frequency range, with maximum at mid-high frequencies (500-1kHz).

Another similar research is conducted (Yairi, 2002) about the sound radiation from a double-leaf elastic plate subjected to a point force excitation. It is an investigation about the structure-borne noise in building elements, and is to gain a fundamental insight into the sound radiation from an interior panel of a double-leaf structure in buildings. Due to the mass-air-mass resonance, the effects of the interior panel on the sound radiation show a negative effect at low frequencies. It is useful for predicting the sound radiation due to the structure-borne sound in building elements.

Michishita (2000) studied the sound field radiated by an infinitely long elastic plate strip in contact with a vertical reflecting surface. His main interest in this study is to clarify the effect of a concrete slab on the radiated sound field from a steel plate girder.

Howe (1994) showed in his study that the sound and vibration produced by low Mach number turbulence flow over the edge of a coated region of an elastic plate. The coating is idealized as a semi-infinite pressure release surface on one side of a thin, infinite plate, and the configuration may be regarded as modeling interactions

---

occurring in a mean flow duct. Particular attention is given to the case of heavy fluid loading, which occurs in underwater applications.

There are also some studies on the resonance with plates. Abe *et al.* (1998) studied the subharmonic resonance of simply-supported, rectangular laminated plates by the method of multiple scales. They present a remedy for solving the subharmonic resonance of moderately thick laminated plates by the MMS. Taking into account the first order shear deformation theory and the von Karman-type geometric non-linear theory, the governing equations for antisymmetric angle-ply laminated plates are derived by Hamilton's principle. Then, applying Galerkin's procedure, the governing equations are reduced to the Duffing-type equation in terms of the transverse displacement. Finally, steady-state solutions for the subharmonic resonance are obtained by using the MMS, where they suggest a new definition of a detuning parameter to apply it properly.

In the research of Tu and Fuller (2000), experiment is conducted on sound transmission through a vibrating plate. The plate is excited by two distinctive noise sources. One is acoustical disturbance from a large speaker, while the other is the structural disturbance from a piezoelectric ceramic transducer mounted on the plate. The secondary control source acting on the plate is another piezoelectric actuator. The positions of both of the actuators are selected such that any order modes of the

plate can be excited. Multiple reference active noise control is applied to acoustical fields with multiple noise sources to achieve low-frequency noise reduction.

Besides the experimental method, computation is also conducted to explore the sound field induced by plate vibration. To develop effective general computer-aided-engineering methods for structural design optimization of vibroacoustic problem, Shou *et al.* (2003) proposed a numerical method of optimum design of mechanical structures for reducing noise. This method couples an optimization technique based on a genetic algorithm with both a finite element code for determining structural vibrations and acoustic radiation analysis for determining sound pressure levels at the receiver point. Reducing the sound pressure level associated with the fundamental acoustic resonant mode is accomplished by adding masses to a vibrating plate coupled to an acoustic cavity which is excited by a sound source. The positions of the masses on the plate are adopted as the design variables. By using the presented method, the optimal positions that would not be easy to be found by any intuitive solution are determined so as to effectively reduce the sound pressure level.

Gardonio *et al.* (2000) proposed a theory of an impedance-mobility matrix model to predict the structural vibration transmission between two plates, which are mechanically coupled via an active mounting system. With the model, the active and passive isolation effectiveness of different types of mounting systems has been

---

studied. In particular, the case of a three-mount isolator system with inertial or reactive actuators has been investigated. Through the isolator system, the structure-borne noise transmission between flexible mechanical systems connected via a set of mounts can be reduced.

Lee *et al.* (2005) proposed a new analytical formulation for the sound radiation from an annular or circular disk that explicitly considers the disk thickness effect on sound radiation from out-of-plane modes. Out-of-plane (flexural) vibration is a major source of sound radiation from many mechanical or structural components. Structural eigensolutions for the out-of-plane modes and sound radiation from the modal vibration of a thick annular disk with free-free boundaries have been calculated using both thick and thin plate theories. It is shown that thin, light, poroelastic plates can provide high values of the acoustic absorption even for low-frequency sound, Sakagami (2001) once developed a method to calculate the acoustic response of a thin, baffled, poroelastic plate in a rigid baffle with simply supported edges. The acoustic properties of the porous material are predicted using the effective fluid assumption.

Chapman *et al.* (2005) once conducted an asymptotic analysis of the sound and vibration produced when a metal plate is forced into motion by its contact with vibrating machinery on one side, and radiates sound into water on the other side. The effects of the greatest interest in the problem are the sound field radiated

---

directly into the fluid from the forcing region, and the surface wave propagating in the plate and neighboring fluid. These effects are analyzed in detail, both with regard to their numerical values and also the way in which these numerical values are determined by scaling laws. The ‘significant’ scaling, which gives accurate results over a wide frequency range, is used to obtain scaling laws for all aspects of the acoustic field and plate vibration. The mathematical method used is scaling of the frequency with the square of the intrinsic fluid-loading parameter to maximize the number of terms in the dispersion relation which balance at leading order. The ‘significant’ scaling, which gives accurate results over a wide frequency range, is used to obtain scaling laws for all aspects of the acoustic field and plate vibration.

A coupled system between the vibration of a flexible plate and the ensuing acoustic radiation is investigated by Frendi (1994). The plate is excited by a time harmonic, normally incident acoustic source, the amplitude of which is varied. Both linear and non-linear time periodic vibrations as well as aperiodic responses are computed. In each case, the acoustic radiation pattern resulting from the plate vibration is described.

Different with the researchers above, Meunier *et al.* (2001) extend their research to a 'psychomechanical' level. Most studies on acoustic radiation by vibrating bodies have focused on the physical aspects of either the vibration itself (displacement, velocity of the vibrating structure) or the acoustic field radiated

---

outside the structure. However, this paper presents a combination of vibroacoustic and psychoacoustic studies of sounds radiated by a vibrating structure. The author focuses on the calculation of the sound field which is radiated by a baffled thin-plate structure immersed in a fluid, on the surface of which the acceleration is given. This study confirms the interest of extending vibroacoustic studies to a more complete 'psychomechanical' investigation of the whole process of sound generation. Such investigations may apply to product sound quality and to active or passive noise control, by providing psychoacoustic feedback to the design of the vibrating structures or of the noise-control systems.

### ***1.6 Literature survey on plate silencers***

Except the part that the plates are used as a noise source, plates are also designed as silencers using different noise control mechanisms.

As stated in the preceding section, there are three main kinds of noise control methods: active noise control method, dissipative noise control method, and reactive noise control method. These three mechanisms are the fundamental mechanisms to design different types of plate silencers, which will be illustrated and evaluated in the following text.

### **1.6.1 Active noise control**

To get a good performance of noise reduction at broadband frequencies, Lee *et al* (2002) proposed to use active and passive hybrid panels. Basically, the mechanism of the active and passive hybrid panel is a combination of two distinct approaches-the passive and active approaches to achieve a broadband noise control. It utilizes the passive effect at mid and high frequencies and the active effect at low frequencies. The active hybrid panel was made with a host plate onto which piezoelectric sensors and actuators, a negative feedback controller and the sound absorbing material are bonded. Sound absorbing material and/or an air gap are used to enhance the NR in the mid and high frequency regions. The active approach of a piezoelectric sensor/actuator is adopted for the low frequency region. Instead of using the active control system, passive shunt damping is used for the NR at low frequencies. This is called a passive-hybrid panel. The use of piezoelectric passive shunt damping is an alternative for noise control at lower resonance modes since it can give selective damping at resonance frequencies with a simple shunt circuit.

However, because the panels are inserted across the duct, it will block the flow in the duct. Therefore, although it has a good performance over a broadband of frequencies, it has many limitations in the wide applications.

### **1.6.2 Passive noise control**

Porous materials are commonly used in noise control solutions to reduce both structure and air-borne sound together with the resonant structural vibrations. A new solution is once proposed (Sgard, 2003) to improve their acoustic absorption, acoustic attenuation and vibration damping properties. He investigated the influence of adding heterogeneities (macro solid pieces or air pockets) on the vibroacoustic behavior of a plate coated with a porous material radiating in a rigid walled cavity. However, it is also more effective for the mid-frequency noise, and not that effective for the low-frequency noise.

Sakagami *et al.* (1996) once conducted a research about the sound absorption characteristics of an elastic plate backed by a cavity. He first theoretically studied the acoustic properties of an infinite membrane without a cavity. The results provide the fundamental aspects of acoustical properties of membranes. When a membrane is used as a low-frequency sound absorber, it is usually placed parallel to a rigid wall with an air cavity behind, which is similar to a panel absorber. The analysis can give much information to design the purpose-made acoustic materials and to predict the sound fields within the boundaries made of such panels. The theoretical studies include a basic analysis of the sound absorption mechanism and the prediction of the absorption characteristics, which can also be applied to membrane problems. Sound absorption of a permeable membrane backed by a multiple-layered cavity has also been studied. Employing these theories, one can

---

predict the absorption characteristics of a panel or a membrane-type sound absorber.

It is found that the contribution of the source side surface to the total absorption is rather small, and it has a dip at the contribution of the cavity absorption, which is much greater than that of the source side surface: it is nearly equal to the total absorption at the resonant frequency. In the case of a plate, the loss factor is found to have a minor contribution to the total absorption only at the coincidence frequency. However, as the membrane alone cannot absorb the sound very well, the sound absorption of the cavity-backed membrane mainly depends on the contribution of the cavity absorption, not the membrane.

An experiment is also conducted (Tang, 2003) with a composite panel placed in a duct. Noise reduction in this exploration is achieved by a combination of a flexible thin plate and a duct wall, with air cavities and porous material in-between. Panel absorbers dissipate acoustic energy by different modes of vibration excitable in a complex system of rather thin, though comparatively stiff thick metals or plastic membranes. An air gap in-between a stiff panel and a thin flexible plate is “mass-air-mass” resonance. The absorption of the vibrational energy by the resonance is increased by filling the air gap behind the absorber with sound absorbing material. When the stiffness of the panel or the depth of the air gap between the panels is suitably adjusted, the resonance frequency can be adjusted to

---

a particular part in the noise spectrum. The mechanism of the panel absorber is a combination of vibrating mechanism and damping mechanism, and among the two mechanisms, the damping mechanism is still the more effective one. Besides, it's not easy to adjust all the variables to a suitable value, especially of the duct wall. Therefore, it has limitation in the industrial applications. What's the most important is that its mechanism is mainly good for a narrow frequency band.

Besides the dissipative noise control method, the reactive noise control method is also a mechanism often used in the noise reduction. The main reactive mechanisms which are often used in the plate-type wave reflector are: Helmholtz resonator mechanism and reflection mechanism.

Nowadays, several micromachined acoustic devices such as a microphone or a speaker have been developed in the field of microelectromechanical systems (MEMS) (Hsieh, 1997 & Haradine, 1997). These devices essentially make use of the principle of Helmholtz resonator (Maa, 1998). In this method, the perforations are reduced to submillimeter size so that they themselves will provide enough acoustic resistance and also sufficiently low acoustic mass reactance necessary for a wide-band sound absorber. The advantage of the micro-perforated panel (MPP) absorber is that it may be designed according to the required absorbing characteristics in terms of several parameters. On the basis of the MEMS technology, a tunable acoustic absorbing device using a Helmholtz resonator is

---

proposed (Konishi, 2000). Timing the resonance frequency of the device to desired frequency makes it possible to absorb sounds of different frequencies. The designed device forms an array of the Helmholtz resonator with a tunable compliance. A deephole array formed by X-ray lithography is fabricated into the front plate of the device in order to absorb low-frequency noise. The high-aspect-ratio acoustic hole allows absorption of a low-frequency noise without thickening the structure of the absorber. X-ray lithography is used to provide an array of high-aspect-ratio microholes at the same time. The high-aspect-ratio acoustic holes fabricated by micromachining allow the absorption of low-frequency noise. A large number of holes serve to increase the absorption unit which is proportional to the opening size of the resonator. However, the tunable acoustic absorber can be effective to low-frequency noises, its performance depends on the parameters of the device. For a fixed configuration, its effective frequency band is narrow. What's more, the difficulty to change the parameters of the absorber is another problem to be tackled before it can be widely applied.

A research is also conducted (Frommhold, 1994) on the acoustic properties of absorbing elements, which consist of metal membranes and show good sound absorption at low and medium frequencies over more than one octave. The behavior of the absorbing element is mainly determined by a combination of Helmholtz resonance and plate resonance. The structure is a symmetrical one. The smooth covering membrane seals the component against humidity and solid

---

particles, and reduces the flow resistance to a minimum. When properly dimensioned, the good absorption properties make the element appropriate for special requirements in industrial applications. However, the acoustic behavior also depends on a number of construction parameters and the material's properties, and the design of an optimized absorber for a particular application is a complicated task that has so far been solved only heuristically. Besides, it's also a difficult job to install so many silencers in a row.

With the development of both membrane absorbers and micro-perforated plate absorbers, Kang (1999) explored the combination of the two, such as a glass-fiber textile or a micro-perforated membrane mounted over an airtight cavity. On the basis of the theories for both the membrane absorber, namely a limp lightweight membrane backed by an air space, and the micro-perforated absorber, namely a cavity backed plate with low aperture ratio but many apertures of sub-millimeter size, the author combined them together. The basic idea of the theory is to regard an open weave textile or a micro-perforated membrane as a parallel connection of the membrane and apertures. In this way the effectiveness of one element relies on its relative impedance to the other. In other words, if the acoustic impedance of the apertures is much greater than that of the membrane, the absorption of the structure depends mainly on the characteristics of the membrane and conversely, the apertures will play a dominant role if their acoustic impedance is much less than that of the membrane. In order to modify the absorption, the acoustic impedance of

---

the structure can be adjusted by varying the appropriate parameters of the membrane and apertures. Although the absorption performance of such structures can be very high, this method is the most effective for the mid-frequency noises, and not very effective for the low-frequency noise.

Another research group led by Fuchs (1995) also uses the multilayered micro-perforated plate absorbers (MPA), whose prototype is Helmholtz resonator, to reduce the low and medium frequencies noise. By arranging a plate containing holes in front of an air cushion, the vibration of the air in the very small holes may be ideally damped by shearing forces and so a relatively broadband absorber can be created without using fibrous or porous materials. However, the device is most effective to the frequencies above 200 Hz, and its acoustic features depend on its material, which should be selected according to the respective application. This increases the difficulty of its application.

Takahashi *et al.* (2002) proposed a method of theoretical treatment of acoustic coupling due to flexural vibration of perforated plates and plates of porous elastic materials. The research focused on development of a generalized approach to investigate problems surrounding structural-acoustic coupling for both perforated plates and plates of porous elastic materials. For acoustic radiation from a vibration excited by a harmonic point-force, the attenuation effect of power radiation appears at frequencies below the critical frequency of coincidence. In the problem of sound

---

absorption of a perforated plate or a plate of porous elastic material backed by an air layer, as permeability decreases, the effect of plate vibration increases. For perforated absorber systems including plate vibration effects, the trend of variation from ordinary theory depends on plate thickness.

In summary, the silencers shown above are based on different mechanisms. Some of them make use of the dissipative mechanism, adding the porous materials on the plate or between the plate and the cavity, some of them adopt the microperforated noise absorption techniques, some rely on the combination of the Helmholtz resonance and plate resonance, others use the combination of the passive mechanism and the active mechanism. Although all these silencers make use of plates, their mechanisms are different from the plate-type wave reflector explored in this thesis. The plate-type wave reflector makes use of the sound induced vibration for the purpose of sound reflection, and is effective for a broad frequency range, especially for the low-frequency noise.

## Chapter 2: Real-plate model in two-dimension

### 2.1 Introduction

As analyzed by Huang (2002), for the drumlike silencer, three spectral peaks occur in the spectrum of the transmission loss with a high level of trough between them. This is a result of constructive inter-modal interaction of the first two *in vacuo* modes, which complement each other in wave reflection. For a membrane, it has *in vacuo* modes for which the modal wavelength is  $2L/n$ , where  $L$  is the length of the membrane and  $n$  the modal index. Since the inter-modal interaction is crucial for the success of the drumlike silencer, further exploration needs to be done to find whether other structural dynamics can have better performance in wave reflection.

For a membrane, which is fixed at both ends with a tension  $T$  applied on it, its *in vacuo* eigen-frequencies can be expressed as:

$$\omega_n = n\pi \sqrt{\frac{T}{\rho L^2}} \quad (n=1, 2, 3\dots), \quad (2.1)$$

which means that the second eigen-frequency is twice the first eigen-frequency.

However, for a plate, which has more boundary restrictions, the relationship between its eigen-frequencies is more complicated than that of the membrane. And the ratio of the first two eigen-frequencies is, therefore, different from that of the

---

membrane. For example, for a pinned-pinned uniform plate, its eigen-frequencies are:

$$\omega_n = (n\pi)^2 \sqrt{\frac{EI}{mL^4}} \quad (n=1, 2, 3\dots), \quad (2.2)$$

where  $E$  is the Young's modulus and  $m$  is the mass per unit area. In this case, plates, with various boundary conditions, are tried in the present thesis to get their performances in wave reflection, which leads to the noise reduction.

In this chapter, the plate-type wave reflector is simulated in a two-dimensional coupled system, including a structural mechanics domain and an acoustics domain. The plate with different boundary conditions is simulated by two different models, the mindlin-plate model and the plane-stress model.

The most frequently encountered boundary conditions for rectangular plates are either fixed or simply-supported. In the first section, the mindlin-plate model is introduced. In the mindlin-plate model, many boundary conditions are available, such as simply-supported, fixed, rotation constrained, and so on. Another advantage of the mindlin-plate model is that it can save computational memory. For a uniform plate with two simply-supported ends, the final results using the mindlin-plate model will be compared with the analytical model.

In the second section, a plane-stress model is introduced. A comparison is conducted between the plane-stress model and a plane-strain model. A uniform

---

plate with two clamped ends is modeled in both the mindlin-plate model and the plane-stress model, and the results of the two different models are compared. The result shows that the performance of the plate with fixed ends is not as good as that with two simply-supported ends, although the simply-supported boundary condition is difficult to be realized in acoustic experiments.

Under this situation, a non-uniform plate with two fixed thinner ends is adopted to approximate the simply-supported uniform plate. The simulation of the non-uniform plate is conducted in the plane-stress model. When the shape of the non-uniform plate is modified, four spectral peaks appear in the low-frequency region, showing an even wider stopband than the simply-supported boundary conditions.

## **2.2 Mindlin-plate model**

### **2.2.1 The theoretical model**

To begin with, the plate with simply-supported ends is investigated. For a simply-supported edge, the deflection and moment are zero:

$$w = 0 \quad \text{and} \quad M_x = -D\left(\frac{\partial^2 w}{\partial x^2} + \mu \frac{\partial^2 w}{\partial y^2}\right) = 0, \quad M_y = -D\left(\frac{\partial^2 w}{\partial y^2} + \mu \frac{\partial^2 w}{\partial x^2}\right) = 0 \quad (2.3)$$

where  $w$  is the deflection in the  $z$ -direction, and  $M_x, M_y$  are the moments around  $x$  and  $y$  axes, respectively.

Since the slope along the simply-supported edge is always zero,  $\frac{\partial w}{\partial y} = 0$ , the

quantity  $\mu \frac{\partial^2 w}{\partial y^2}$  and  $\mu \frac{\partial^2 w}{\partial x^2}$  vanish and the moment boundary condition becomes

$$M_x = \frac{\partial^2 w}{\partial x^2} = 0, M_y = \frac{\partial^2 w}{\partial y^2} = 0.$$

The configuration of the plate-type wave reflector is shown in Figure 2.1:

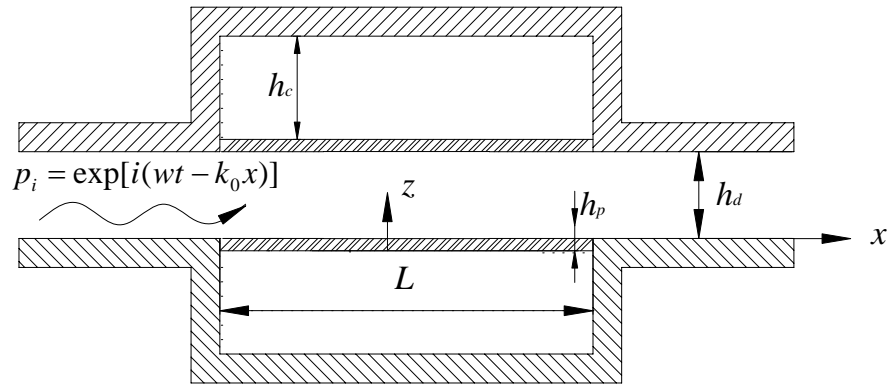


Figure 2.1 : Configuration of a plate-type wave reflector with simply-supported uniform plates

In Figure 2.1, a rectangular duct is modeled by a two-dimensional channel. Two identical plates with two simply-supported ends are backed by two rigid-walled

cavities. When excited by an incident wave, the plates vibrate and the left-going sound radiation forms the reflection wave thus reducing the transmitted wave.

In the following simulations, dimensionless parameters are used by normalizing dimensional variables by a set of three basic dimensions: duct height  $h_d^*$  as the length scale, air density  $\rho_0^*$ , and the speed of sound in free space  $c_0^*$ :

$$p = \frac{P^*}{\rho_0^*(c_0^*)^2}, \quad f = \frac{f^* h^*}{c_0^*}, \quad \omega = 2\pi f, \quad m = \frac{m^*}{\rho_0^* h_d^*}, \quad E = \frac{E^*}{\rho_0^*(c_0^*)^2}, \quad (2.4)$$

where  $p, f, \omega, m, E$  are, respectively, the dimensionless sound pressure, frequency, angular frequency, mass ratio, and Young's modulus of the plate material. The asterisks denote dimensional variables while the corresponding dimensionless ones are without asterisks. Occasionally, it would be beneficial to retain the dimensional form of equations so that the physical meaning is not obscured by the parametric normalization. For example,  $p^* = \rho_0^* c_0^* u^*$  holds for travelling waves in the  $+x$  direction. In dimensionless form, the correct result is  $p = u$ , but  $p = \rho_0 c_0 u$  is retained with the understanding of  $\rho_0 = \rho_0^*/\rho_0^* = 1, c_0 = c_0^*/c_0^* = 1$ .

In the simulation, the system is divided into three domains: one is structural mechanics domain, the other two are acoustics domains. Because two cavities are used on the two sides of a two-dimensional duct of height  $h_d$ , only half of the duct and one cavity need to be calculated by virtue of symmetry, as shown in Figure 2.2.

---

The duct centre line is the symmetrical line equivalent to a rigid wall. The dimensionless geometry used for the current simulation is given as:  $h_d = 1$ ,  $L=5$ ,  $h_c=1$ .

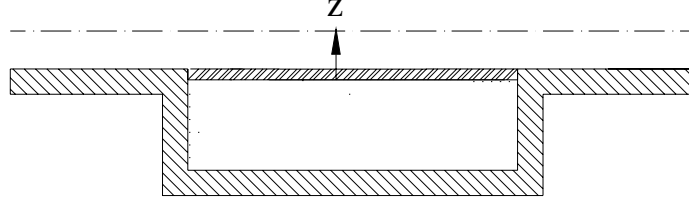


Figure 2. 2: The configuration of the geometry

The two acoustics domains consist of the half duct and one cavity separately. The dynamics governing equation of the air in the two acoustics domains is the wave equation

$$\square^2 f = 0, \quad f = p, \rho, \vec{v}, \quad \square^2 = \nabla^2 - c^{-2} \partial^2 / \partial t^2. \quad (2.5)$$

Here a harmonic wave with velocity potential  $\phi$  is assumed, and Eq. (2.5) can be rewritten in the form of Helmholtz equation

$$\nabla^2 \phi - \frac{\partial^2 \phi}{c^2 \partial t^2} = 0 \xrightarrow{\phi = \phi \exp(i\omega t)} \nabla^2 \phi + k^2 \phi = 0, \quad (2.6)$$

where  $k = \omega/c$  is the wave number. The pressure  $p$  is

$$p = -\rho_0 \frac{\partial \phi}{\partial t}. \quad (2.7)$$

For frequencies below the cut-on frequency of the duct, the inlet and outlet boundaries contain simple traveling wave elements for which:

$$p = \pm \rho_0 c u , \quad (2.8)$$

where the signs ‘ $\pm$ ’ are for the downstream and upstream traveling waves, respectively.

There are totally four types of boundaries in both the acoustics domain: the incident waves mixed with the reflected waves, the out-going waves at the exit, stationary solid walls and the moving boundary with a specified vibration velocity. For the inlet boundary (the left end) of the duct, the waves are composed of the reflected wave mixed with the known incident wave. The boundary condition is written in terms of the total velocity potential. The actual condition, however, is simply the statement that the reflection wave is a simple out-going plane wave to the left.

$$p_r = -\rho_0 c u_r, \quad p_r = p - p_i, \quad u_r = u - u_i \rightarrow p + \rho_0 c u = p_i + \rho_0 c u_i, \quad (2.9)$$

where subscript  $r$  denotes ‘reflection’ and ‘ $i$ ’ for the incident. By specifying an incident wave of unit velocity amplitude,  $u_i = 1$ ,  $p_i = \rho_0 c$ , the inlet boundary condition becomes

$$p + \rho_0 c u = 2\rho_0 c . \quad (2.10)$$

The physical boundary type of the right end of the duct is the out-going waves. The out-going waves in the  $n$  direction can be written as:

$$p = \rho_0 c u_n . \quad (2.11)$$

The air on the boundaries of the upper and lower surfaces of the plate has a coupled

relation with its vertical velocity specified by the plate motion. Then, the kinematic boundary condition is

$$\frac{\partial \phi}{\partial z} = \frac{\partial v}{\partial t}, \quad (2.12)$$

where  $v$  is the displacement of the plate in  $z$ -direction.

The wall of the duct and cavity are assumed to be acoustically rigid, so the velocity of the particles normal to the wall is zero. Then we can define the boundary condition of the solid wall as:

$$\frac{\partial \phi}{\partial n} = 0. \quad (2.13)$$

In the Structural mechanics domain, the governing equation is the plate dynamics equation:

$$m_s \frac{\partial^2 \eta}{\partial t^2} + D \left( \frac{\partial^4 \eta}{\partial x^4} + 2 \frac{\partial^4 \eta}{\partial x^2 \partial y^2} + \frac{\partial^4 \eta}{\partial y^4} \right) + (p_i + \Delta p) = 0, \quad (2.14)$$

where  $m_s$  is the mass per unit area of the plate,  $D$  is the stiffness matrix,  $\eta$  is the displacement of the plate,  $p_i$  is the incident wave,  $\Delta p$  is fluid loading induced by the plate vibration. The self-induced loading  $\Delta p$  can be divided into three parts:

$$\Delta p = p_{+rad} - (p_{-rad} + p_{-ref}), \quad (2.15)$$

where  $p_{+rad}$  and  $p_{-rad}$  are the radiation sound pressures on the upper and lower plate surfaces, respectively,  $p_{-ref}$  is the sound reflected by the two vertical cavity walls. For the specific depth of  $h_c = 1$ ,  $p_{+rad} = -p_{-rad}$ .

The structure mechanics domain consists of a uniform plate, whose dimensions are  $L=5$  and  $h_p=0.05$ . The material properties of the plate are defined as follows. The dimensionless density  $\rho = \frac{m}{h_p} = \frac{1}{0.05} = 20$  (corresponding to a mass ratio of  $m=1$ ), the Poisson's ratio  $\nu = 0.33$ .

Both ends of the non-uniform-shaped plate are defined as simply-supported ends. Because the upper and lower surfaces of the plate are exposed to the pressure of the duct and the cavity separately, its vibration is driven by the difference of the air pressure across the interface at  $y=0$ ,  $p|_{y=0-} - p|_{y=0+}$ . Therefore, their boundary conditions can be expressed as that the loading per unit area is equal to the difference of the air pressure. Note that both the plate vibration velocity and the air pressure on the plate are not known a priori. They are solved in the coupled problem.

### **2.2.2 Implementation in the finite element method**

FEMLAB® is a powerful interactive environment for modeling and solving all kinds of scientific and engineering problems based on partial differential equations (PDEs), and works under the programming language of MATLAB®. In the finite element simulation of FEMLAB®, the ability to create multiphysics models—those with more than one type of physics or equations such as coupled-field problems—is one of FEMLAB’s most powerful capabilities. In such a model, the software solves all the equations, taken from various areas of physics, as one fully coupled system, and does so simultaneously. In our numerical simulation, the whole system is modeled in three-dimensional geometries, and is divided into three domains. Two of them are the acoustics domains for the air in the duct and cavity, the two being geometrically de-linked. The third is a structural mechanics domain for the plate. The two kinds of domains have different models with different dependent variables. The velocity potential  $\phi$  is defined as the variable for the acoustics domain, and the global displacement  $w$  in the  $z$ -direction and the rotations  $\theta_x$ ,  $\theta_y$  around the global  $x$  and  $y$  axes are used as the dependent variables in the structural mechanics domain.

To couple the three domains together, a new kind of variable, non-local extrusion coupling variable, is introduced. The extrusion coupling variable maps values from the source domain to the destination domain, and hence couples the two domains together. It is extremely powerful in their ability to make the value and the exact

---

Jacobian of an expression available non-locally. The Jacobian for problems formulated using the finite element method is usually large but sparse. This is because the solution at each node in the mesh can depend at most on the degrees of freedom from the neighboring mesh elements. However, by introducing coupling variables, non-local dependencies fill up the rows and columns of the affected source and destination nodes. This extra fill-in might make the Jacobian matrix slightly less sparse, in which case the solution speed is only slightly affected. The weak-form of the solver is used here to implement the coupling. The weak form makes it possible to build models with mixed space and time derivatives, and solve models that need an exact Jacobian for convergence. It is usually the best because it can get a correct Jacobian and assembly somewhat faster.

In the acoustics domain, mathematically, there are two types of boundary conditions in FEMLAB: Dirichlet condition and the Robin type condition. In the present problem, all the four physical boundary conditions are the Robin type conditions due to the choice of velocity potential  $\phi$  as the dependent variable of the actual problem. Since for the Helmholtz equation, the boundary condition is simplified as  $\partial\phi/\partial n + q\phi = g$ , where  $\partial\phi/\partial n = n \cdot \nabla\phi$  is the acoustic particle velocity projected in the outward normal direction  $n$  of the boundary.

At the inlet boundary, the boundary condition can be written as:

$$p + \rho_0 c u = 2\rho_0 c \rightarrow -\rho_0 i \omega \phi + \rho_0 c \partial\phi/\partial x = 2\rho_0 c \xrightarrow{x \cdot n} \partial\phi/\partial n + ik\phi = -2. \quad (2.16)$$

At the outgoing boundary, the boundary condition can be defined as:

$$p = \rho_0 c u_n \rightarrow -\rho_0 \partial \phi / \partial t = \rho_0 c \partial \phi / \partial n \rightarrow \partial \phi / \partial n + ik \phi = 0. \quad (2.17)$$

For the two plate surfaces, the vertical displacements of the upper and lower horizontal surfaces of the non-uniform plate,  $v_1$  and  $v_2$  respectively, are defined as two coupling variables from the structural mechanics domain to the corresponding boundaries of the acoustics domain. The boundary where the upper

plate surface is located has the boundary condition of  $\frac{\partial \phi}{\partial n} = -\frac{\partial v}{\partial t} = -ikv_1$ , where the

‘-’ sign means the displacement of the upper surfaces is opposite to the normal direction of the air acoustics domain above the plate. For the lower plate boundary,

$\frac{\partial \phi}{\partial n} = \frac{\partial v}{\partial t} = ikv_2$ . The expression of the boundary condition for the solid walls is

$$\frac{\partial \phi}{\partial n} = 0.$$

For the structural mechanics domain, one of the most popular models for plate bending is the Mindlin plate theory. This theory describes all displacements in the plate based on the rotations about the  $x$ - and  $y$ -axes and the displacements normal to the plate. Mindlin plate is defined as a thin planar structure, whose thickness as a rule is less than one tenth of its width. In contrast to the plane stress and plane strain 2D cases, the forces are either applied in the direction normal to the plate, or as moments about directions in the plane where the plate lies. The main deformation takes place in the out-of-plane direction.

---

The Mindlin plate is based on the following engineering assumption: a plane originally perpendicular to the mid surface remains plane after loading, but not necessarily perpendicular to the deformed mid surface. The change in angle accounts for the transverse shear deformation. There are two main groups of plates: one is thin plates, the other is thick plates. Because the theory also accounts for transverse shear deformations, it suits analyses for both thin and thick plates. In the thin plate theory, the transverse shear deformation is neglected, in the same way as Euler beams neglect shear deformations. In the thick plate theory, the transverse shear deformation is included.

The in-plane strain components depend on the rotation derivatives defined by the shape function and the  $z$  coordinate in the plate.

$$\varepsilon = \begin{bmatrix} \varepsilon_x \\ \varepsilon_y \\ \gamma_{xy} \end{bmatrix} = z \begin{bmatrix} \frac{\partial \theta_y}{\partial x} \\ -\frac{\partial \theta_x}{\partial y} \\ \left( \frac{\partial \theta_y}{\partial y} - \frac{\partial \theta_x}{\partial x} \right) \end{bmatrix} = z\Theta \quad (2.18)$$

The in-plane stress components in the plate are described by the symmetric stress tensor:

$$\sigma = \begin{bmatrix} \sigma_x & \tau_{xy} \\ \tau_{yx} & \sigma_y \end{bmatrix} \quad \tau_{xy} = \tau_{yx} \quad (2.19)$$

consisting of 2 normal stresses ( $\sigma_x$ ,  $\sigma_y$ ) and two or, if the symmetry is used, one shear stress  $\tau_{xy}$ . The stress-strain relation for linear conditions including initial stress and strain and thermal effects reads:

$$\sigma = D\varepsilon \quad (2.20)$$

where  $D$  is the 3 x 3 elasticity matrix, and the stress and strain components are described in vector form with the three stress and strain components in column vectors:

$$\sigma = \begin{bmatrix} \sigma_x \\ \sigma_y \\ \tau_{xy} \end{bmatrix} \quad \varepsilon = \begin{bmatrix} \varepsilon_x \\ \varepsilon_y \\ \gamma_{xy} \end{bmatrix}. \quad (2.21)$$

The elasticity matrix  $D$  and the more basic matrix  $D^{-1}$  (the inverse of  $D$ , also known as the flexibility or compliance matrix) are defined differently for isotropic, orthotropic, and anisotropic materials. Because our simulation only concerns the problem with isotropic material, the matrix for the other two materials won't be described here. For isotropic material, the  $D^{-1}$  matrix is defined as

$$D^{-1} = \frac{1}{E} \begin{bmatrix} 1 & -\nu & 0 \\ -\nu & 1 & 0 \\ 0 & 0 & 2(1+\nu) \end{bmatrix}, \quad (2.22)$$

where  $E$  is the Young's modulus, and  $\nu$  is Poisson's ratio. Inverting  $D^{-1}$  symbolically results in the following definition of  $D$ :

$$D = E \begin{bmatrix} \frac{1}{1-\nu^2} & \frac{\nu}{1-\nu^2} & 0 \\ \frac{\nu}{1-\nu^2} & \frac{1}{1-\nu^2} & 0 \\ 0 & 0 & \frac{1}{2(1+\nu)} \end{bmatrix}. \quad (2.23)$$

FEMLAB bases its implementation of the structural mechanics application modes on the equilibrium equations expressed in the global stress components. The three governing Mindlin plate equations are:

$$\begin{aligned} -\frac{\partial}{\partial x} \left( D \frac{\partial \theta_x}{\partial x} \right) - \frac{\partial}{\partial y} \left( (1-\nu) \frac{D}{2} \frac{\partial \theta_x}{\partial y} \right) - \frac{\partial}{\partial x} \left( \nu D \frac{\partial \theta_y}{\partial y} \right) - \frac{\partial}{\partial y} \left( (1-\nu) \frac{D}{2} \frac{\partial \theta_y}{\partial x} \right) - Gd \frac{\partial w}{\partial x} + Gh_p \theta_x &= 0 \\ -\frac{\partial}{\partial y} \left( \nu D \frac{\partial \theta_x}{\partial x} \right) - \frac{\partial}{\partial x} \left( (1-\nu) \frac{D}{2} \frac{\partial \theta_x}{\partial y} \right) - \frac{\partial}{\partial x} \left( (1-\nu) \frac{D}{2} \frac{\partial \theta_y}{\partial x} \right) - \frac{\partial}{\partial y} \left( D \frac{\partial \theta_y}{\partial y} \right) - Gh_p \frac{\partial w}{\partial y} + Gh_p \theta_y &= 0 \\ -\frac{\partial}{\partial x} \left( Gh_p \frac{\partial w}{\partial x} \right) - \frac{\partial}{\partial y} \left( Gh_p \frac{\partial w}{\partial y} \right) + \frac{\partial}{\partial x} \left( Gh_p \theta_x \right) - \frac{\partial}{\partial y} \left( Gh_p \theta_y \right) &= g \rho h_p \end{aligned} \quad (2.24)$$

where  $\theta_x$ ,  $\theta_y$  are the rotation about the  $x$ - and  $y$ -axes respectively, and the parameters  $G$  and  $D$  are defined as:

$$G = \frac{E}{2(1+\nu)1.2}, \quad D = \frac{Eh_p^3}{12(1-\nu^2)}. \quad (2.25)$$

The two ends of the plate is defined as simply-supported, that is, the rotations ( $\theta_x$  and  $\theta_y$ ) are free, but the  $z$ -displacement ( $w$ ) is set to zero on the boundaries. For the upper and lower surfaces of the plate, coupling variables are also needed in the

boundary condition definition. The pressures from the duct and cavity,  $p_d$  and  $p_c$ , are defined from the acoustics domain to the upper and lower surfaces of the plate. Then, the horizontal boundaries facing the duct has a loading of  $F_z = -p_d$ , where  $F_z$  is the force per unit area along  $z$ -direction, and ‘-’ means that the direction of the force is opposite to the normal direction. For the lower horizontal surface of the plate, which faces the cavity, its boundary condition can be defined as  $F_z = p_c$ .

For the two domains, a frequency-response analysis solver in weak form is used. This type of solver solves for the steady-state response to harmonic excitation loads. In this simulation, it is used in a parametric mode in which the dimensionless excitation frequency is varied from 0.002 to 0.2 in steps of 0.002. Then the final result— transmission loss under different excitation frequencies can be obtained. The transmission loss ( $TL$ ) is defined as the ratio of the sound intensity:

$$I_{\pm} = pu_{\pm} = \frac{1}{2} \rho c k^2 |\phi_{\pm}|^2, TL = 10 \log_{10} \frac{I_{in}}{I_{exit}}, \quad (2.26)$$

where  $\rho = \frac{P}{c^2}$  is the density fluctuation in the air,  $I_{in}$  and  $I_{exit}$  are the intensities of the incident sound and transmitted sound, respectively.

### 2.2.3 Results

To get the optimal performance of the plate-type wave reflector, the bending stiffness is a crucial factor. In the present studies, the optimal bending stiffness is determined through the comparisons among the performances of different bending stiffnesses.  $TL_{cr} = 10dB$  is specified in Figure 2.3 as a criterion value, and the stopband is defined as the frequency range,  $f \in [f_1, f_2]$ , where the transmission loss is everywhere equal or above the criterion level. The ratio of the band limits,  $f_2 / f_1$ , namely the logarithmic bandwidth, is used as the key performance indicator, while the same structure-to-air mass ratio is used. Figure 2.3 shows the transmission loss spectra among the plate-type wave reflectors with different bending stiffness. Here,  $TL_{cr} = 10dB$  is plotted in the Figure 2.3 for reference.

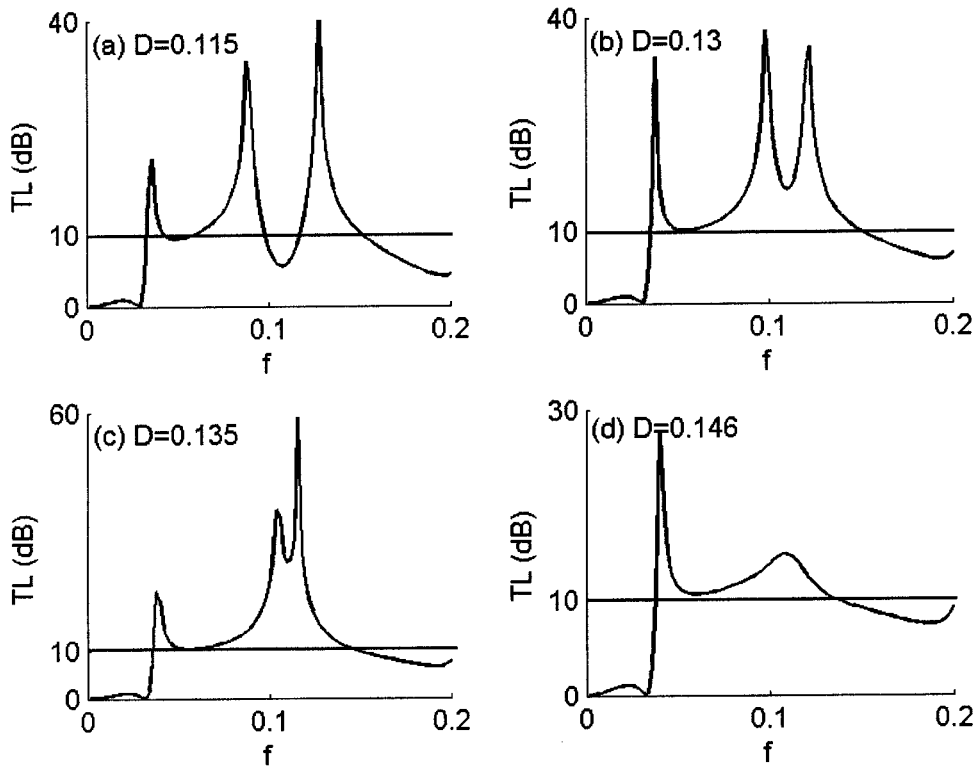


Figure 2.3: A stacked view of the transmission loss spectra of simply-supported plate-type wave reflector with different bending stiffness

In Figure 2.3, four different bending stiffnesses are selected to show the effect of the bending stiffness on the transmission loss spectra of the plate. It is found that with the increasing bending stiffness, the first and second peaks shift from lower frequencies to higher frequencies, while the third peak shifts from the higher frequencies to lower frequencies. In this way, the trough between the second and third peaks is elevated above the criterion level of 10dB, as shown in the first three subfigures. When the bending stiffness continues increasing, the second and third

peaks finally merge into one peak, as shown in Figure 2.3(d) ( $D=0.146$ ), and there are two peaks, the former first peak together with the merged peak, left within the stopband. If the bending stiffness continues increasing, the merged peak will be cut in magnitude until it drops below the crucial line  $TL_{cr} = 10dB$ , and only one peak is left in the low-frequency region. For the specified simply-supported plate, the optimal bending stiffness is  $D=0.13$ , shown in Figure 2.3(b), and the corresponding biggest logarithmic bandwidth is  $f_2 / f_1 = 0.15 / 0.0353 = 4.25$ . The pattern shift of the transmission loss spectra with changing bending stiffness will be analyzed in detail in section 2.5.

Figure 2.3(b) shows the optimal performance of the plate with a mass ratio of  $m=1$ , but actually, the optimal performances of the plates vary with  $m$ . Figure 2.4 shows a comparison between the performances of the plates with  $m=0$  and  $m=1$ . In Figure 2.4 (a), it can be found that when  $m=0$ , the bandwidth is very wide, ranging from  $f_1 = 0.0343$  to  $f_2 = 0.2077$ . While in Figure 2.4(b), the bandwidth of  $m=1$  is much narrower than that of  $m=0$ . The relationship among the mass ratio, optimal bending stiffness and the optimal bandwidth will be described in details in the following section.

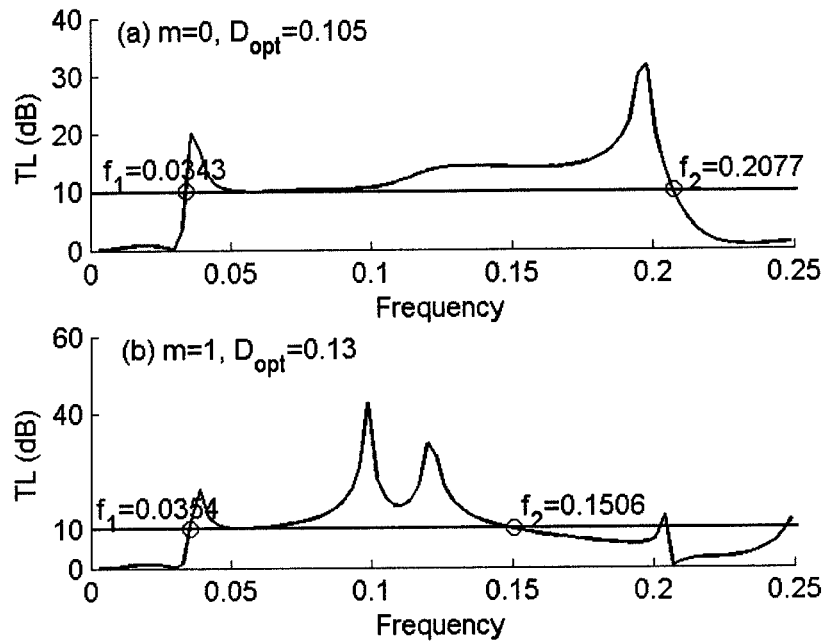


Figure 2.4: The comparison between the performances of the simply-supported uniform plates with (a)  $m=0$  and (b)  $m=1$

## 2.3 Plane-stress model

### 2.3.1 Plane-stress model vs plane-strain model

In structural mechanics, the equations relating stress and strain arise from the balance of forces in the material medium. The stress conditions encountered in axially loaded bars, shafts in torsion, and beams in bending are examples of a state of stress called plane stress. Plane stress condition

---

mainly refers to a plate, which is thin enough such that there is no variation of displacement (and temperature) with respect to the third direction. In other words, only the  $x$  and  $y$  faces of the plate are subjected to stresses, and all stresses act parallel to the  $x$ - $y$  plane.

Compared with plane stress condition, a deformation state where there are no displacements in the  $z$ -direction, and the displacements in the  $x$ - and  $y$ -directions are functions of  $x$  and  $y$  but not  $z$  is called plane strain. The differences between the plane stress condition and plane strain condition are shown in the following table:

	Plane stress	Plane strain
Stress	$\sigma_z = 0, \tau_{yz} = 0, \tau_{xz} = 0$ $\sigma_x, \sigma_y, \tau_{xy}$ may have nonzero values	$\tau_{yz} = 0, \tau_{xz} = 0$ $\sigma_x, \sigma_y, \sigma_z$ and $\tau_{xy}$ may have nonzero values
Strain	$\gamma_{yz} = 0, \gamma_{xz} = 0$ $\varepsilon_x, \varepsilon_y, \varepsilon_z$ and $\gamma_{xy}$ may have nonzero values	$\varepsilon_z = 0, \gamma_{yz} = 0, \gamma_{xz} = 0$ $\varepsilon_x, \varepsilon_y, \gamma_{xy}$ may have nonzero values

Table 2-1: Comparison of plane stress and plane strain

In our simulation, a plate with two fixed ends and two free ends is considered. The upper and lower surfaces of the plate are under the pressure from the duct and cavity respectively, but there is no shear stress along the third direction. According to the differences shown above, this situation should be defined as the plane stress condition.

### **2.3.2 The theoretical model**

In the plane stress model for a two-dimensional plate, the plate with two clamped ends, instead of two simply-supported ends, are simulated. The governing equation and the boundary conditions of the model are almost the same as those in the mindlin model, except that in plane stress model, two clamped ends replace two simply-supported ends. For a fixed edge, the deflection and slope are zero

$$w = 0 \quad \text{and} \quad \frac{\partial w}{\partial y} = \frac{\partial w}{\partial x} = 0, \quad (2.27)$$

where  $w$  is the deflection of the plate.

The coupled system is divided into two domains: acoustics domain for the duct and cavity, and structural mechanics domain for the plate with two clamped ends and two free ends.

### 2.3.3 Results

To get the optimal performance of the uniform plate with two clamped ends, comparisons among the final results of different bending stiffnesses are also conducted like those in the mindlin plate model. The results shows that when the optimal value of the dimensionless Young's modulus is  $E=6550$ , the widest bandwidth is obtained. Figure 2.5 shows a comparison between the results of the plane stress model and the mindlin plate model with the same parameters and boundary conditions.

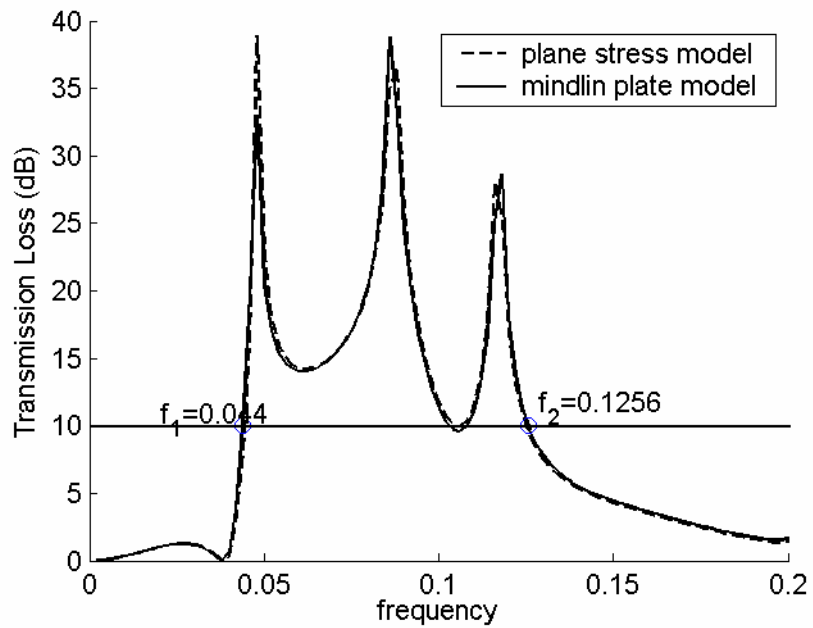


Figure 2.5: Comparison between the results of the plane stress model and the mindlin plate model with the same parameters of  $m=1$ ,  $E=6550$ .

The two curves shown in Figure 2.5 match each other very well, except for some small differences, which are caused by the mesh part of the two models. In the mindlin plate model, the duct and cavity are created with three-dimensional geometry; while in the plane stress model, they are created with two-dimensional geometry. Restricted by the memory of the computer, the mesh in the three-dimensional model is coarser than that in the two-dimensional model. This leads to the small discrepancies between the two final results.

Another comparison is also made, shown in Figure 2.6, between the optimal performance of the uniform plate with two simply-supported ends with  $E_{opt} = 12480$  and the uniform plate with two fixed ends with  $E_{opt} = 6550$ .

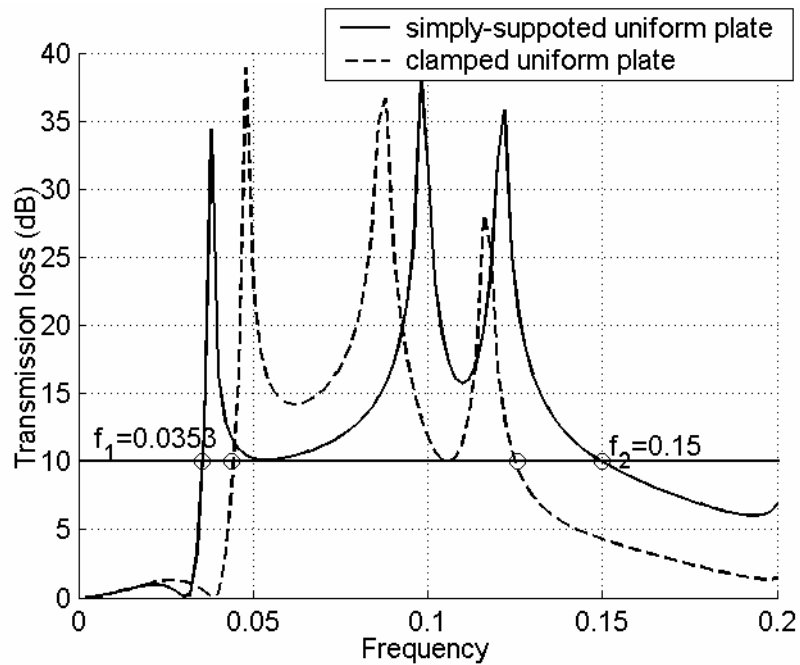


Figure 2.6: The comparison between the optimal performances of a clamped uniform plate model ( $E=6550$ ) and a simply-supported plate model ( $E=12480$ ) with the same mass ratio of  $m=1$ .

From Figure 2. 6, it is easily found that the plate with two simply-supported ends can provide much wider stopband than the fixed ends. This is because the essential mechanism of the plate-type wave reflector, the reflection mechanism, requires the effective length for reflection as long as possible. Compared with the simply-supported boundary condition, the fixed boundary condition lays more restriction to the portion of the plate near the edges, and this just shortens the effective length of the plate, thus reducing its effectiveness in noise reflection. From this comparison, it is derived that a simply-supported uniform plate with less restriction to the plate reflection is preferred over a clamped uniform plate.

## **2.4 Non-uniform plate model**

Although the simply-supported ends can be easily achieved in usual structural mechanics, it is hard to be realized in an acoustic system. This is because the systems in acoustics are usually very light, and the methods to implement the simply-supported ends in a real device often result in the clamped-clamped ends. Under this situation, an alternative plate, named non-uniform plate, is studied. The

non-uniform plate is a symmetric one with thicker middle part and two thinner ends, whose configuration is shown in Figure 2.7.

For a non-uniform plate, when its two thinner ends are clamped, it shows similar performance to that of the simply-supported plate, and the clamped-clamped boundary condition is easy in experimental implementation. This is because the thinner end of the plate has a lower bending stiffness than that of the middle thicker

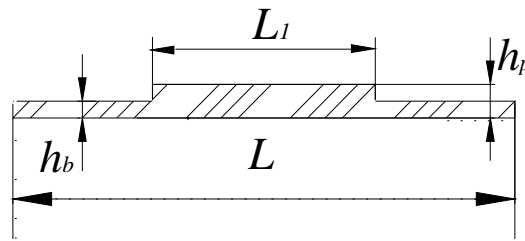


Figure 2.7: Configuration of a non-uniform plate

part. With the softer ends, although the whole structure is clamped at both sides, the restriction to the portions near the plate edges caused by the clamped boundary condition is greatly reduced.

To get the *in vacuo* modes, the *in vacuo* eigen-frequencies of the specific model are firstly obtained through FEMLAB calculation, and then the corresponding vibration modes of the plate are plotted under these eigen-frequencies. The first two *in vacuo* modes of such a clamped-clamped non-uniform plate are shown in Figure 2.8. The mode shapes show that the vibration of the portions near the plate

---

edges is greatly promoted, compared with that of a clamped uniform plate, and is similar to that of the simply-supported uniform plate. For this reason, the clamped non-uniform plate will be used in all the following simulations to substitute for the simply-supported uniform plate. In the remainder of this section, the plane stress model is used to explore the performance of the clamped non-uniform plate, whose thickness of the two thinner ends is fixed as  $h_b = 0.3h_p$ .

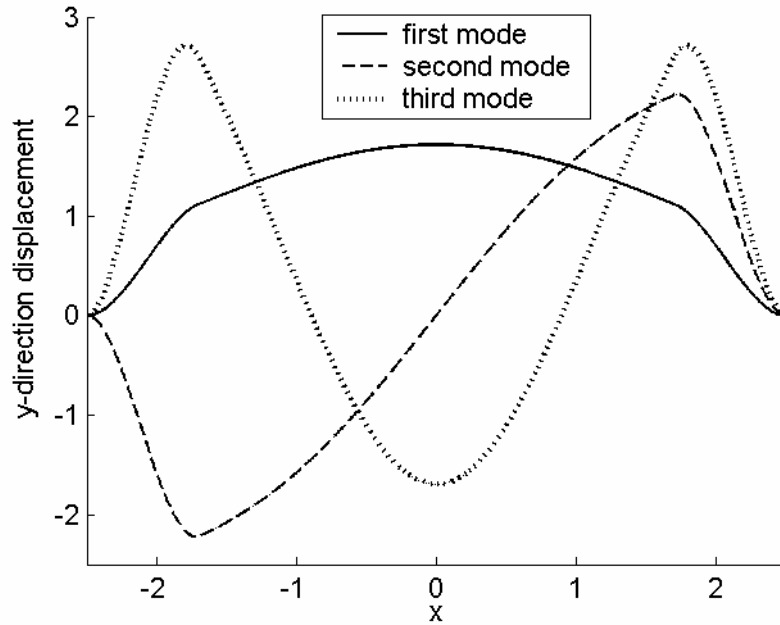


Figure 2.8: The first three mode shape of the non-uniform plate with  $L_1 = 3$  and  $h_b = 0.015$

In the numerical model, mesh is generated in FEMLAB when the maximum edge size,  $H_{\max}$ , is specified.  $H_{\max}$  is a dimensionless quantity normalized by the duct height  $h$ , and is determined by the size of the created geometry. In the acoustics

domain,  $H_{\max}=0.05$  is selected, and totally 15304 elements are generated. In the structural mechanics domain, because of its rapid shape changes, a global mesh parameter is not suitable any more. Instead, different values of  $H_{\max}$ , varied from 0.003 to 0.01, are given to different boundaries according to their specific sizes. Finally, totally 7438 quadratic elements are generated.

Comparisons are made about the optimal performances of the plate with different lengths of the middle thicker part  $L_1$ . For all the different plate models, different values of  $L_1=3.2, 3.4, 3.6, 3.8, 4.0, 4.2, 4.4, 4.5$  are simulated, all with  $h_b = 0.3h_p$ . The corresponding optimal bending stiffness and optimal bandwidth are obtained in Figure 2.9. Here, the bandwidth is defined as the frequency range within which the transmission loss curve is above an arbitrarily chosen value  $TL = 10dB$ .

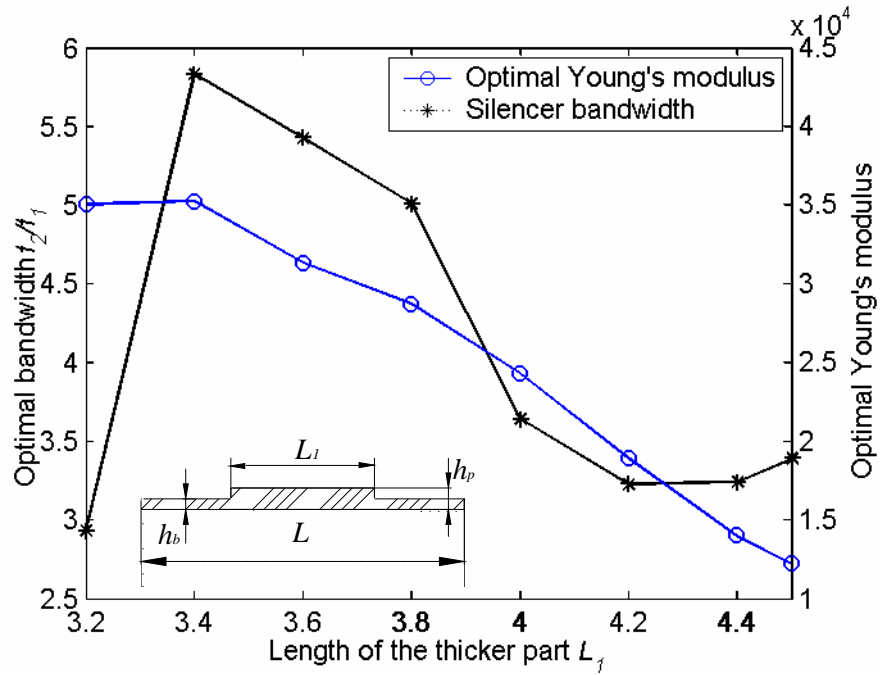


Figure 2.9: Effect of the length of the middle part on optimal bending stiffness and silencer bandwidth when mass ratio=1.

Figure 2.9 shows the trends of both the optimal bandwidth and the optimal Young's modulus with the increasing length of the thicker part  $L_1$ . When  $L_1$  increases from 3.2 to 3.4, there is a dramatic increase in the optimal bandwidth curve. However, within the range  $3.4 \leq L_1 \leq 4.2$ , the optimal bandwidth continuously decreases, and then has a slight increase when  $4.2 \leq L_1 \leq 4.5$ . Compared with the curve of the optimal bandwidth, the optimal bending stiffness curve is much simpler. There is only a slight increase within the range of  $3.2 \leq L_1 \leq 3.4$ , and for the rest values of  $L_1$ , it continues reducing. To understand the change of the two curves, the transmission loss spectra when  $L_1=4.0, 3.8, 3.4$  and  $3.2$  are shown in Figure 2.10 as an illustration:

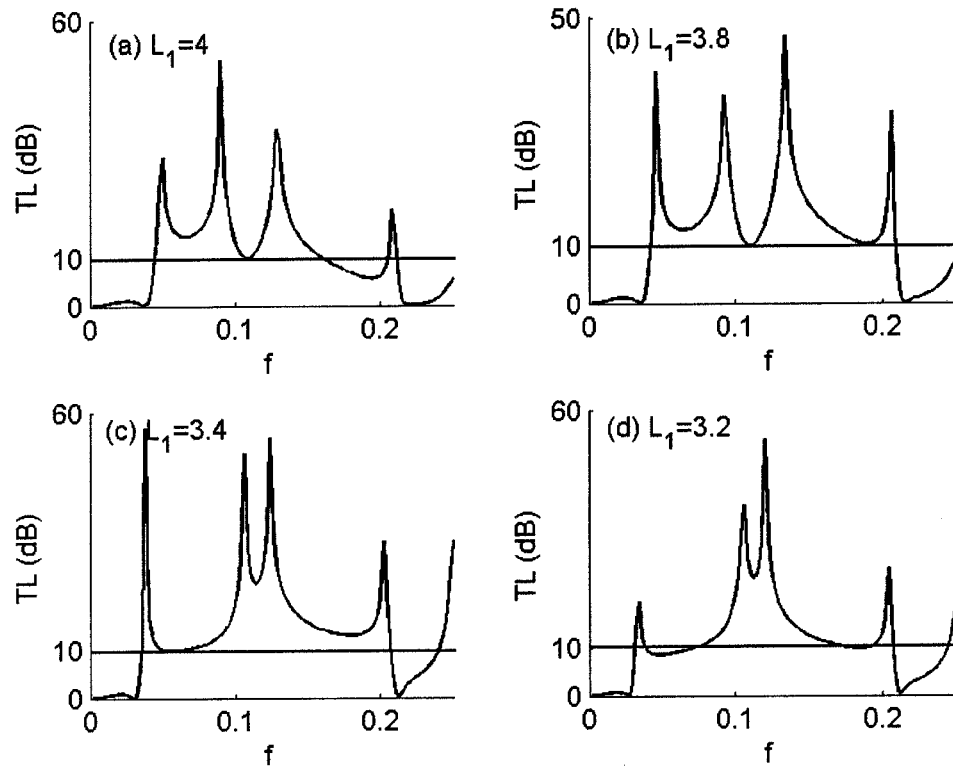


Figure 2.10: Transmission loss spectra of the non-uniform plate with  $L_1=4.0, 3.8, 3.4, 3.2,$  and the same dimensionless density of  $\rho=20$

In all the subfigures of Figure 2.10,  $TL=10dB$  is marked by a solid line. Actually,  $TL=10dB$  is used here as a reference not a strict standard. Slight departure of the transmission loss spectrum from  $10dB$  is acceptable, and can be modified through tempering the values of the Young's modulus  $E$ . By revising the Young's modulus, the values of the critical trough can be elevated to above  $10dB$ .

It can be found in Figure 2.10 (a) that when  $L_1=4$ , there are three peaks above the criterion line without any breaks. When  $L_1$  reduces, the second and third peaks begin to move close to each other, and the left-shifted third peak will lift the trough between the third and fourth peaks. Finally, the trough will increase to above  $10dB$ , and four peaks appear in the stopband of the  $TL$  spectrum, as shown in Figures 2.10(b) and 2.10(c). This is why there is a big increase between  $L_1=4$  and  $L_1=3.8$ . However, when  $L_1$  continues reducing, the right-shifted second peak will deteriorate the trough between the first and second peaks, and finally results in a trough below  $10dB$ , leaving only three peaks above the criterion line without any breaks. In this way, the reduction from the four peaks to three peaks finally leads to a truncated stopband, making the performance of the plate not as good as the former situations, and this is also why there is a dramatic drop in the optimal bandwidth curve between  $L_1=3.4$  and  $L_1=3.2$ . The detailed explanations about the peak number changes will be described in the following section.

To check the accuracy of the FEMLAB solver, the energy conservation in the coupled system is examined. In the present model, the reflected sound energy is obtained by integrating the velocity potential at the inlet boundary, and the transmitted sound energy is obtained by the same integration at the outlet boundary. The addition of the reflected sound energy and the transmitted sound energy should be equal to the specified incident sound energy. The deviation indicates the

---

computational error. Dividing the error by the incident sound energy, the normalized error is obtained. The process of the normalized error calculation can be expressed as:

$$\frac{\delta E}{\int_{inlet} |\phi_{in}|^2 dy} = \frac{\overbrace{\int_{inlet} |\phi - \phi_{in}|^2 dy}^{\text{reflected sound energy}} + \overbrace{\int_{outlet} |\phi|^2 dy}^{\text{transmitted sound energy}}}{\int_{inlet} |\phi_{in}|^2 dy} - 1. \quad (2.28)$$

where subscripts ‘in’ denote incident wave evaluated at the inlet boundary. Based on the given mesh, the normalized error spectrum over the dimensionless frequency range from 0.002 to 0.25 is shown in the Figure 2.11. It can be found that the result is satisfactory, and all the values are smaller than  $5 \times 10^{-8}$ .

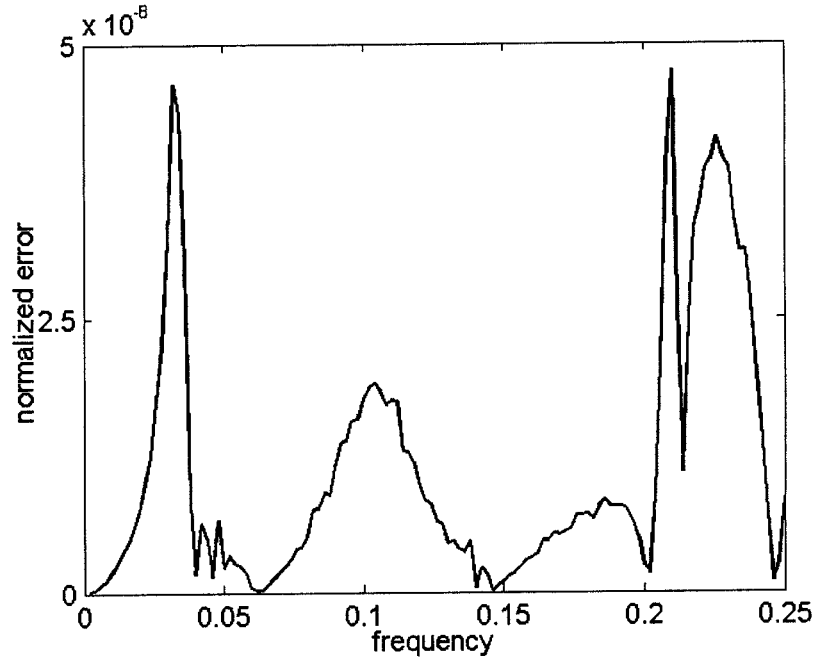


Figure 2. 11: The normalized error spectrum of the numerical model for a non-uniform plate

Another comparison between the results of the simply-supported uniform plate and the clamped non-uniform plate is also conducted. In the comparison, both of the models have the same mass ratio of  $m=0.776$ . Figure 2.12 shows that there are three peaks within the stopband, ranging from  $f_{1s} = 0.0354$  to  $f_{2s} = 0.157$ , for the simply-supported uniform plate, while four peaks for the clamped non-uniform plate, ranging from  $f_{1c} = 0.0354$  to  $f_{2c} = 0.2065$ . Comparing the optimal results of the two different models, it can be found that the clamped non-uniform plate has an even wider stopband than that of the simply-supported one. This is because although the clamped boundary condition imposes more restrictions on the plate than the simply-supported boundary condition, the thinner ends of the non-uniform

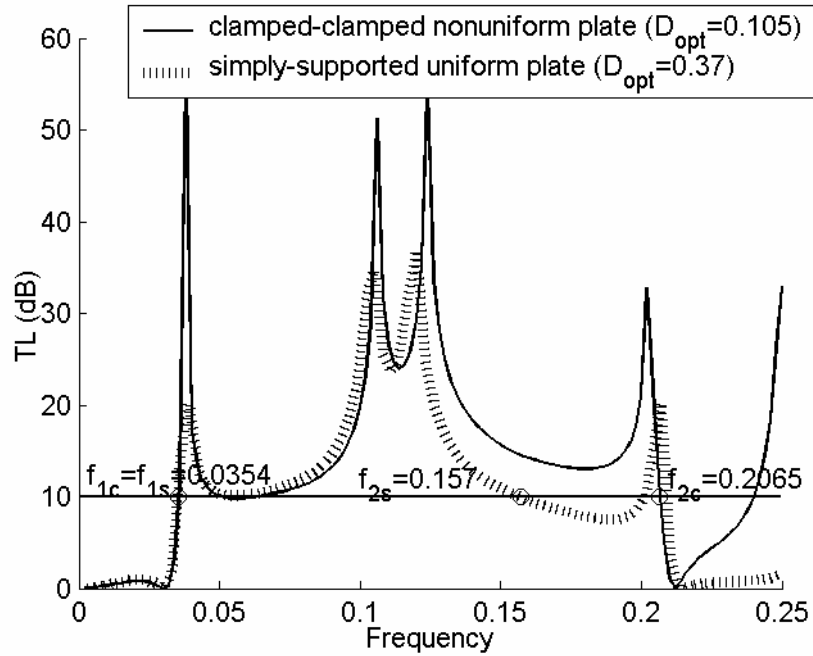


Figure 2. 12: Comparison about the optimal performance between the simply-supported uniform plate and the clamped non-uniform plate ( $L_1=3.4$ ), both of which have the same mass ratio  $m=0.776$ . The solid line is the result of the clamped non-uniform plate with  $L_1=3.4$ , and the dotted line is that of the simply-supported uniform plate.

plate weaken the restrictions, and makes it effectively longer than the simply-supported uniform plate. In this way, an even wider effective frequency band is obtained.

The mass ratio and the bending stiffness are also two key elements for the plate-type wave reflector. For each mass ratio  $m$ , there is an optimal Young's

modulus  $E_{opt}$ . Here, a non-uniform plate, with the specified dimensions  $L_1=3$ ,  $L=5$ ,  $h_b=0.025$  and  $h_p=0.05$  is explored. The results are shown in Figure 2.13. It is found that, when the mass ratio increases, the optimal bending stiffness increases, but the stopband width shrinks. It is concluded that low mass ratio is preferable in the plate-type wave reflector. However, Figure 2.13 also shows that the optimal performance requires a mass ratio and bending stiffness not normally seen in usual homogeneous materials. Therefore, to find a material or structure with low mass ratio and required high bending stiffness is an important task for experiments.

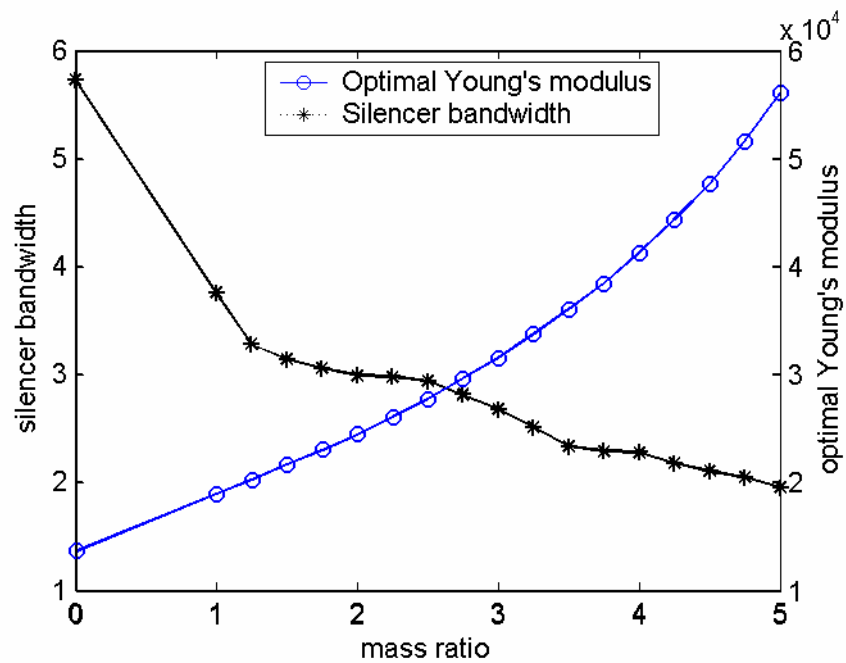


Figure 2.13: Effect of the mass ratio on optimal bending stiffness and silencer bandwidth.

## 2.5 Modal analysis

### 2.5.1 The simply-supported uniform plate

As stated in the former sections, the governing equation for the plate vibration is the dynamics equation of plate:

$$m_s \frac{\partial^2 \eta}{\partial t^2} + D \frac{\partial^4 \eta}{\partial x^4} + (p_i + \Delta p) = 0. \quad (2.29)$$

When a harmonic incident wave  $p_i = e^{i(\omega t - k_0 x)}$  comes, the plate will be excited to vibrate harmonically. If the plate vibration velocity  $V = \partial \eta / \partial t = i\omega \eta$  is used here as the variable, Eq. (2.29) is rewritten as:

$$m_s i\omega V + \frac{D}{i\omega} \frac{\partial^4 V}{\partial x^4} + (p_i + \Delta p) = 0 \quad (2.30)$$

The equation above can be expressed by the standard Galerkin procedure, in which  $V$  is expanded as a series of *in vacuo* modes with modal amplitude  $V_j$ :

$$V_j(t) = \frac{2}{L} \int_{-L/2}^{L/2} V(x, t) \sin[j\pi(x/L + 1/2)] dx \quad (2.31)$$

In this case, Eq. (2.30) can be expressed in the form of:

$$\begin{aligned} \ell_j V_j + \frac{2}{L} \int_{-L/2}^{L/2} (p_i + \Delta p) \sin[j\pi(x/L + 1/2)] dx &= 0 \\ \ell_j &= m_s i\omega + \frac{D}{i\omega} \left(\frac{j\pi}{L}\right)^4 \quad j = 1, 2, 3, \dots \end{aligned} \quad (2.32)$$

The modal response for the plate is described by several parameters: all the individual plate vibration modes,  $V_j$ ,  $j = 1, 2, 3, \dots, N$ , the complex amplitude of

the reflected sound by the induced vibration of the  $j$ th mode with unit amplitude  $R_j$ , the contribution of each single mode to sound reflection,  $V_j R_j$ , and the modal reflection contribution to the final sound reflection  $\gamma_j$ . All the expressions of these parameters can be referred to in (Huang, 2002). Figure 2.14 shows the variation of these parameters with changing frequencies.

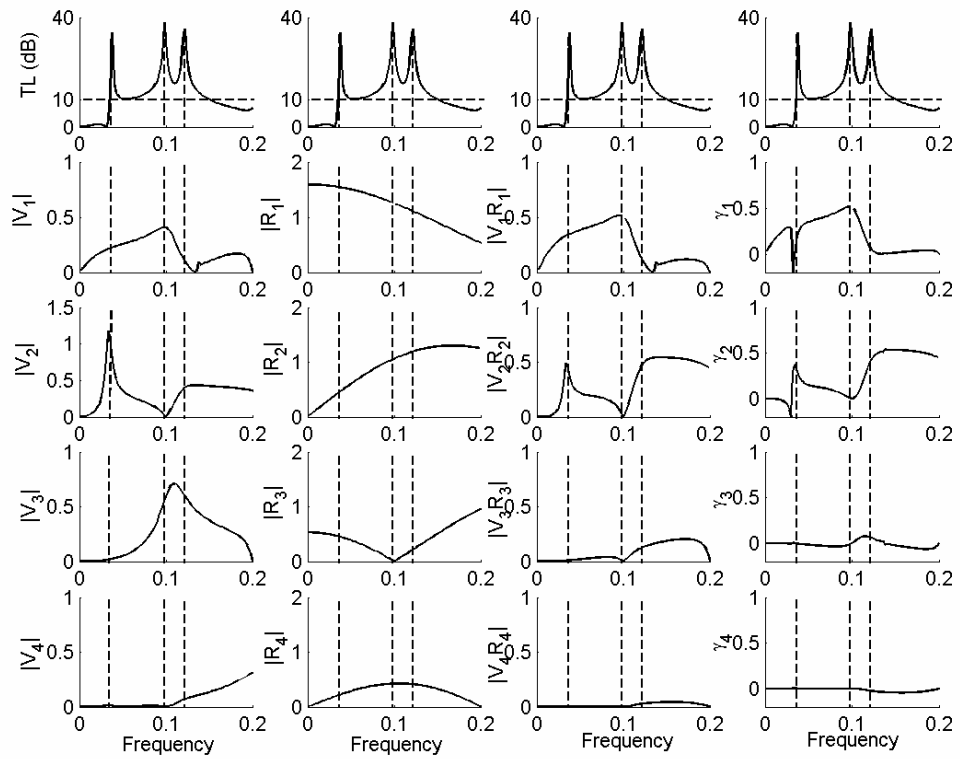


Figure 2.14: Modal reflections. The first column is the modal amplitude  $|V_j|$ , the second column is the modal reflection coefficient  $|R_j|$ , the third column is the single mode reflection  $|V_j R_j|$ , and the last column is the modal contribution  $\gamma_j$ . The top row is the TL spectrum as a reference of some important frequencies.

In Figure 2.14, the vibration amplitude of each individual mode  $|V_j|$ , the modal reflection coefficient  $|R_j|$ , the single mode reflection  $|V_j R_j|$ , and the modal contribution  $\gamma_j$  are all shown in the frequency range between 0 and 0.2. It makes it easy to identify the relationships between all these factors at some particular frequencies. From Figure 2.14, it is found that the transmission loss curve is not simply determined by the modal amplitude  $|V_j|$ , but by a combination of the mode reflection  $|V_j R_j|$  and the modal contribution  $\gamma_j$ . Further modal analysis concentrated on the three peak points is conducted in the following.

As explained in (Huang, 2002), the higher order modes contribute little to the radiation impedance,  $Z_{-jl}$ , and reflection impedance,  $Z_{rjl}$ . Therefore, only the plane wave mode,  $n=0$ , is analyzed for  $f \leq 0.2$ .

Although there is a complicated inter-modal coupling, there is no coupling between the odd and even modes in the modal radiation impedance  $Z_{jl}$ , which means  $Z_{odd,even} = Z_{even,odd} = 0$ . Coupling still exists among all the odd modes and among all the even modes. As shown in the former studies, with the plane wave approximation, in the frequency range where the first two modes are quite decoupled from the higher order modes, the coupling among all the odd modes and

---

among all the even modes are so weak that it can be simplified by the first two modes, and expressed as

$$V_1 \approx \frac{-I_1}{Z_{11} + \ell_1}, \quad V_2 \approx \frac{-I_2}{Z_{22} + \ell_2}. \quad (2.33)$$

The radiation impedance,  $Z_{11}$  and  $Z_{22}$  can be expressed as

$$\begin{aligned}
 Z_{11} = & \overbrace{\left[ (2L) \frac{2\pi^2(1 + \cos \theta)}{[\pi^2 - \theta^2]^2} \right]}^{\text{Radiation resistance}} \\
 & \overbrace{-i(L_c + 2L) \left[ \frac{2\pi^2 \sin \theta}{[\pi^2 - \theta^2]^2} - \frac{\theta}{\pi^2 - \theta^2} \right]}^{\text{Radiation resistance (stiffness)}} \\
 & \overbrace{-iL_c \left[ \frac{2\pi^2(1 + \cos \theta)}{[\pi^2 - \theta^2]^2 \tan(\theta/2)} \right]}^{\text{Cavity reflection reactance (stiffness)}}. \\
 \\
 Z_{22} = & \overbrace{\left[ (2L) \frac{8\pi^2(1 - \cos \theta)}{[(2\pi)^2 - \theta^2]^2} \right]}^{\text{Radiation resistance}} \\
 & \overbrace{+i(L_c + 2L) \left[ \frac{8\pi^2 \sin \theta}{[(2\pi)^2 - \theta^2]^2} - \frac{\theta}{(2\pi)^2 - \theta^2} \right]}^{\text{Radiation resistance (stiffness)}} \\
 & \overbrace{+iL_c \left[ \frac{8\pi^2(1 - \cos \theta) \tan(\theta/2)}{[(2\pi)^2 - \theta^2]^2} \right]}^{\text{Cavity reflection reactance (stiffness)}}. \quad (2.34)
 \end{aligned}$$

where  $\theta = k_0 L$ .

The first plate mode is rather stiff for very low frequencies mainly due to the cavity reflection effect. It is concluded that the structural mass is not important at all for the first mode response at low frequencies. The very high stiffness in the low-frequency range also indicates that the first mode cannot be relied upon for sufficient plate reflection of the grazing incident sound. Therefore, although the first mode response is the most effective in sound reflection, the second mode resonance is an important factor to analyze.

### **Second mode resonance**

For the second mode,  $j=2$ ,  $\theta$  in  $[(j\pi)^2 - \theta^2]$  can be ignored for a rough estimate without loss of qualitative information. The impedance  $Z_{22}$  and the incident wave coefficients  $I_2$  are approximated as follows:

$$4\pi^2 Z_{22} \approx (4L)(1 - \cos \theta) + i(L_c + 2L)[2 \sin \theta + \theta] + iL_c 2(1 - \cos \theta) \tan(\Theta/2) \quad (2.35)$$

$$I_2 \approx \frac{1}{\pi} e^{i\theta/2} (1 - e^{-i\theta}).$$

In this way, the second mode response can be derived as:

$$V_2 \approx \frac{-I_2}{Z_{22} + \ell_2} = \frac{-i4\pi L^{-1}}{8 \sin(\theta/2) + iX},$$

$$X = (h_c^{-1} + 2) \left[ 4 \cos(\theta/2) + \theta / \sin(\theta/2) \right] + 4h_c^{-1} \sin(\theta/2) \tan(\Theta/2) \quad (2.36)$$

$$+ \left( \frac{2\pi}{L} \right)^2 \left[ m\theta - \frac{DL^2}{\theta} \left( \frac{2\pi}{L} \right)^4 \right] / \sin(\theta/2).$$

A resonance occurs when the denominator of the second mode response is the minimum value, and the minimum value can be approximately said to happen where the reactance term  $X$  has its minimum value. Here, a very small  $\theta$  is assumed, and the corresponding  $\Theta$  is also very small. With this assumption, the values of  $\sin(\theta/2) \approx \theta/2$ ,  $\tan(\Theta/2)$  can be approximated to zero, while  $\cos(\theta/2)$  approaches 1. Therefore, the approximated resonance condition  $X=0$  can be simplified as

$$3(h_c^{-1} + 2) + \left(\frac{2\pi}{L}\right)^2 \left[ m - \frac{D}{(L\theta)^2} (2\pi)^4 \right] \approx 0 \quad (2.37)$$

From this equation, the second mode resonance frequency can be determined as

$$f_{2res} \approx \frac{1}{L} \left(\frac{2\pi}{L}\right)^2 \sqrt{\frac{D}{3(h_c^{-1} + 2) + m \left(\frac{2\pi}{L}\right)^2}}. \quad (2.38)$$

For the present mindlin plate model, dimensionless Young's modulus  $E=12480$  is used, whose corresponding dimensionless bending stiffness  $D$  is

$$D = EI = E \frac{a^3 b}{12} = 12480 \times \frac{(0.05)^3 \times 1}{12} = 0.13.$$

Together with the parameters  $m=1, L=5, h_c=1$ , the approximate second mode resonance frequency can be determined as

$$f_{2res} \approx \frac{1}{L} \left(\frac{2\pi}{L}\right)^2 \sqrt{\frac{D}{3(h_c^{-1} + 2) + m \left(\frac{2\pi}{L}\right)^2}} = 0.035.$$

The accurate root for resonance condition  $X=0$  is  $f_{2res} = 0.0339$  as shown in the left column  $|V_2|$  of Figure 2.14. The most influential parameter for the second mode resonance frequency is the plate length  $L$ .

**Peak performance points for simply-supported plate:**

Here, the transmission loss spectrum of the simply-supported uniform plate, Figure 2.15, is attached as a convenient reference.

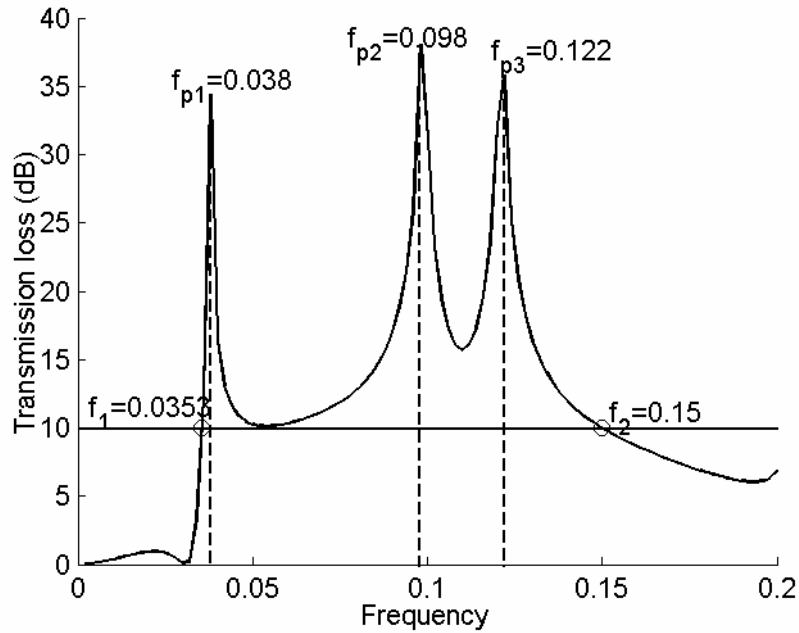


Figure 2.15: Transmission loss spectrum of the simply-supported plate with  $m=1$  &  $D=0.13$

There are three peaks in the stopband, located at  $f_1 = 0.038$ ,  $f_2 = 0.098$  and  $f_3 = 0.122$ , respectively. To find the modal interference patterns of the three peaks, a modal analysis is conducted for the peaks in this section.

The first peak, P1, is firstly analyzed in Figure 2.16:

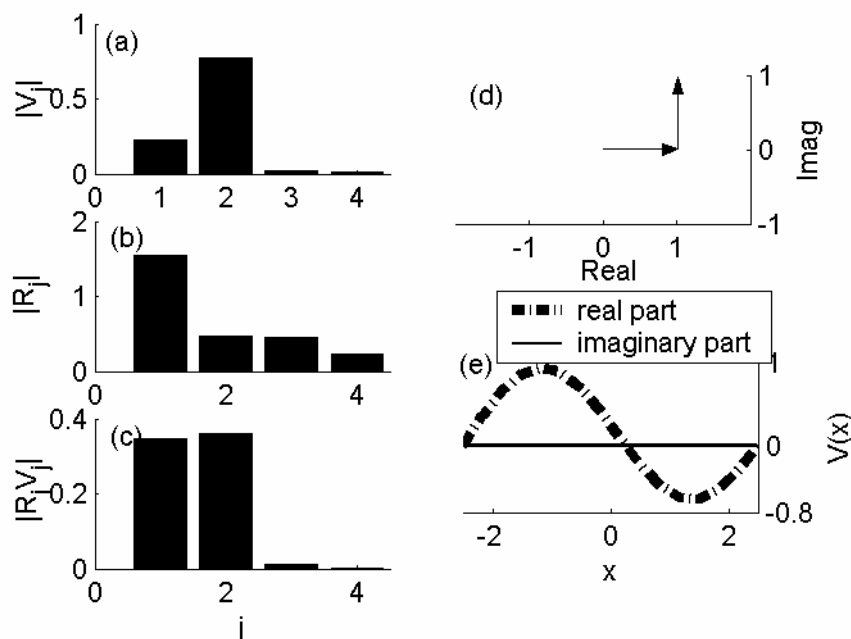


Figure 2.16: The response of the plate at the first peak  $f_1 = 0.038$ , P1. (a) shows the velocity amplitude of each mode,  $|V_j|$ . (b) is the amplitude of the modal reflection coefficient  $|R_j|$ . (c) is the sound reflection by each mode alone,  $|R_j V_j|$ . (d) shows how the complex modal contributions add up. (e) is the real and imaginary parts of the plate vibration velocity distribution,  $V(x)$ .

The velocity amplitude of each mode  $|V_j|$ , the amplitude of the modal reflection coefficient  $|R_j|$ , and the sound reflection by each mode alone,  $|R_j V_j|$  are shown in Figures 2.16(a), 2.16(b), and 2.16(c), respectively. According to Figure 2.16(a),

it is found that the plate vibration mode shape is mainly composed of the first two modes, and can be expressed as  $\sin(\pi\xi) + 3.44\sin(2\pi\xi)$ , whose shape resembles a distorted second mode with the left half-length extended and the right half-length reduced. Although the amplitude of the first mode is smaller than that of the second mode, because the amplitude of the first mode reflection coefficient  $|R_1|$  is larger than  $|R_2|$ , there is not big difference between the final amplitudes of  $R_1V_1$  and  $R_2V_2$ . Besides, at  $f_1 = 0.038$ , the phase angle of the contribution of the first mode,  $R_1V_1$ , is  $173.06^\circ$ , and the phase angle of the contribution of the second mode,  $R_2V_2$ , is  $261.97^\circ$ . The phase difference between  $R_1V_1$  and  $R_2V_2$  is  $88.91^\circ$ , nearly out-of-phase, therefore, there is no interference between the first two modes. As shown in Figure 2.16(e), the imaginary part of plate vibration velocity  $V(x)$ , shown as the thin solid line, is about zero, which means the plate vibrations are almost in-phase.

The performance of the second peak is shown in Figure 2.17. As shown in Figure 2.17 (a), the amplitudes of the second mode and the fourth mode almost vanish to

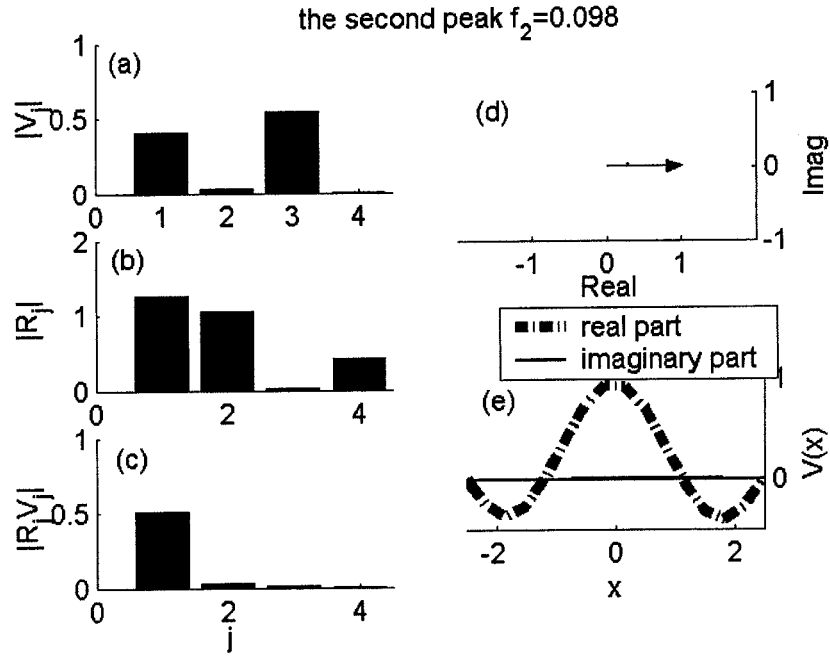


Figure 2.17: The response of the plate at the second peak

zero, because of the effect of the first cavity mode. The plate vibration mode shape can be expressed as  $\sin(\pi\xi) - 1.35\sin(3\pi\xi)$ . Together with the effect of modal reflection coefficient, only the first mode contributes to the wave reflection. At the second peak, the phase difference between  $R_1V_1$  and  $R_3V_3$  is  $179.67^\circ$ , which means the first mode and the third mode is in-phase with each other.

The response of the third peak is analyzed in Figure 2.18. Different from the former two peaks, the amplitude of the first mode is very small, and the plate vibration mode shape can be expressed as  $\sin(2\pi\xi) - 1.48\sin(3\pi\xi)$ . At the third peak, the

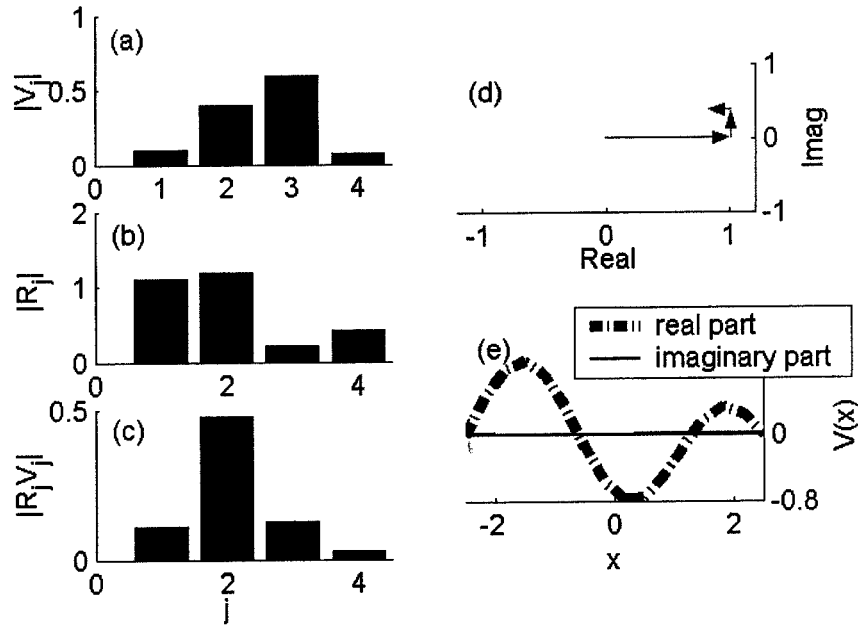


Figure 2.18: The response of the plate at the third peak  $f_3 = 0.122$

the phase difference between  $R_2 V_2$  and  $R_3 V_3$  is  $90.9^\circ$ . It shows a roughly in-phase relationship between the first mode and the third mode. As shown in Figure 2.18(e), the combination of the second mode and the third mode makes the plate vibration mode shape like a distorted third mode.

To understand the spectral pattern shift in Figure 2.3 with the changing  $D$ , the following exploration is conducted. In Figure 2.19, the relationships between the peak positions of the transmission loss and the interference between the even modes and odd modes are shown. The plates with three different values of the bending stiffness,  $D=0.13$  (optimal value),  $D=0.135$  and  $D=0.115$ , are studied as

illustrations. Because the summation of the complex amplitudes can be expressed as vectorial sum on the real-imaginary plane, the contributions from all the odd modes,  $j=1, 3, 5, \dots$ , towards the reflected wave can be classified as  $V_{odd}R_{odd}$ , and those for the even modes, with the indices  $2, 4, 6, \dots$ , can be classified as  $V_{even}R_{even}$ . As described above, when the index of the mode exceeds 25, there won't be any noticeable differences, therefore, the first 25 modes are included in the calculation.

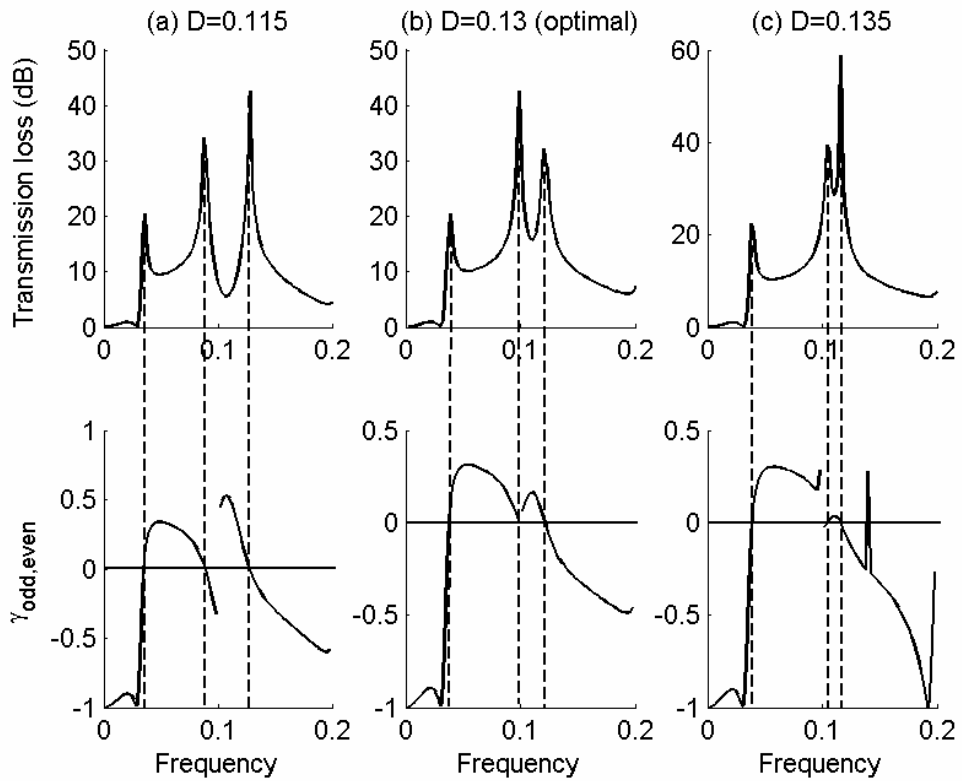


Figure 2.19: Relationships between the peak positions in the transmission loss spectra and the interference between the even modes and odd modes

In Figure 2. 19, the three subfigures in the first row describe the transmission loss curve of the plate with three different bending stiffness,  $D=0.13$ ,  $0.135$  and  $0.115$ . The other three subfigures in the second row just show the corresponding interference between the even modes,  $V_{even}R_{even}$ , and odd modes,  $V_{odd}R_{odd}$ , by a parameter,

$$\gamma_{odd,even} = \cos \theta, \quad (2.39)$$

where  $\theta$  is the phase angle difference between the complex amplitudes of  $V_{odd}R_{odd}$  and  $V_{even}R_{even}$ .

From Figure 2.19, it is found that the three peaks in the transmission loss curve occur at the frequencies where the odd modes and the even modes have no interference. Note that there are disconnections in the three lower subfigures,

$\gamma_{odd,even}$ , at the frequency  $f=0.1$ , which are caused by the singular division  $\frac{0}{0}$ .

Although the division has finite results, the figures in Figure 2.19 are still kept disconnected for the purpose of identifying locations where  $\gamma_{odd,even} = 0$ .

### **2.5.2 The clamped non-uniform plate**

As shown in the preceding sections, there are four peaks within the stopband for the optimal performance of the non-uniform plate. To avoid the repetition with the analyses above, only the vibration velocity distributions at the peak points are

---

analyzed in this section. Comparison between the clamped non-uniform plate and the simply-supported uniform plate are made in Figure 2.20.

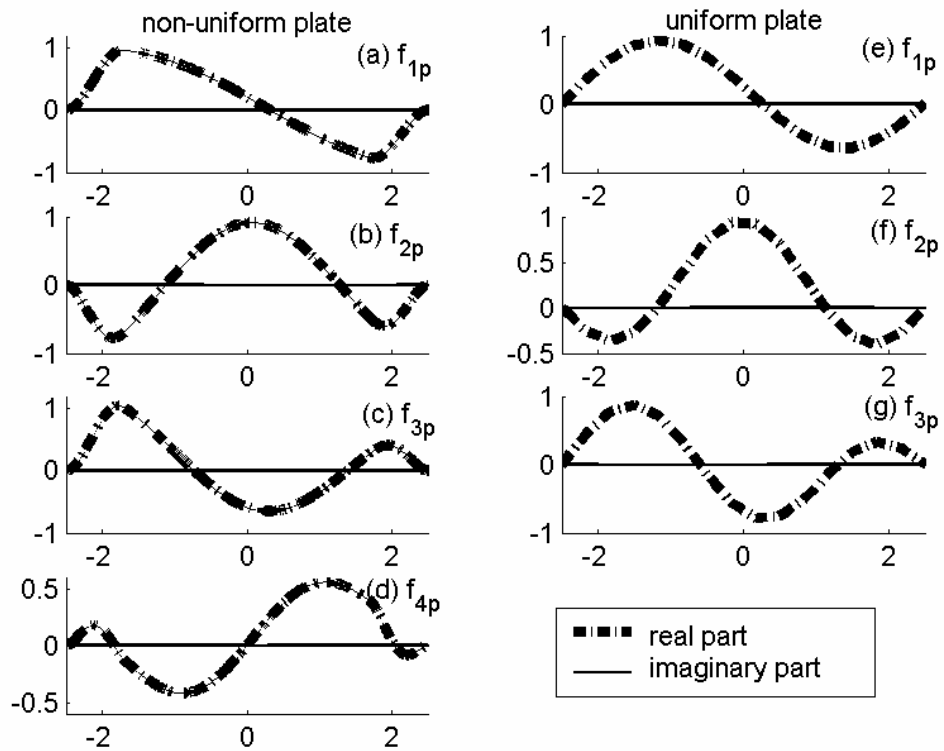


Figure 2.20: The comparisons of the vibration velocity distributions at the peak points between the clamped non-uniform plate (left column, from (a) to (d)) and the simply-supported uniform plate (the right column, from (e) to (g)).

In the subfigures in the left column of Figure 2.20, the vibration velocity distributions of the clamped non-uniform plate are displayed, while the subfigures on the right are for the simply-supported uniform plate. From the comparisons of

the first three peak points of the two plates, it is found that the vibration velocity distribution of the clamped non-uniform plate is not as smooth as that of the simply-supported uniform plate. This is so because although the vibration modes of the clamped non-uniform plate is similar to those of the simply-supported uniform plate, the two conjunctions between the thinner ends and the middle part still make the modes not that smooth.

## Chapter 3: Three-dimensional effects

### 3.1 Introduction

The former chapter focuses on some two-dimensional models for three different types of plate-type wave reflector, a uniform plate with two simply-supported ends, a uniform plate with two clamped ends and a non-uniform plate with clamped ends. In all the two-dimensional plate models, their two longitudinal edges are free to vibrate. Because the two edges are free, when the incident wave is a plane wave, there is no excitation along the lateral direction, which means that the lateral vibration of the plate is in step with the whole width of the plate.

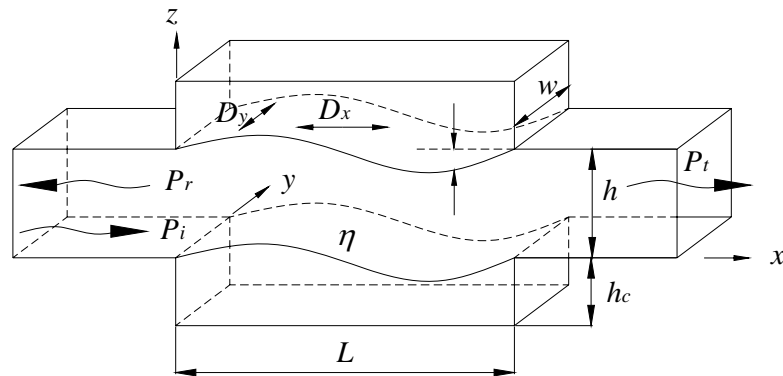


Figure 3.1: The configuration of a three-dimensional plate-type wave reflector with two identical bending stiffness plates. Each cavity has a length of  $L$ , depth  $h_c$  and width  $w$

Figure 3.1 shows a three-dimensional configuration for the plate-type wave reflector. The two free edges give the plate no restrictions for vibration, and hence make the plate more effective in sound reflection. However, due to the Poisson's ratio of the plate material, when the plate vibrates, it always has a deformation along the lateral direction. Such a deformation requires that there should be a necessary gap in a real model between the plate and the actual test-rig to keep the no touch condition of the two-dimensional model. Figure 3.2 illustrates the non-uniform plate with two clamped edges and two gaps of width  $\tau$  between the two plate longitudinal edges and the duct.

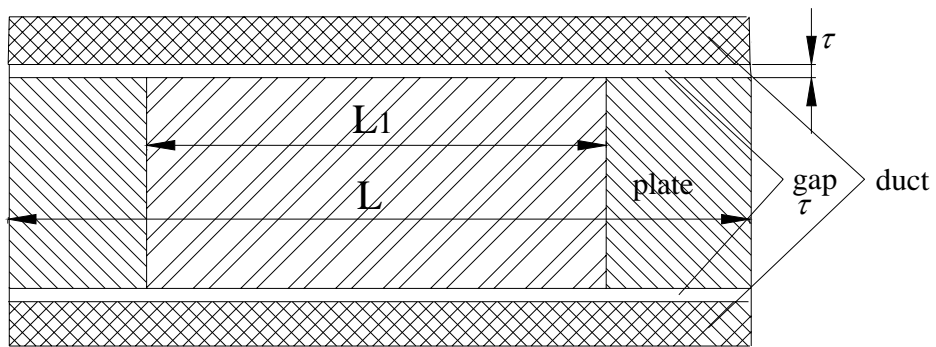


Figure 3.2: Top view of the non-uniform plate and the duct with a gap of specified dimensions  $\tau$  between them

Nevertheless, the gap always leads to acoustic leaking, and even a very small gap may cause much influence on the final performance of the reflector, and makes the transmission loss curve look like an expansion chamber, especially in the low frequency range. Some explorations about the effect of the gap have been

conducted (Cheung *et al.*, 2005), in which the transmission loss spectra of both a plate and membrane under the excitation of normal incident waves are studied. In these studies, finite element simulation is adopted to study the gap effect for different values,  $\tau = 0, 0.2\text{mm}, 0.5\text{mm}$  and  $1\text{mm}$ , and the transmission loss spectra with  $\tau = 0, 0.5\text{mm}, 2\text{mm}, 4\text{mm}$  and  $6\text{mm}$  are measured in experiment. By comparing the result with no gap and that with different gap sizes, it is concluded that when the gap is smaller than  $0.5\text{mm}$ , the final results of the plate or membrane won't be much influenced. Note that the duct height was  $10\text{mm}$  in all these studies.

In the present studies, the plate is installed parallel to the direction of the incident waves, instead of the normal direction. However, no matter what direction the plate is placed, the same mechanism of the gap is shared, and hence the safe gap for both the studies should be the same.

The strict requirement for gap size makes it difficult to adjust the plate exactly the desired size in implementation. If the width of the plate isn't within the required range, friction or leakage will happen. Friction happens when some parts of the plate are wider than the actual width of the duct wall. The interface will become a constraint to the plate, and makes the plate not vibrate with two free edges, which finally greatly reduces the reflection capability of the plate. Leakage happens where the gap size exceeds the range, and makes the behavior of the expansion chamber dominant.

Actions have been taken to reduce the leakage, such as adding some soft connections along the two long sides of the plate to cover the small gap between the duct wall and the plate. A 1mm-thick rubber strips and blu-tack strips were tried in our experiment. One side of the strip connects the long side of the plate, and the other side of the strip is fixed. By doing so, although the leakage is reduced, the reflection ability of the plate also reduces. This is because the gap is very small, 1mm wide in our experiment, although the rubber strips and the blu-tack strips are very soft, when they are only 1mm wide, their transverse bending stiffness is very high, and makes the two long sides of the plate like being fixed.

Under this situation, the most secure model would be one in which the lateral edges are also simply-supported or clamped. However, such a model gives rise to lateral bending moments, which is expected to harm the performance of the silencer (Huang & Choy, 2005). To reduce the negative effect of the lateral bending stiffness, a composite plate, in which the lateral bending stiffness is much lower than the axial bending stiffness, might be helpful. However, such a structure is also too complicated to be realized in real life. Therefore, in this chapter, theoretical studies on the three-dimensional effects of the plate are conducted.

### **3.2 Clamped lateral edges**

It is concluded in the preceding section that if the gap  $\tau$  is larger than 0.5mm, the performance of the plate-type wave reflector will be greatly affected, and the transmission loss spectrum will resemble an expansion chamber. The requirement for the gap size is so strict that it loads too many difficulties on the implementation. To make the plate-type wave reflector more practical to operate, a three-dimensional model is preferred. Compared with the two-dimensional model, whose lateral edges of the plate are both free, the three-dimensional model has two fixed lateral edges instead. Two different three-dimensional models are introduced in this section. One has a uniform thickness along the lateral direction, and the other has a non-uniform thickness along the width direction. Both models have a non-uniform thickness along the longitudinal direction.

#### **3.2.1 Uniform thickness in the lateral direction**

In this model, the shape of the plate can be seen as an extruded non-uniform two-dimensional model with all four edges fixed, and its configuration is shown in Figure 3.3. The thickness of the plate is uniform along the lateral direction. Here, the width of the plate  $w$  is defined as  $w=1$ , the thickness of the two edges and the

middle part is  $h_b = 0.015$ ,  $h_p = 0.05$ , respectively, and the total length of the plate  $L=5$ . The optimal performance of such a structure can be got through changing

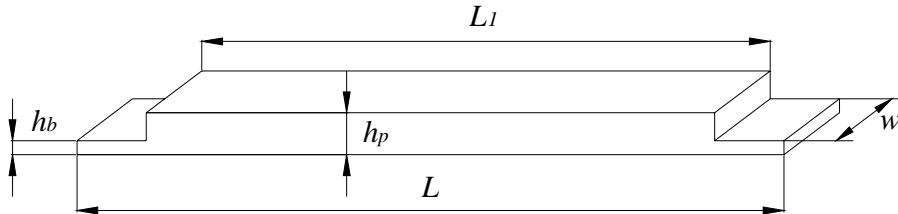


Figure 3.3: Configuration of the non-uniform plate with non-uniform thickness along the longitudinal direction and uniform thickness in the lateral direction

the length of the middle thicker part  $L_1$ , and  $L_1=4.5, 4.2, 4, 3.8, 3.6$  are specialized in the present studies.

Different from all the models in the former studies, which have two fixed edges and two other free edges, the non-uniform plate in this model has all the four edges fixed. To simulate such a three-dimensional model, three domains, each with three-dimensional geometry, are created. Generally speaking, the procedures to set up a three-dimensional model are just similar to those of the two-dimensional one. One of the major differences between them is their meshing methods.

Mesh in the three-dimensional model has its peculiar characteristics. Because the solver is restricted by the memory of the computer, there should not be too many

mesh elements in the model. Otherwise, the calculation is easy to be suspended for out of memory. A 3D mesh is either generated as an unstructured mesh containing tetrahedral elements or by extruding or revolving a 2D mesh. Creating an unstructured mesh, the number of mesh elements is determined from the shape of the geometry and various mesh parameters. The mesh parameters can be controlled by specifying the local mesh-element sizes and their distribution. An extruded or revolved mesh is structured in the direction of the extrusion or revolution. Extruding or revolving a 2D mesh into a 3D mesh, triangular elements and quadrilateral elements in the 2D mesh are extruded or revolved into prism (wedge) elements and hexahedral (brick) elements, respectively, in the resulting 3D mesh. The corresponding extruded or revolved geometry is generated together with the mesh. After defining the corresponding extrusion distances and the element layers in the extrusion direction, a new 3D geometry is generated with the defined mesh elements. The two figures in Figure 3.4 give the illustrations about both the unstructured mesh method and the extruded mesh method. In both the subfigures, the geometry created is half of the duct. The maximum edge size,  $H_{\max}$ , is specified as a dimensionless quantity normalized by the duct height  $h$ . In Figure 3.4(a),  $H_{\max}$  for the 3D quadratic air elements is 0.35, and there are totally 7626 elements generated. While in Figure 3.4(b), the maximum edge size  $H_{\max}$  is 0.55, and totally 3624 elements are generated. Compared with the unstructured mesh method, the extruded mesh method normally generates less mesh elements, which

---

can save much memory for the calculation. Therefore, the mesh extrusion method is used in our simulation.

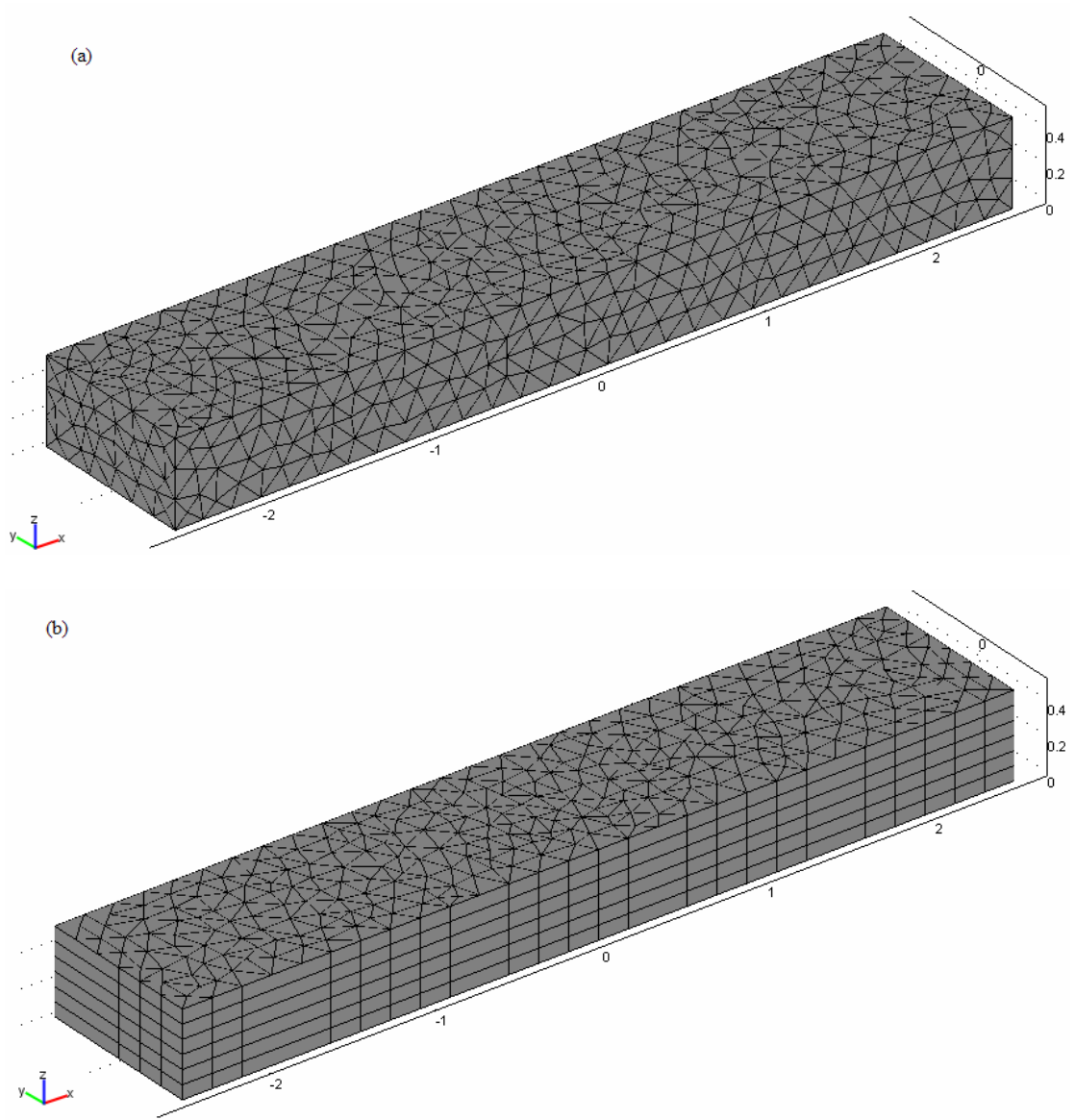


Figure 3.4: Illustrations of the unstructured mesh method (a) and extruded mesh method (b)

It is possible to completely describe the strain conditions at a point with the deformation components—(  $u, v, w$  ) in 3D—and their derivatives. The shear strain can be expressed in a tensor form,  $\varepsilon_{xy}, \varepsilon_{yz}, \varepsilon_{xz}$ , or in an engineering form,  $\gamma_{xy}, \gamma_{yz}, \gamma_{xz}$ . The normal strain components and the shear strain components are given from the deformation as follows:

$$\left. \begin{aligned} \varepsilon_x &= \frac{\partial u}{\partial x} & \varepsilon_{xy} &= \frac{\gamma_{xy}}{2} = \frac{1}{2} \left( \frac{\partial u}{\partial y} + \frac{\partial v}{\partial x} \right) \\ \varepsilon_y &= \frac{\partial v}{\partial y} & \varepsilon_{yz} &= \frac{\gamma_{yz}}{2} = \frac{1}{2} \left( \frac{\partial v}{\partial z} + \frac{\partial w}{\partial y} \right) \\ \varepsilon_z &= \frac{\partial w}{\partial z} & \varepsilon_{xz} &= \frac{\gamma_{xz}}{2} = \frac{1}{2} \left( \frac{\partial u}{\partial z} + \frac{\partial w}{\partial x} \right) \end{aligned} \right\} \quad (3.1)$$

The symmetric strain tensor  $\varepsilon$  consists of both normal and shear strain components:

$$\varepsilon = \begin{bmatrix} \varepsilon_x & \varepsilon_{xy} & \varepsilon_{xz} \\ \varepsilon_{xy} & \varepsilon_y & \varepsilon_{yz} \\ \varepsilon_{xz} & \varepsilon_{yz} & \varepsilon_z \end{bmatrix} \quad (3.2)$$

The equilibrium equations expressed in the stresses for 3D are

$$\left\{ \begin{aligned} -\frac{\partial \sigma_x}{\partial x} - \frac{\partial \tau_{xy}}{\partial y} - \frac{\partial \tau_{xz}}{\partial z} &= F_x \\ -\frac{\partial \tau_{xy}}{\partial x} - \frac{\partial \sigma_y}{\partial y} - \frac{\partial \tau_{yz}}{\partial z} &= F_y \\ -\frac{\partial \tau_{xz}}{\partial x} - \frac{\partial \tau_{yz}}{\partial y} - \frac{\partial \sigma_z}{\partial z} &= F_z \end{aligned} \right. \quad (3.3)$$

where  $F$  denotes the volume forces (body forces). Using compact notation, this relationship can be written as:

---


$$-\nabla \cdot \sigma = F \quad (3.4)$$

where  $\sigma$  is the stress tensor. Substituting the stress-strain and strain-displacement relationships in the above equation results in Navier's equation expressed in the displacement.

The stress in a material is described by the symmetric stress tensor

$$\sigma = \begin{bmatrix} \sigma_x & \tau_{xy} & \tau_{xz} \\ \tau_{xy} & \sigma_y & \tau_{yz} \\ \tau_{xz} & \tau_{yz} & \sigma_z \end{bmatrix} \quad \tau_{xy} = \tau_{yx} \quad \tau_{xz} = \tau_{zx} \quad \tau_{yz} = \tau_{zy} \quad (3.5)$$

consisting of three normal stresses ( $\sigma_x$ ,  $\sigma_y$ ,  $\sigma_z$ ) and six, or if symmetry is used, three shear stresses ( $\tau_{xy}$ ,  $\tau_{yz}$ ,  $\tau_{xz}$ ). The stress-strain relationship for linear conditions reads:

$$\sigma = D\varepsilon \quad (3.6)$$

where  $D$  is the 6 x 6 elasticity matrix, and the stress and strain components are described in vector form with the six stress and strain components in column vectors:

$$\sigma = \begin{bmatrix} \sigma_x \\ \sigma_y \\ \sigma_z \\ \tau_{xy} \\ \tau_{yz} \\ \tau_{xz} \end{bmatrix} \quad \varepsilon = \begin{bmatrix} \varepsilon_x \\ \varepsilon_y \\ \varepsilon_z \\ \gamma_{xy} \\ \gamma_{yz} \\ \gamma_{xz} \end{bmatrix} . \quad (3.7)$$


---

The elasticity matrix  $D$  and the more basic matrix  $D^{-1}$  (the inverse of  $D$ , also known as the flexibility or compliance matrix) are defined differently for isotropic, orthotropic, and anisotropic material. For isotropic material, the  $D^{-1}$  matrix is

$$D^{-1} = \frac{1}{E} \begin{bmatrix} 1 & -\nu & -\nu & 0 & 0 & 0 \\ -\nu & 1 & -\nu & 0 & 0 & 0 \\ -\nu & -\nu & 1 & 0 & 0 & 0 \\ 0 & 0 & 0 & 2(1+\nu) & 0 & 0 \\ 0 & 0 & 0 & 0 & 2(1+\nu) & 0 \\ 0 & 0 & 0 & 0 & 0 & 2(1+\nu) \end{bmatrix}. \quad (3.8)$$

Inverting  $D^{-1}$  symbolically, we can get the stiffness matrix  $D$  for 3D model:

$$D = \frac{E}{(1+\nu)(1-2\nu)} \begin{bmatrix} 1-\nu & \nu & \nu & 0 & 0 & 0 \\ \nu & 1-\nu & \nu & 0 & 0 & 0 \\ \nu & \nu & 1-\nu & 0 & 0 & 0 \\ 0 & 0 & 0 & \frac{1-2\nu}{2} & 0 & 0 \\ 0 & 0 & 0 & 0 & \frac{1-2\nu}{2} & 0 \\ 0 & 0 & 0 & 0 & 0 & \frac{1-2\nu}{2} \end{bmatrix}. \quad (3.9)$$

The boundary conditions of the three-dimensional model are identical to those of the two-dimensional case except that the plate displacement on the two sides,  $w_1, w_2$ , are different. By changing  $L_1$ , the corresponding optimal bending stiffness and optimal bandwidth are got and shown in Figure 3.5.

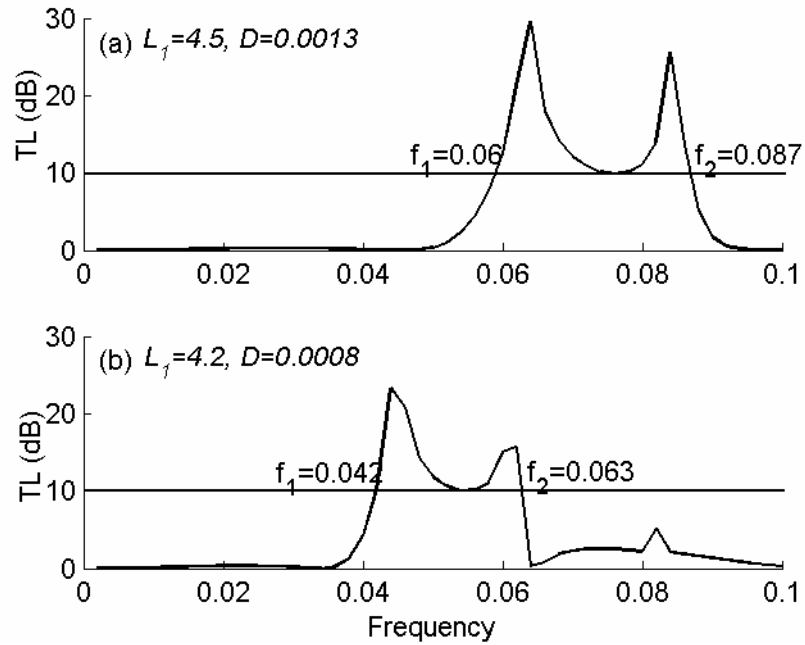


Figure 3.5: The optimal transmission loss spectra with the changing length of the middle part  $L_1$

Figure 3.5(a) shows the optimal performance of the non-uniform plate with  $L_1 = 4.5$  and Figure 3.5(b) shows that of the plate with  $L_1 = 4.2$ . The two limits of the stopband are marked in the subfigures for identification. It is found that the effective frequency band of the plate with four fixed edges is greatly reduced, because of the effect of the transverse bending stiffness. Compared with the optimal result of the  $L_1 = 4.5$ , the two peaks of  $L_1 = 4.2$  move further into the low-frequency region, but the effective frequency range shrinks.

When  $L_1$  continues reducing to  $L_1=4$ , the trough between the two peaks is always below the criteria level  $TL=10\text{ dB}$ , and breaks the two continuous peaks into two separate ones. Here, a stacked view of the transmission loss spectra is made in Figure 3.6 to demonstrate the performance of the non-uniform plate. Since there is only one peak in the low-frequency region, the optimal performance of the plate is not what we concerns any more,  $D=0.001$  is selected to illustrate the change of the results.

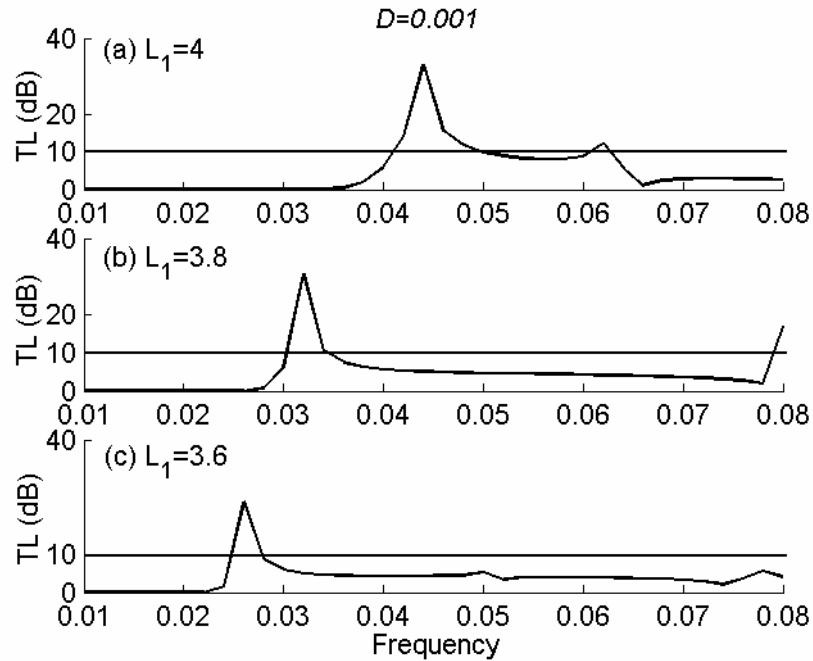


Figure 3.6: The comparisons of the transmission loss spectra with the changing length of the middle part  $L_1$  under the dimensionless bending stiffness  $D=0.001$

In Figure 3.6, the frequency region is focused from 0.01 to 0.08. When  $L_1$  reduces from 4 to 3.6, the first peak shifts to lower frequencies, and the second peak moves

downwards, until it disappears. No matter how the shape of the plate is modified, the optimal performance of this model always has only two peaks in the low-frequency region. Therefore, it is concluded that the performance of the non-uniform plate with a uniform thickness in the lateral direction is unsatisfactory.

### 3.2.2 Non-uniform thickness in the lateral direction

Due to the unsatisfactory performance of the non-uniform plate described in the preceding section, another model, a non-uniform plate, with four fixed thinner edges in both the longitudinal direction and the lateral direction, is proposed and introduced in this section. The configuration of the plate is shown in Figure 3.7:

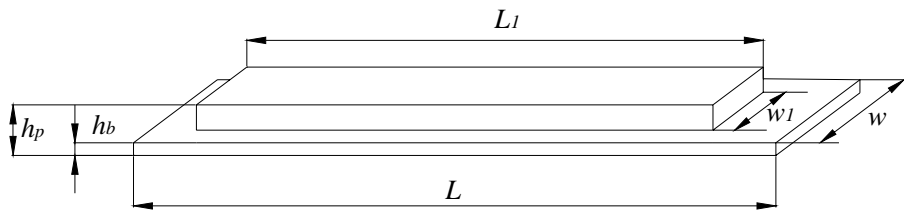


Figure 3.7: Configuration of the non-uniform plate with non-uniform thickness along both the longitudinal and lateral directions

In the present studies, the thickness of the thinner edges is still defined as  $h_b = 0.015$ , while the thickness of the middle part  $h_p = 0.05$ . Also, the total length and width of the plate are still  $L=5$  and  $w=1$ , respectively. The width of the middle part is given a moderate value  $w_l = 0.5$ . The optimal performance of the this kind

of plate can also be determined by changing the length of the middle part  $L_1$ . In this model,  $L_1=4.5, 4.2, 4, 3.8, 3.6$  are also selected as illustrations.

The simulation procedures for this model are the same as those described in the preceding section. The results are shown in Figure 3.8:

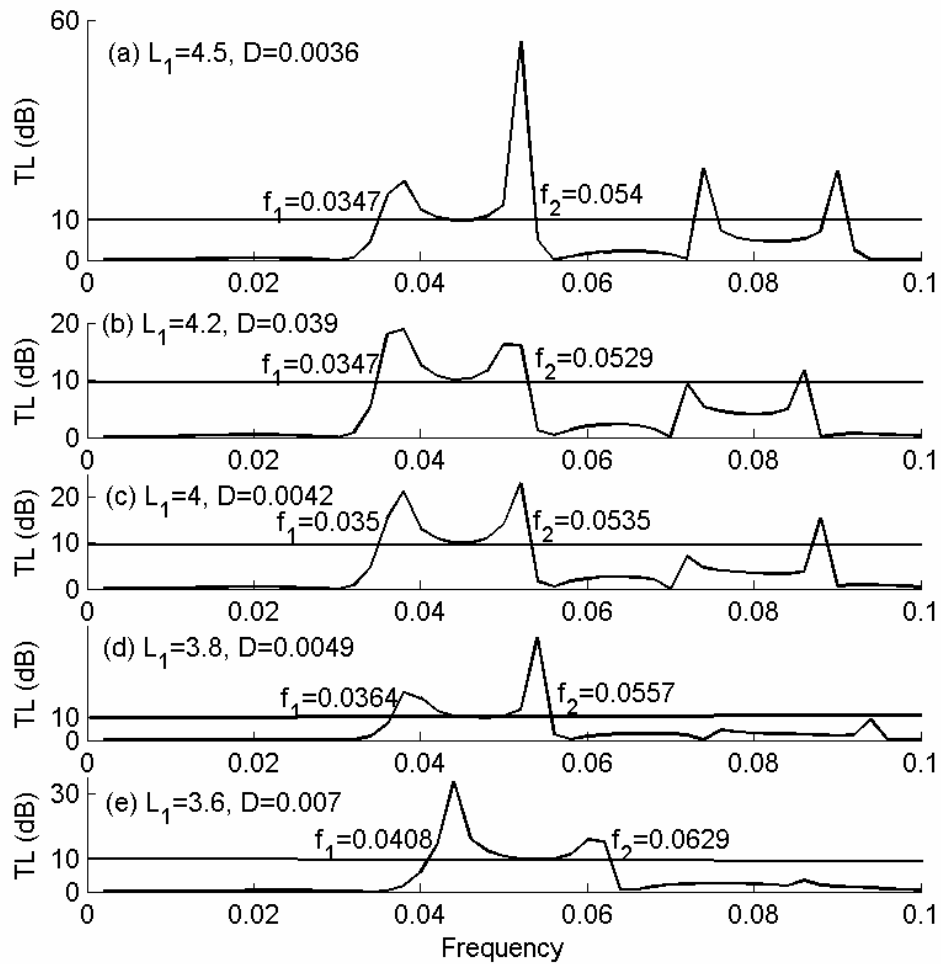


Figure 3.8: The stacked view of the optimal transmission loss spectra with the changing length of the middle part  $L_1$

In Figure 3.8, the optimal performances of the plate with five different values of  $L_1$  are included, and all the five subfigures show two peaks in the stopband. With the decreased  $L_1$ , the two peaks shift to higher frequencies, but the effective bandwidth in the five situations doesn't change much. From the results above, it is found that although the performance of the non-uniform plate with four thinner edges is better than that of the plate with two thinner edges, its optimal stopband still only contains two peaks. Therefore, it can be said that it's not an effective method to get a good performance for the three-dimensional model through changing the shape of the plate.

When  $L_1$  drops to  $L_1=3.4$ , the trough between the two peaks will move down below  $10\text{ dB}$ , and results in two distinct peaks, instead of two continuous ones. To compare the performances of the two different plate models, uniform width and non-uniform width, a comparison is made as shown in Figure 3.9. The transmission loss spectra of the plates with  $L_1 = 4.2$  and  $L_1 = 4.5$  are displayed. When  $L_1$  takes these two values, there are two peaks in both of the plate models, and the stopband is comparable. However, one of the differences between the two models is that under the same condition, the plate with four thinner edges is effective for even lower-frequency noises. Besides, according to the results above, the length range of  $L_1$ , in which two peaks appears, is wider for the plate with four thinner edges than that with two thinner edges. These differences show the plate model with non-uniform width has better performance, although the stopband in both

---

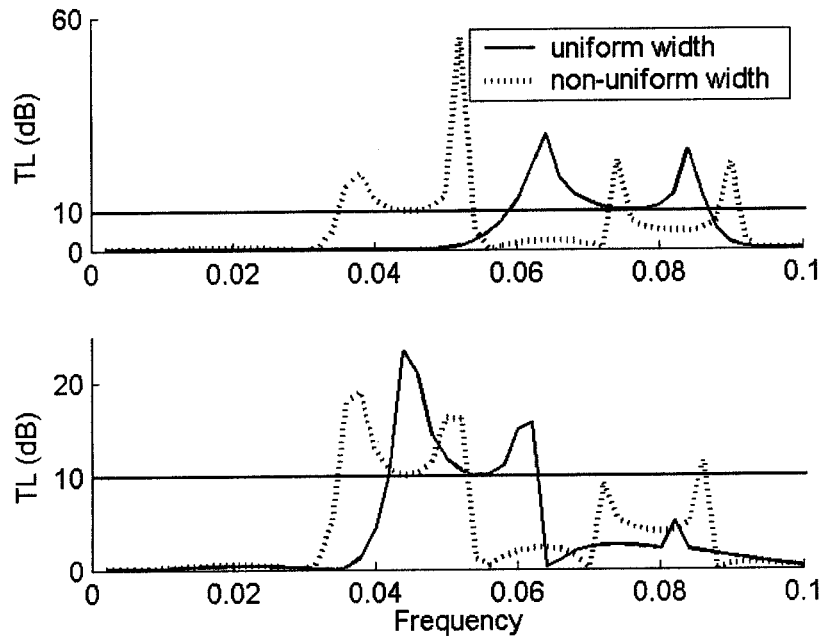


Figure 3.9: Comparison between the plates with 2 thinner edges (solid line) and with 4 thinner edges (dotted line)

models is unsatisfied. To tackle this problem, to reduce the effect of the transverse bending stiffness is the essential method. Under this situation, a corrugated plate, which promotes the effective axial bending stiffness and decreases the lateral bending stiffness, is proposed in the next section.

### 3. 3 Corrugated plate

In engineering practice, flat plates are often reinforced by ribs, stringers, or corrugations. These methods of stiffening are typically found in decking, roofing,

and sandwich plate cores. The primary objective of this reinforcement is to enhance the bending stiffness in one direction. For specific case of the plate stiffened by corrugation, it is an efficient low-cost structural material that is widely used for transporting, storing and distributing goods. For most common corrugated plates, the transverse stiffness is dramatically decreased from that of an uncorrugated plate of the same thickness. This is because most of the deformation is due to bending induced by the corrugated geometry. For the case of plates stiffened by corrugations, the stiffness of the plate in a direction transverse to the corrugation is often neglected. For thin-walled corrugated plates, the transverse stiffness is usually small in comparison to the extensional stiffness parallel to the corrugation.

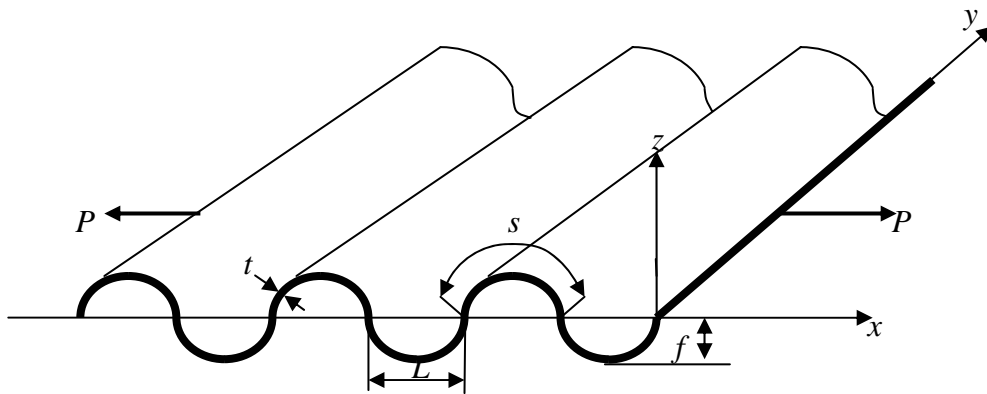


Figure 3.10: Configuration of a sinusoidal corrugated plate

For a corrugated plate with a sinusoidal shape  $z = f \sin \frac{\pi x}{L}$ , as shown in Figure 3.10, its governing differential equation of the corrugated plate is given as (Troitsky, 1976):

$$D_x \frac{\partial^4 w}{\partial x^4} + 2H \frac{\partial^4 w}{\partial x^2 \partial y^2} + D_y \frac{\partial^4 w}{\partial y^4} = q(x, y), \quad (3.10)$$

and the stiffnesses are defined as:

$$D_x = \frac{L}{s} \frac{Et^3}{12(1-\nu^2)}, \quad D_y = EI, \quad H = \frac{s}{L} \frac{Et^3}{12(1+\nu)}, \quad (3.11)$$

in which  $s$  and  $I$  are the arc length and the inertia of moment,  $s = L(1 + \frac{\pi^2 f^2}{4L^2})$  and

$$I = \frac{f^2 t}{2} \left(1 - \frac{0.81}{1 + 2.5(\frac{f}{2L})^2}\right), \text{ respectively.}$$

Lau (1981) proposed an analytical model to get a more precise approximation about the bending stiffnesses. In his paper, the relative parameters are defined as:

$$s = \frac{2L}{\pi} \sqrt{1 + \alpha^2} E(k, \frac{\pi}{2}) \quad (3.12)$$

in which  $\alpha = \frac{f\pi}{L}$  ;  $\beta = \frac{\pi x}{L}$  ;  $E(k, \frac{\pi}{2}) = \int_0^{\pi/2} \sqrt{1 - k^2 \sin^2 \beta} d\beta$  ; and

$$k^2 = \frac{\alpha^2}{1 + \alpha^2} < 1 \text{ for all the real value of } \alpha .$$

The moment of inertia is:

$$I = \frac{2tf^2}{3\pi} \frac{\sqrt{1 + \alpha^2}}{k^2} [(2k^2 - 1)E(k, \frac{\pi}{2}) + (1 - k^2)F(k, \frac{\pi}{2})], \quad (3.13)$$

in which  $F(k, \frac{\pi}{2}) = \int_0^{\pi/2} d\beta / \sqrt{1 - k^2 \sin^2 \beta}$ .

---

For a thin plate ( $t/L=0.04$ ) with the high corrugation ratio, the transverse stiffness is nearly four orders of magnitude smaller than a similar flat plate. The loss of transverse extensional stiffness is directly attributed to the dominant bending deformation in the structure; as the corrugation ratio increases, the bending deformation is more significant, and the transverse stiffness decreases dramatically.

In our studies, the high bending stiffness is required for a good performance of the plate-type wave reflector. With the consideration of the high bending stiffness, a sandwich plate with a corrugated core can be adopted. Corrugated core materials include a large variety of geometries, often providing a highly directional core stiffness for certain applications. Ordinary cardboard is a common example of corrugated core sandwich. Stiffened panels, as well as web core and truss, can be considered as corrugated core structures.

With the same mechanism of the corrugated plate, the bending stiffness of the sandwich plate is generally much larger transverse to the corrugations ( $x$ -direction) than along the cross-direction of each of the constituents ( $y$ -direction), while the reverse is true for the out-of-plane shear stiffnesses. This means that the direction of the large bending stiffness ( $x$ -direction) coincides with the direction of low transverse shear stiffness. When the corrugated core is attached with two

---

facesheets, its bending stiffness will be greatly increased, and satisfy our requirement.

## **Chapter 4: Choice of plate material & structure**

### ***4.1 Introduction***

In Chapters 2 and 3, both two-dimensional model and three-dimensional model are simulated. In this chapter, experiments for both the two-dimensional model and the three-dimensional model are conducted to verify the theoretical findings. Methodology and results of the experiment are described.

For the two-dimensional model, a material with low mass ratio but high bending stiffness is preferred. However, for the three-dimensional model, its optimal bending stiffness is much lower, but it also requires the mass ratio of the plate to be as low as possible. Through the parametric studies about the effects of both the mass ratio and the bending stiffness on the silencer bandwidth, the low mass ratio is found to be the premier factor which influences the performance of the plate-type wave reflector. This is so because the acoustic energy is very small, and if the chosen material is heavy, it won't be excited by the sound waves. Moreover, according to the different requirements of the bending stiffness in both the 2D model and the 3D model, a moderate bending stiffness, not too high or too low, is

---

avored. Under the consideration of all the requirements, a 3mm-thick foam plate with the density  $\rho^* = 63.2 \text{ kg/m}^3$  is selected for both the two-dimensional experiment and the three-dimensional experiment in the present studies.

## **4.2 Determination of material properties**

In our experiment, two methods, the static method and dynamic method, are used to determine the Young's modulus of the plate material, which are described as follows.

### **4.2.1 Static method**

The static method makes use of the three-point bending mechanism. Specimen with the size of 25 mm wide by 160mm long by 5mm thick is used. Although the thickness of the foam is different from that of the foam used in the experiment, all the other properties are the same for them. The configuration of the installation is shown in Figure 4.1.

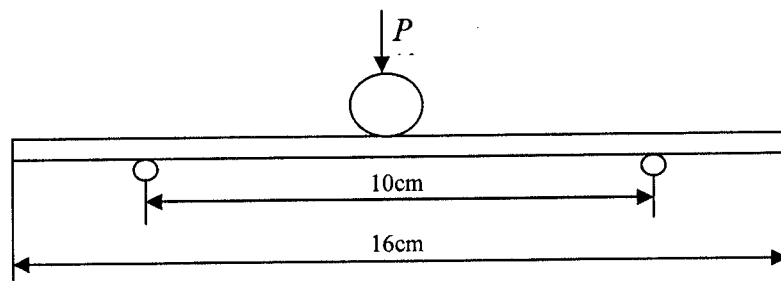


Figure 4.1: The configuration of the experimental setup

In this experiment, the equipment ‘*Axial Static Testing Machine*’, with a maximum loading  $50\text{ kN}$ , is used to obtain a relationship between the applied loading and the extension of the specimen. The machine has a master template for compression testing. From this template, methods can be constructed to conform with ASTM D695. First, the crosshead will move to contact the specimen and generate a load specified by the Pre-load input. Then, the crosshead will move at the test speed until it reaches a strain corresponding to the strain endpoint input.

Figure 4.2 shows the curve of the extension of the plate with the increasing applied load  $P$ . Because the speed of the crosshead is defined very low  $v=1.27\text{ mm/min}$ , the

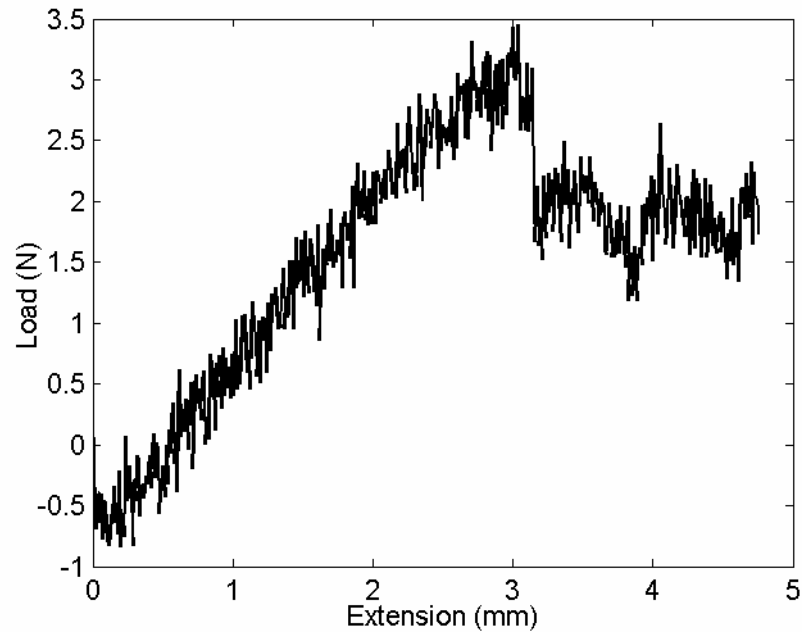


Figure 4.2: Relationship between the applied loading and extension

curve looks coarse, instead of a smooth one. The final result of the testing shows the Young's modulus of the specimen is  $E=42.680\text{MPa}$ .

#### **4.2.2 Dynamic method**

The dynamic method is actually a combination of both experimental and numerical work. In this method, the natural frequencies of the plate material are firstly determined by experiment, and then the numerical simulation is conducted to find the particular Young's modulus of the plate material using the known natural frequencies and the density.

In the experiment, a uniform foam plate with a length 520mm, width 114mm and thickness 3mm is installed covering a square-shaped hole of the duct with two clamped ends and two free ends. One surface of the plate faces the duct, and the other surface faces the air outside. Therefore, the dynamics of the plate is determined by the combination of both the pressure of the duct  $p_d$  and the outside air pressure  $p_0$ . The effective area of the plate, which does not include the clamped part, is 497mm long by 114mm wide. The sketches of the setup and the specimen are shown in Figure 4.3. Figure 4.3 (a) shows that a foam plate is under the excitation of the sound from the loudspeaker, which is a white noise generated by function generator (Hioki). The frequency range specified is 0-100Hz. Laser vibrometer (Polytec type with controller FV-3001 and sensor head OFV-303) is used here to get the signal, vibration velocity here, of the plate. Figure 4.3(b) shows

---

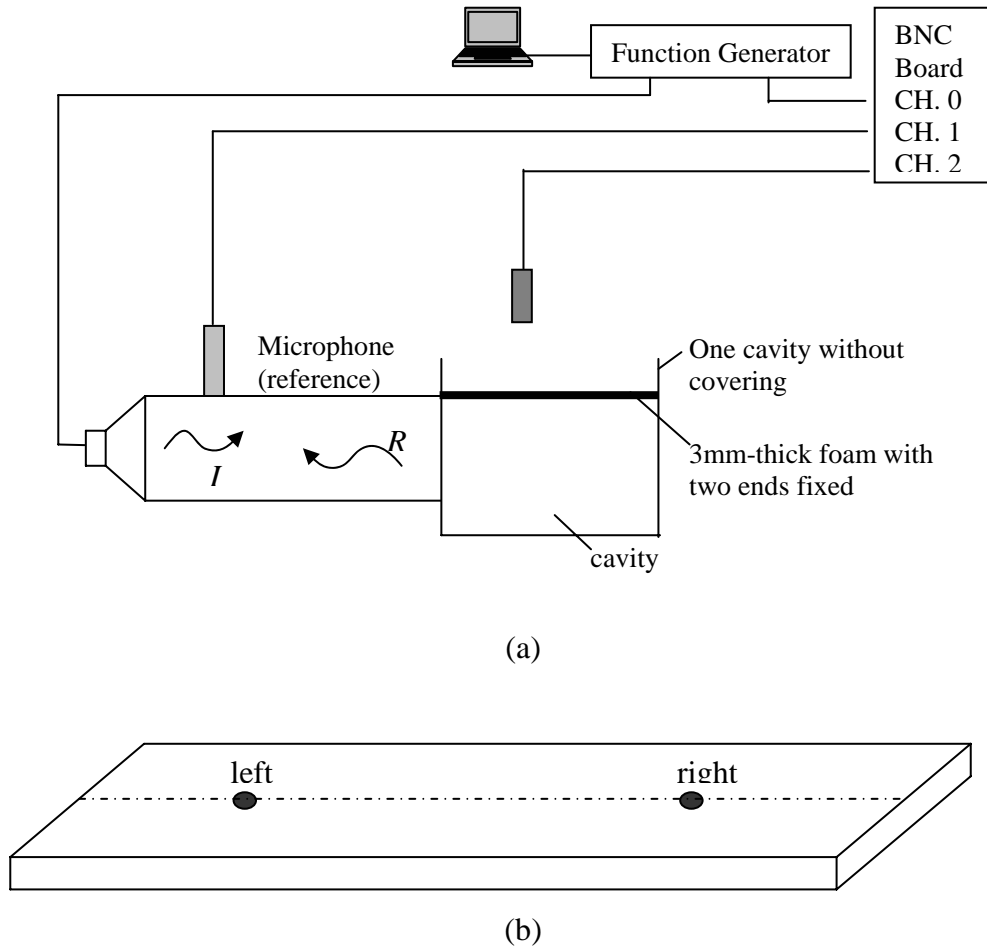


Figure 4.3: (a): Experiment setup of the vibration testing using laser vibrometer, and (b) is the configuration of the 3mm-thick foam with two testing points

the configuration of the foam plate with two testing points. The vibration velocities at these two points along the middle longitudinal line of the plate are measured. The signals collected by a B&K's 1/2 inch condenser microphone (Type 4187) are used as the reference signal here. The data collected by the laser vibrometer within

---

the frequency range 0-100Hz are the response. The reason why a loudspeaker is used to excite the plates to get the natural frequencies of the plate is that, it is more analogous to the environment of our later experiment to find the overall transmission loss spectrum. Then the natural frequencies of the specimens can be determined by frequency response function. Figure 4.4 shows the testing results,

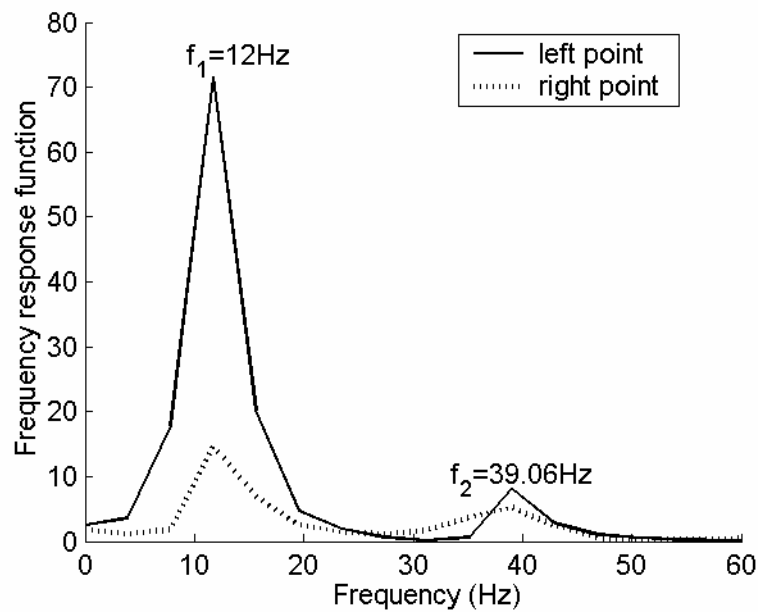


Figure 4.4: Natural frequencies of the 3mm-thick foam with two fixed ends

for the frequency response function of the two different points. The first two natural frequencies of the plate can be identified from Figure 4.4 as:  $f_1 = 12Hz$  and  $f_2 = 39.06Hz$ .

With the known natural frequencies, together with the density, of the 3mm-thick foam, a simulation in FEMLAB is conducted to determine its Young's modulus. In the simulation, the 'eigenfrequency analysis' solver in 'Mindlin Plate' of the 'structural mechanics module' is chosen. With the specified geometry, the Young's modulus  $E$  can be determined by changing the input values of the Young's modulus and comparing the resulting natural frequencies with the experimental results until they match each other. Figure 4.5 shows the first two *in vacuo* modes of the 3mm-thick foam plate when  $E = 54.4MPa$ . Compare the simulation results

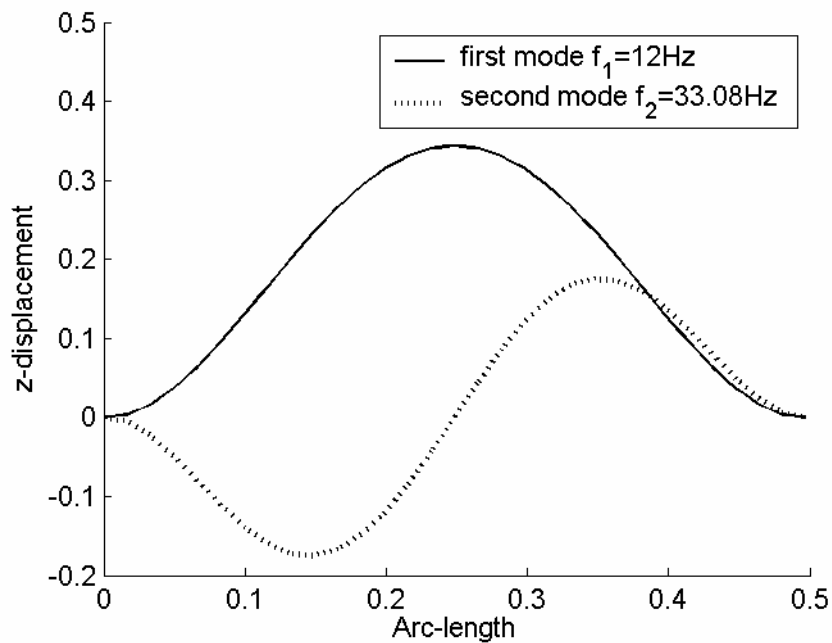


Figure 4.5: The first two *in vacuo* modes of the 3mm-thick foam plate when  $E = 54.4MPa$

and the experimental results got from the laser testing shown in Figure 4.5, it is found that, when the first natural frequency matches, the second natural frequency will be a little lower than the experimental result. This is so because the simulation results are the *in vacuo* natural frequencies, and no effect of the air is considered. However, the experiment measures the natural frequencies of the plate in the coupled system of both the set-up and the surrounding air, and the effect of the air makes the second natural frequency smaller than the second *in vacuo* one.

Compare the results of the two results of both the static method and the dynamic method, it is found that the results don't match very well. This is because in the simulation of the dynamic method to determine  $E$ , the frequencies are used as the *in vacuo* natural frequencies, and no air effect is involved in it. However, because the experiment cannot be operated *in vacuo*, there is a coupling between the plate and the air. Therefore, the measured natural frequencies are actually the results in the coupled system, and are essentially different from the ones used in the simulation. These discrepancies result in the different results in the two methods.

### **4.3 Acoustic measurement**

In our experiment, two-microphone method is used to resolve the standing wave pattern in both upstream and downstream regions. The signal can be either harmonic or random. But the inherent requirement of the two-microphone method

---

is that the amplitude and phase mismatch of the two microphones should be calibrated. What's more, the microphone holders may also have influence on the measured signals. A calibration for the four microphones is needed before all the procedures of the experiment. In our experiment, the ISO 10534-2:1998 is followed in the calibration exercise.

The two-load measurement method (Munjal and Doige, 1990) is used to find the transmission loss in the experiment, and its setup is shown in Figure 4.6

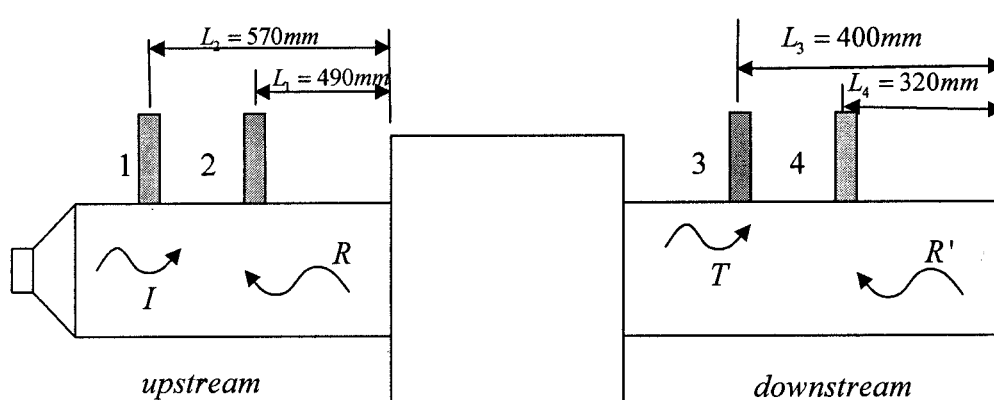


Figure 4.6: The set-up for the standing wave decomposition and the two-load method

In Figure 4.6, there are four traveling waves at the upstream and downstream of the chamber. At the upstream duct,  $I$ ,  $R$  are the incident and reflected wave respectively, and at the downstream duct,  $T$  and  $R'$  are the transmitted and the second reflected waves respectively. All the four waves are considered to be plane

waves at a distance sufficiently far away from the junctions. Four microphones are installed flush with the duct to collect data of the sound pressure.

Filtering or windowing is usually used in the spectral analysis of data. This is because when a pure tone is sampled for over a non-integer number of cycles, spectral leakage will appear. The spectral leakage often causes the energy of one given frequency to be distributed to adjacent discrete frequencies, and makes the measurement results inaccurate. Many corrections are used to reduce the influence of the spectral leakage, including data windowing. However, although the windowing can reduce the leakage, it may also cause the phase angle distortion. Under this situation, the sampling rate should be adjusted with the frequency of the noise sources changing. Therefore, a Labview program is written in our experiment to generate the signal from the loudspeaker, and collect data with an adjustable sampling rate such that integer number of noise signals are obtained each time. The program firstly generated digital DA signal and trigger the DA system, about 1 second after the DA level is set, the data acquisition process starts to collect the data of the frequencies from 10Hz to 680Hz. The operation of FFT does not need data windowing in our experiment due to the sampling rate adjustment.

In the experiment, two sets of frequency loops are used. In the first loop, an initial voltage  $V_i$  is pre-defined to the loudspeaker, and this is a trial loop to get the relationship between the DA amplitude and received AD voltage amplitude. Then,

---

the optimal DA voltage  $V_o$  over the whole frequency range can be determined by the desired uniform AD voltage. Therefore, the second frequency loop can use the optimal voltage  $V_o$  to get a higher signal-to-noise level of the microphones.

Before testing the transmission loss curve of the plate-type wave reflector with two clamped ends and two free ends, a calibration for the whole experiment setup is needed to find whether there are any problems with the testing rig. To calibrate the experiment setup, nothing is used to cover the cavity, which means an expansion chamber is tested. The expansion chamber is 500mm long, and has an area ratio of  $a = 3$ . The size of the straight duct has a cross section of  $100\text{mm} \times 100\text{mm}$ . Both of the duct and the cavity is made of 10mm thick acrylic, which can be regarded as acoustically hard. The configuration of the whole experiment setup is illustrated in Figure 4.7:

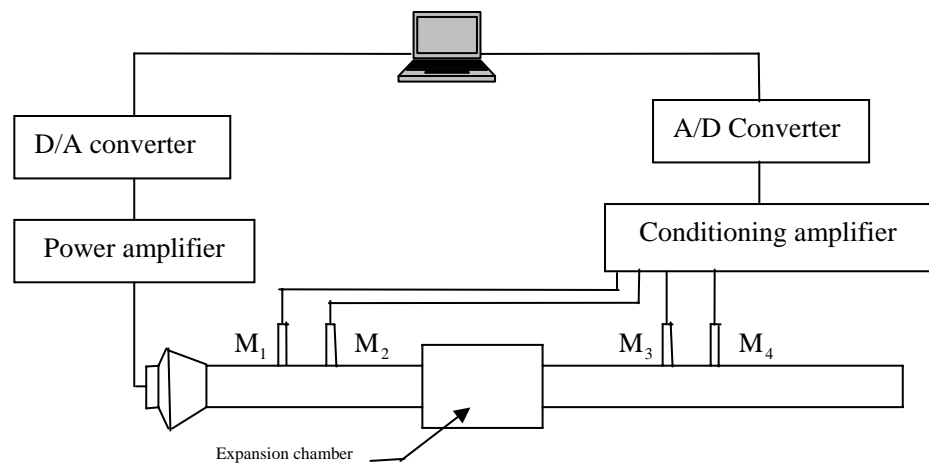


Figure 4.7: The set-up of the experiment

In the experiment, a Labview program is run by the computer to generate a series of pure tone signal, whose frequency range is from 10Hz to 1000Hz with an interval of 10Hz. To use the pure tone signal is because it has a better signal-to-noise ratio, and it's important to the low-frequency noise. The digital signals pass the D/A converter (type PCI-M10-16E-1) to convert into the analog signals. The signals are amplified by B&K's power amplifier (type LAB Gruppen 300). The loudspeaker generates a series of pure tone signals from 10Hz to 1000Hz. The signals of sound pressure inside the duct are collected by the four B&K's 1/2 inch condenser-type, intensity microphones (type 4187), which are fixed flush with the duct, and the output signals are connected with B&K's Nexus four-channel conditioning amplifier (type 2693). The signals are then transferred to the A/D converter (type BNC 2140) installed in the computer.

The two-load measurement method is adopted in the experiment, and the positions of the four microphones are the same as what are specified in Figure 4.6. To compare the experimental result with theoretical model, a finite element simulation is made in FEMLAB, and the comparisons are displayed in Figure 4.8. It is found that the transmission loss at the three peaks increases with the excitation frequency. According to the plane wave theory, the  $TL$  at every peak should be equal. This is because with the frequency increasing, higher order modes are excited when the frequency exceeds the cut-on frequency of the chamber, when the plane wave

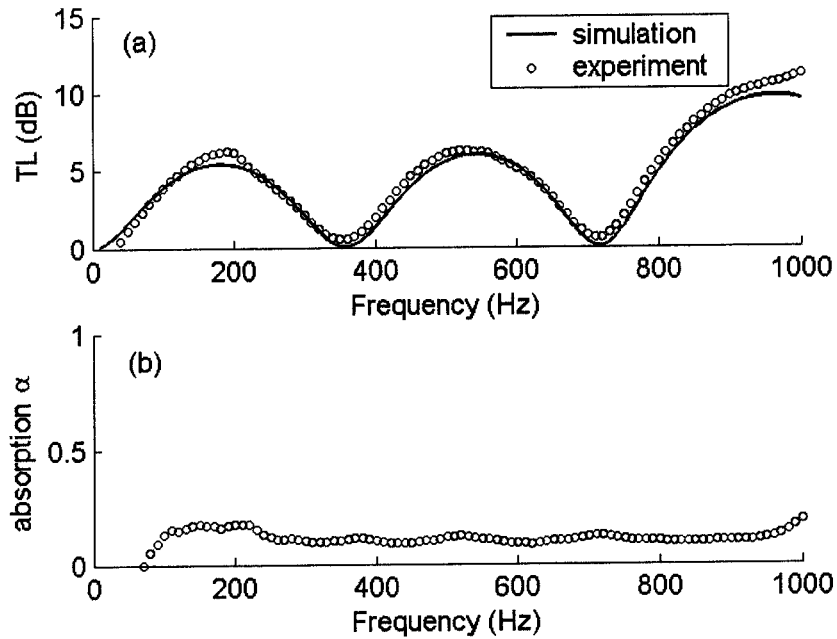


Figure 4.8: A comparison about the TL curve between the simulation result and the experiment result (a), and the measured absorption coefficient of the expansion chamber (b)

theory breaks down. But the FEMLAB® shows the trend, which has a coincidence with the experimental results. However, the  $TL$  of the experimental result is greater than the simulation result. This is because there is unavoidably leakage or friction in the test rig. All the dissipated energy will cause the increase of the  $TL$  of the experimental results.

The spectrum of the absorption coefficient in Figure 4.8(b) is around 0.1, and this is believed to be caused by the energy dissipation. To improve the performance of the expansion chamber, gaps should be prevented in the whole setup, which may

result in leakage to the air outside the setup especially for the high-frequency range. Besides, the system should also be guaranteed with no vibration. Therefore, the rubber strips are used to prevent the leakage and holders are used to prevent vibration.

## **4.4 Experimental results**

### **4.4.1 Two-dimensional model**

In the two-dimensional model, the two lateral edges are free to vibrate. The gap between the actual test-rig and the plate edges is about a piece of paper wide. The other two longitudinal edges are clamped using two acrylic rods with specified sizes. With the measurement methodology and data requisition system described in the former sections, the transmission loss spectrum of the two-dimensional model is obtained. Two coefficients, absorption coefficient  $\alpha$  and relative reflection coefficient  $\beta/(1-\alpha)$ , are also measured to make a further description about the mechanism of the two-dimensional plate-type wave reflector in noise reduction.

Because of the viscosity of the acoustic boundary layer on the duct walls and cavity walls, energy dissipation always happens. To quantify the energy loss caused by viscosity, absorption coefficient  $\alpha$  is adopted here with the definition:

$$\alpha = \frac{|I|^2 - |R|^2 - |T|^2}{|I|^2}, \quad (4.1)$$

where  $I$ ,  $R$  and  $T$  are the amplitudes of the incident, reflected and transmitted waves respectively. The relative reflection coefficient,  $\beta/(1-\alpha)$ , where  $\beta = \frac{|R|^2}{|I|^2}$ , is defined here to examine to what extent the plate-type wave reflector reflects waves which are not absorbed,  $1-\alpha$ .

The experimental results of the two-dimensional model are shown as open circles in Figure 4.9, and simulation results are also needed here to make a comparison with the experimental results. In Section 4.2, two different methods are described to determine the Young's modulus of plate. However, due to the instability of the static method and the essential flaw of the dynamic method, the actual Young's modulus still needs to be determined. With the positions of the peaks in the experimental results,  $D=0.0006$  is determined, and the results are in Figure 4.9 as the solid line. Figure 4.9 (a) shows a comparison between the simulation result and experimental result of the two-dimensional model. It can be found that the performance of the plate is not good, and this is because the bending stiffness of the plate material is not the optimal value. There are two groups of peaks in the low-frequency region as shown in the spectrum of simulation result, the solid line. Each group has two peaks in the stopband located at  $f_{p1s} = 0.0204$ ,  $f_{p2s} = 0.0302$  and  $f_{p3s} = 0.048$ ,  $f_{p4s} = 0.064$ , respectively. While, in the spectrum of experimental result, two groups of peaks, which are also composed of two peaks each, appear at the frequencies  $f_{p1e} = 0.021$ ,  $f_{p2e} = 0.030$  and  $f_{p3e} = 0.042$ ,

---

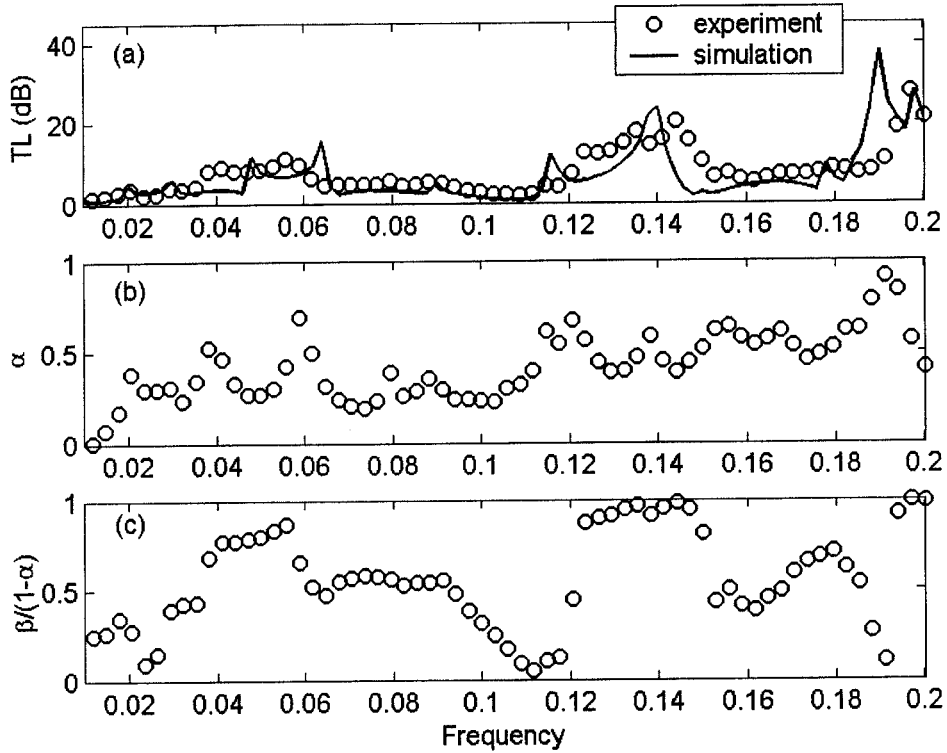


Figure 4.9: Comparisons between the simulation result and experimental result of two-dimensional model using 3mm-thick uniform foam plate. The open circles are the measured data, and the solid line is the simulation result

$f_{p4e} = 0.056$ . From the two results, it can be found that the positions of the third and fourth peaks shift a little with each other. These shifts are mainly due to the problems in the implementation of two clamped lateral edges and the two free longitudinal edges. As described in the section 3.1, it is difficult to control the gap size between the two free longitudinal edges and the duct, and the gap has much influence on the final performance. Even only one point of the plate touches the

duct or cavity, the freedom of the plate vibration will be greatly reduced, and finally greatly influences the measured results. Besides, the clamped boundary condition cannot be ideally realized in the experiment, either. The differences between the ideal definition in simulation and the practical implementation in experiment are the main sources, from which the shifts come. What's more, many other factors may also have influence on the result, such as the small discrepancies between the actual properties of the plate and the defined values in simulation and so on.

In Figures 4.9(b) and 4.9(c), the spectra of the absorption coefficient  $\alpha$  and the relative reflection coefficient  $\beta/(1-\alpha)$  are displayed for an easy comprehension of the mechanism of the plate-type wave reflector. In Figure 4.9(b), a comparatively high absorption coefficient is displayed. The high absorption is mainly caused by the leaking. As explained above, the gap size is difficult to handle. Moreover, the property of the plate material is also a factor which may lead to a high absorption. Actually, damping is a complicated topic, and is not included in the present studies. In Figure 4.9(c), the experiment data shows that in the region where the peaks locate, the relative reflection coefficient  $\beta/(1-\alpha)$  is much higher than the absorption coefficient  $\alpha$ . It shows that the reflection mechanism is the dominant mechanism within this region, rather than the absorption mechanism, and it agrees well with the theory.

To further validate the two-dimensional model, a vibration testing, using laser vibrometer (Polytec type with controller FV-3001 and sensor head OFV-303), is conducted to explore the vibration situations of the plate at the frequencies of the first two peaks. The vibration situations of the plate can be determined by picking up the signals through the transparent cavity wall by the laser vibrometer. The experimental set-up is described in Figure 4.10. The digital signals from the

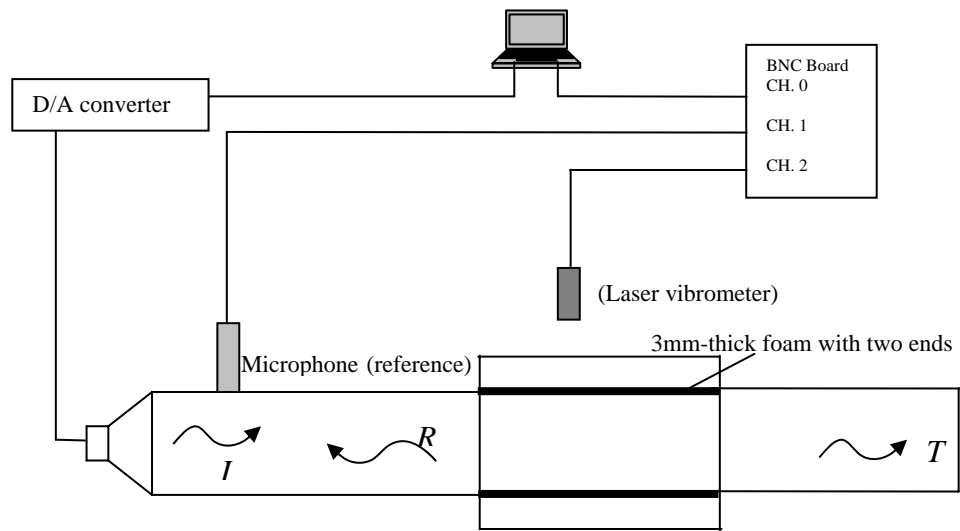


Figure 4.10: Experiment setup of the vibration testing using laser vibrometer

computer are converted into the analog signals by the D/A converter (type PCI-M10-16E-1), and then make the loudspeaker generate a series of pure tone signals from 10Hz to 1000Hz. The signals collected by a B&K's 1/2 inch condenser microphone (Type 4187) are still used as the reference. To use the pure tone signals is because it is convenient to focus the frequencies of the incident

waves to our desired values. Here, the first and second peaks, whose corresponding frequencies are  $f_{p1e} = 0.021$  ,  $f_{p2e} = 0.030$  for the experiment, and  $f_{p1s} = 0.0204$  ,  $f_{p2s} = 0.0302$  for simulation are focused.

In this experiment, 26 points of the plate, which are separated with each other by the equal space along the longitudinal direction, are tested. The signals at each point are collected by moving the sensor to each point and repeating the same procedures of collecting data. Figure 4.11 shows the vibration responses of the plate at the first two peak frequencies. It can be found that the vibration modes of the plate resemble the distorted fourth and fifth modes, not the distorted second

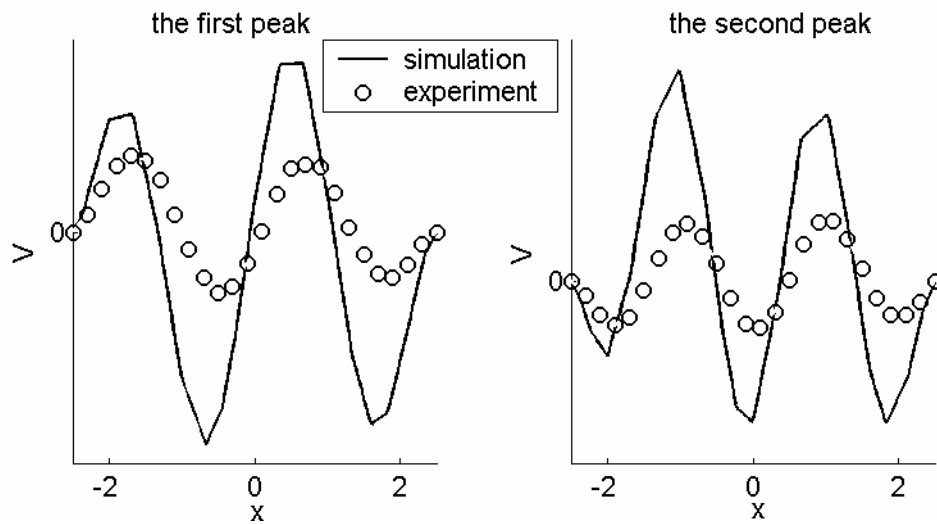


Figure 4.11: The response of the plate along the longitudinal direction. The left column is the response at the first peak frequency, and the right column is the response at the second peak frequency.

and third modes shown in the preceding modal analysis for the optimal situation of the two-dimensional model at the first and second peaks. Just because the vibrations of the plate in this experiment are dominated by higher order modes than those of the optimal situation, the performance of the 3mm-thick foam is not as satisfactory as that of the optimal one. However, the comparisons between the simulation predictions and the experimental results show a good agreement.

The vibration measurement along the lateral directions is also conducted at the frequencies of the first two peaks. Five points along a lateral line are measured, and the experimental results are shown in Figure 4.12 for the vibration along the lateral

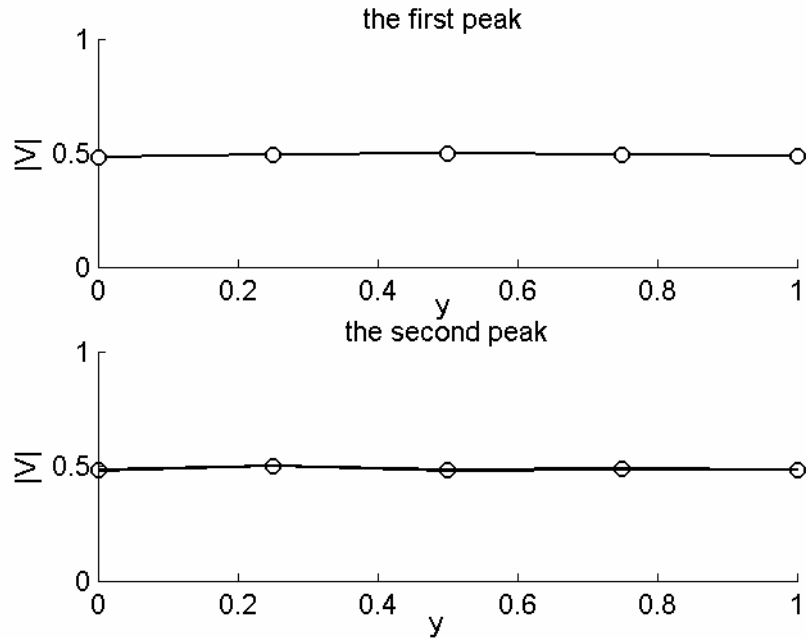


Figure 4. 12: The response of the plate along the lateral direction. The first row is the response at the first peak frequency, and the second row is the response at the second peak frequency

---

direction at the first two peaks. In the two-dimensional model, the two lateral edges of the plate are without any restrictions, and hence there should not be any vibrations along the lateral direction. From the subfigures, it can be found that the amplitudes of the velocity are almost zero, which is coincident with the theoretical predictions. In conclusion, the results of the vibration measurement along both the longitudinal direction and the lateral direction have a good agreement with the theoretical results, and hence further prove the two-dimensional model is correct.

#### **4.4.2 Three-dimensional model**

In the three-dimensional experiment, all the four edges of the plate are fixed by four acrylic rods with specific dimensions. The same experiment methodology as that of the two-dimensional experiment is adopted, and the final results are shown in Figure 4.13. Figure 4.13(a) displays a comparison of the transmission loss spectra between the simulation result (solid line) and the experimental result (open circles). The bending stiffness used in the simulation is the same as that of the two-dimensional model,  $D=0.0006$ . In both results, two peaks appear within the stopband, and the two results agree with each other very well,  $f_{p1s} = f_{p1e} = 0.042$  and  $f_{p2s} = f_{p2e} = 0.056$ . Also can be seen in Figure 4.13(a), peaks in the mid-frequency have some shifts between the two results. This is because the clamped boundary condition for the four edges cannot be perfectly implemented

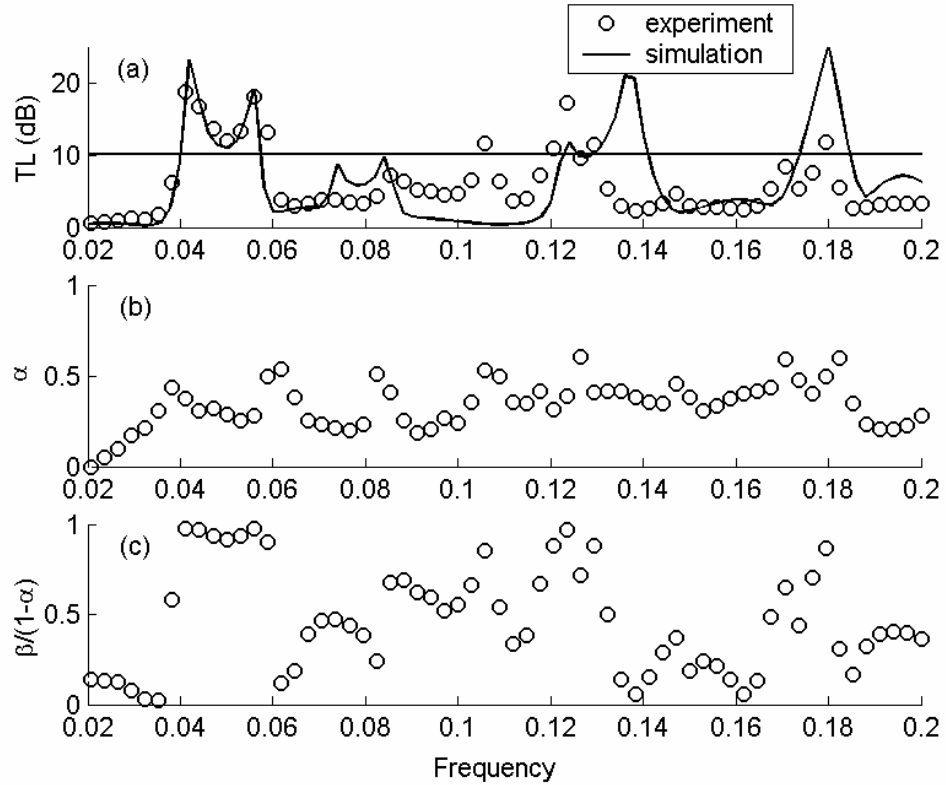


Figure 4.13: Comparisons between the simulation result and experimental result of three-dimensional model using 3mm-thick uniform foam plate. The open circles are the measured data, and the solid line is the simulation result

in experiment, especially at the two longitudinal edges, which finally affects the results. Besides, the influences of the experiment set-up cannot be neglected, either. Figures 4.13(b) and 4.13(c) show the spectra of absorption coefficient  $\alpha$  and the relative reflection coefficient  $\beta/(1-\alpha)$ . It's obvious to find that in the region where the peaks locate, the relative reflection coefficient is very high, and reaches nearly equal to 1, demonstrating the domination of the reflection mechanism.

Comparing the relative reflection coefficient  $\beta/(1-\alpha)$  in both the 2D model and 3D model, it is found that the values at the peaks in 3D model are even higher than those in the 2D model, which can also be perceived from the peak amplitudes in the two models. In the 3D model, there are two peaks above the criterion level 10 dB in the low-frequency region, better than the performance of the 2D model, and the peaks essentially depend on the reflection capability of the plate, and hence can be seen as an embodiment of the relative reflection coefficient.

The vibration measurement along the longitudinal direction and the lateral direction of the plate is also conducted for the three-dimensional experiment. The vibration velocities of 21 points along the longitudinal direction have been measured, and the results are shown in Figure 4.14.

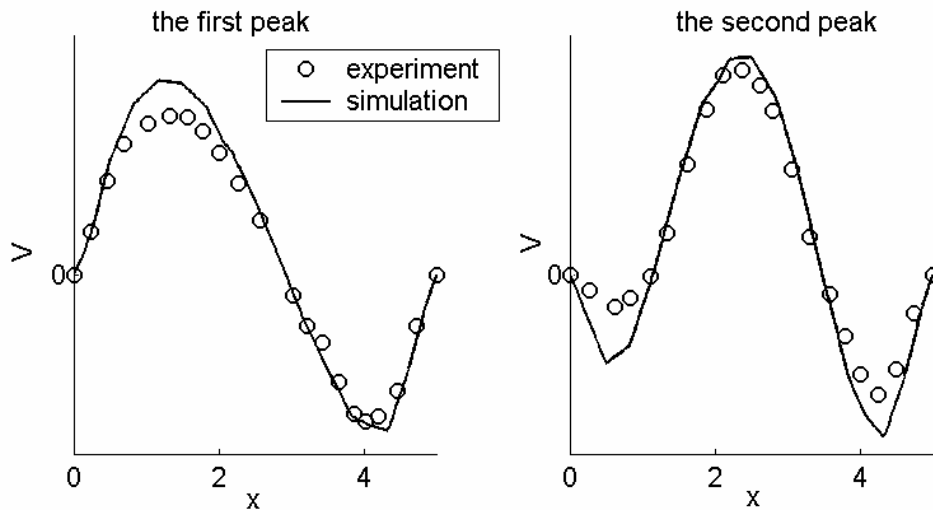


Figure 4.14: The response of the plate along the longitudinal direction. The first column is the response at the first peak frequency, and the second column at the second peak frequency.

The subfigures in both of the columns in Figure 4.14 show a good agreement between the simulation result and the experimental result, and show the vibration mode of the plate resembles a distorted second mode at the first peak frequency, and the distorted third mode at the second peak frequency.

Different from the two-dimensional model, the lateral edges of the plate in the three-dimensional model are both fixed. Such a boundary condition will also lead to a vibration along the lateral direction. Totally five points along the lateral direction have been measured, and Figure 4.15 shows a comparison between the simulation result and the experiment result. It can be found that the lateral vibration

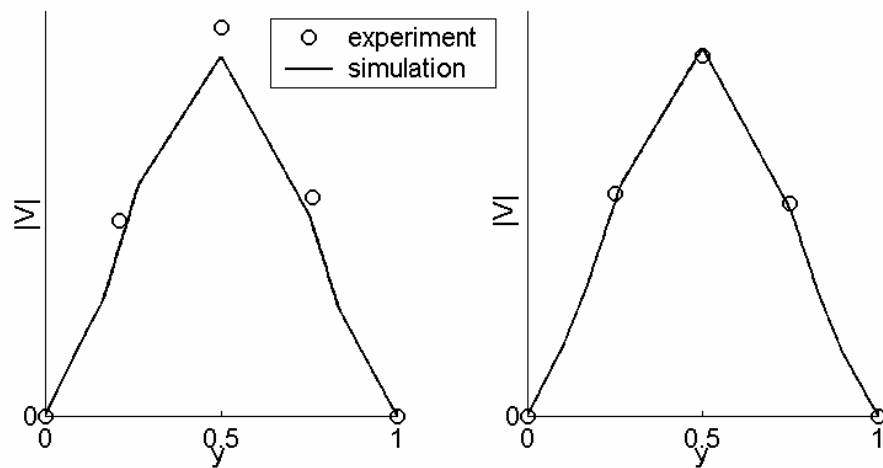


Figure 4.15: The response of the plate along the longitudinal direction. The left column is the response at the first peak frequency, and the right column for the second peak frequency.

of the plate shows the first mode in both the simulation result and the measured result, and proves the theoretical three-dimensional model is correct.

## **4.5 Results for honeycomb structure**

### **4.5.1 Choice of plate material/structure**

For the two-dimensional model, the parametric studies of the two-dimensional simulation show that, both low mass ratio and high bending stiffness is preferred for the plate-type wave reflector. The desired range for the mass ratio is from 1 to 10, and for the dimensionless bending stiffness from 0.1 to 1. Normally, it is difficult to find a homogeneous material satisfying both of the requirements at the same time, therefore, composite structures are focused in our studies.

Sandwich structure is well-known for its high bending stiffness, and has been widely used in many places where the high bending stiffness is required. Its structural efficiency relies heavily on the lightweight cores that separate the face sheets and provide the necessary stiffness. A variety of core configurations have been proposed, in which honeycomb sandwich structures is just one of them.

Honeycomb sandwich structure is a multi-layered structure consisting of one or more high-strength, stiff layers (e.g., laminated facings) bonded to one or more flexible layers. It possesses a very high stiffness to weight ratio, and is used in a

---

wide variety of structural applications, such as the aerofoil, the vanes of the generator, sports productions and so on, largely because of their relative advantages over other structural materials in terms of improved stability, weight savings, and ease of manufacture and repair. Honeycomb cores can be manufactured from a wide range of materials such as aluminum, titanium, fiber reinforced plastics or even resin impregnated paper.

For the aluminum honeycomb structure, it has the largest stiffness-mass ratio in all of the structures. However, under the consideration of mass ratio, it's still too heavy to have a good performance. Take the aluminum honeycomb panel of 5mm for example: its area density is around  $4.9 \text{ kg} / \text{m}^2$ , and hence its mass ratio is

$$m = \frac{\rho^* h^*}{\rho_0 h_0} = \frac{4.9}{1.225 * 0.1} = 40$$

which is beyond the desired region. Therefore, the aluminum honeycomb structure is not a good choice for the experiment.

Besides the aluminum honeycomb cores, the composite honeycomb cores also have a wide application in industries, where weight is much concerned. The Nomex honeycomb core, whose density is very small, is one of the most popular types, although its bending stiffness is not as good as the aluminum honeycomb structure with the same thickness.

Normally, the density of the Nomex cores is between  $24 \text{ kg/m}^3$  and  $144 \text{ kg/m}^3$ , and the thickness is above 5mm. Under the consideration of the low mass ratio requirement, a 5mm-thick Nomex honeycomb core, with the density  $29 \text{ kg/m}^3$ , is selected, and 0.025mm-thick aluminum membrane is used as the face-sheets.

For the adhesive, it should be suitable for forming bonds that can withstand long combinations of stress, temperature and relative humidity expected to be encountered in service. Besides, it should be used for bonding core segments and for bonding core segments to edge members and to integral members in a honeycomb sandwich panel. And it should not allow the transfer of water from one part of the panel to another either through or along the line of the adhesive. According to these requirements, epoxy resin is chosen here to glue the Nomex cores and the aluminum membranes together. The completed honeycomb structure has the density of  $106 \text{ kg/m}^3$ , and its mass ratio is derived as below:

$$m = \frac{\rho^* h^*}{\rho_0 h_0} = \frac{106 \times 5 \times 10^{-3}}{1.225 \times 0.1} = 4.3,$$

which is within the desired range.

In order to find whether the bending stiffness of the Nomex honeycomb structure can satisfy the requirement of our experiment, the static bending stiffness testing method is used here for quantification.

Two specimens are made for the test. Both of the specimens are 25 mm wide by 160mm long. One of them is 10mm thick with the core density  $48\text{ kg/m}^3$ ; while, the other is 5mm thick with the core density  $29\text{ kg/m}^3$ . The upper and lower face sheets are both the 0.025mm-thick aluminum membrane. The honeycomb cores and the face sheets are glued together by epoxy resin.

The mechanism of the bending stiffness testing has been described above, and the result of the specimen of 5mm thick is shown in Figure 4. 16:

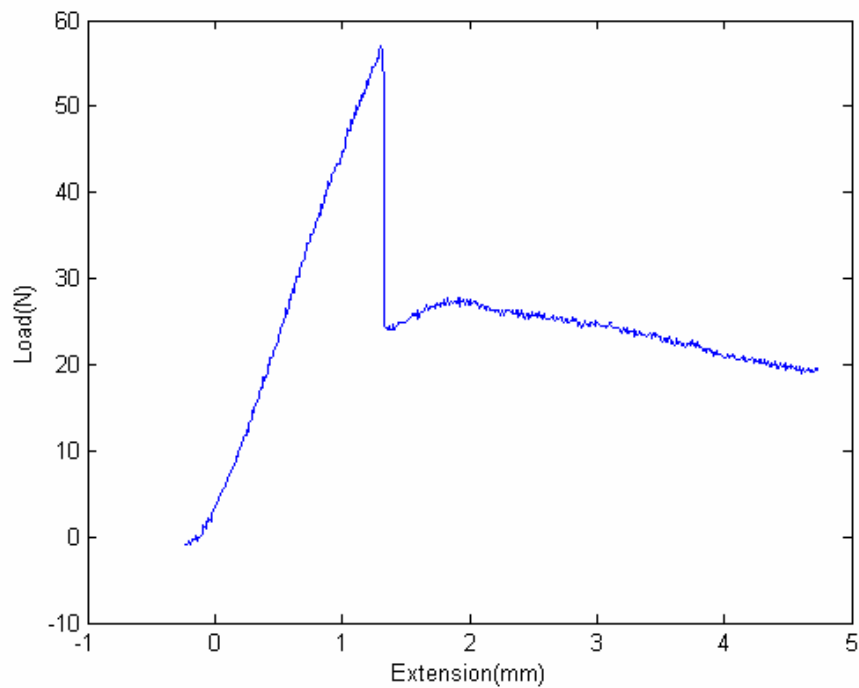


Figure 4.16: The load-extension Curve of Nomex honeycomb structure of 5mm thick

The result of the specimen of 10mm thick is shown Figure 4.17. For a

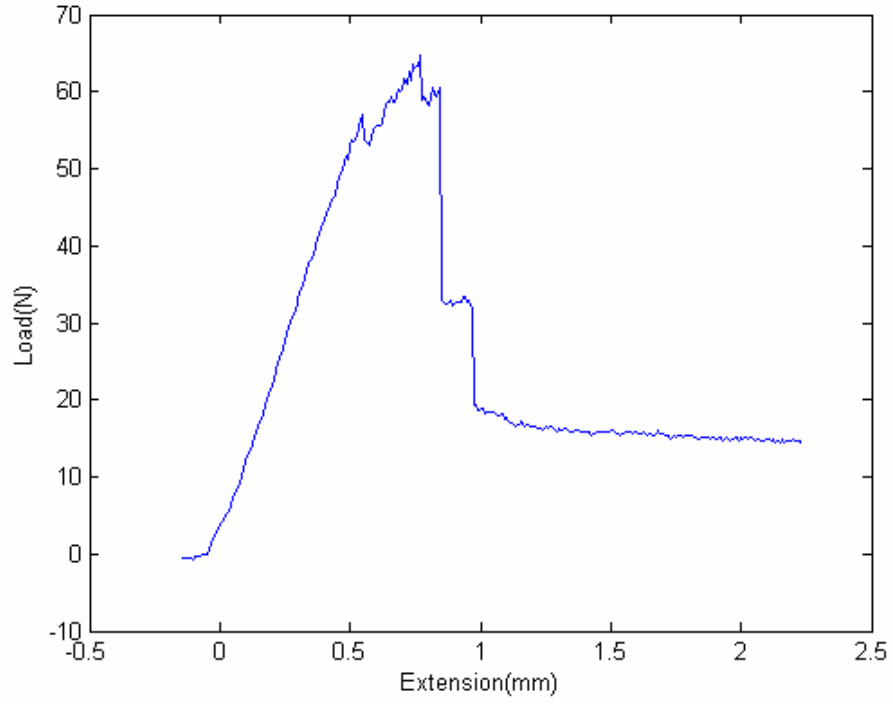


Figure 4.17: Load-extension Curve of Nomex honeycomb structure of 10mm thick

simply-supported beam, whose length is  $L$ , its extension under a load  $F$  can be expressed as:

$$y = -\frac{Fx}{12EI} \left( \frac{3}{4}L^2 - x^2 \right) \quad (0 \leq x \leq L/2) \quad (4.2)$$

and the maximum extension, which locates the middle point of the beam, is

$$y_{\max} = \frac{FL^3}{48EI}.$$

In the experiment, the length of the beam between the two supporting edges is  $L=100\text{mm}$ . The bending stiffness  $D$  from the specimens can also be written as

$$D = EI = \frac{FL^3}{48y} = 2.1 \times 10^{-5} k, \text{ in which } k \text{ is the oblique ratio of the line before}$$

failure point.

For the 5mm-thick honeycomb structure, two points, (20.02N, 0.4199mm) and (30.18N, 0.6445mm), are used for interpolation to get the oblique ratio:

$$k = \frac{30.18 - 20.02}{(0.6445 - 0.41955) \times 10^{-3}} = 4.52 \times 10^4 (N/m)$$

And the bending stiffness can be derived through

$$D = EI = \frac{FL^3}{48y} = 2.1 \times 10^{-5} k = 2.1 \times 10^{-5} \times 4.52 \times 10^4 = 0.949 (Nm^2)$$

For the 10mm-thick honeycomb structure, two points, (30.12N, 0.27415mm) and (40.04N, 0.36658mm), are used to get the oblique ratio:

$$k = \frac{40.04 - 30.12}{(0.36658 - 0.27415) \times 10^{-3}} = 1.0732 \times 10^5 (N/m)$$

and the dimensional bending stiffness is derived

$$D = EI = \frac{FL^3}{48y} = 2.1 \times 10^{-5} k = 2.1 \times 10^{-5} \times 1.0732 \times 10^5 = 2.25 (Nm^2)$$

The normalization formula is used here to get the dimensionless bending stiffness

---

$$\text{5mm-thick: } D = \frac{D^*}{D_0} = \frac{D^*}{\rho_0 c_0^2 w h^3} = \frac{0.949}{1.225 \times 340^2 \times 0.025 \times (0.1)^3} = 0.268,$$

$$\text{10mm-thick: } D = \frac{D^*}{D_0} = \frac{D^*}{\rho_0 c_0^2 w h^3} = \frac{2.25}{1.225 \times 340^2 \times 0.025 \times (0.1)^3} = 0.636.$$

From the results, it can be found that, when a honeycomb core with proper thickness and density is chosen, the bending stiffness can reach the desired range of (0.1,1). Therefore, it can be said that the honeycomb structure can satisfy the experimental requirements for both the low mass ratio and the high bending stiffness at the same time. And it also demonstrates that it is realistic to find a desired material for the experiment.

#### **4.5.2 Implementation in experiment**

According to the studies for the two-dimensional model, the non-uniform plate with two thinner fixed edges has a good performance. Therefore, a two-dimensional experiment with a non-uniform honeycomb structure is conducted. The honeycomb structure is composed of a 5mm-thick Nomex honeycomb core and two 0.025mm-thick aluminum facesheets. To prepare for the non-uniform shape, the portion of the Nomex honeycomb core near the two fixed edges is abraded to half of the thickness of the middle thicker part. The aluminum membrane is glued to the abraded non-uniform honeycomb core using the epoxy resin, and finally makes a finished honeycomb structure, whose configuration and dimensions are shown in Figure 4.18. The finished non-uniform honeycomb plate

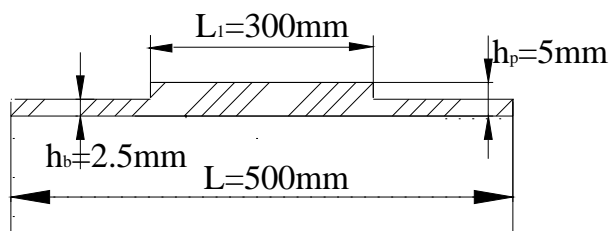


Figure 4.18: The configuration and dimensions of the non-uniform Nomex honeycomb structure

has a density of  $\rho^* = 147.6 \text{ kg/m}^3$ , and the corresponding dimensionless density is  $\rho = \rho^* / \rho_0^* = 147.6 / 1.225 = 120 \text{ kg/m}^3$ . The measured bending stiffness of the honeycomb plate is  $D^* = 1.48$ , with the corresponding value

$$D = \frac{D^*}{D_0} = \frac{D^*}{\rho_0 c_0^2 h^4} = \frac{1.48}{1.225 * 340^2 * (0.1)^4} = 0.105.$$

The two-dimensional experiment using the non-uniform honeycomb plate has the same measurement methodology as that of the former experiments described in the preceding sections. Figure 4.19 shows the results. Figure 4.19(a) shows the measured transmission loss spectrum. There is no sharp peak in the low-frequency region, and the curve resembles the  $TL$  of an expansion chamber. Also as shown Figure 4.19(b), which describes the curve of the relative reflection coefficient, the shape is also similar to that of the expansion chamber. The similarities of the

---

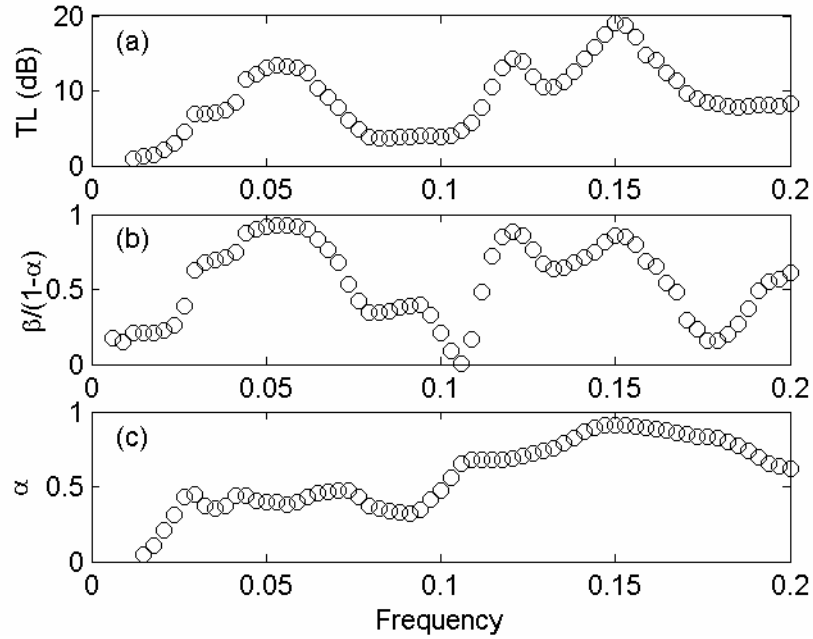


Figure 4.19: The experimental results of two-dimensional model using a non-uniform honeycomb structure.

Results between the non-uniform honeycomb plate and the expansion chamber are essentially caused by the significant acoustic leakage. In the two-dimensional experiment, the effect of the gap is difficult to be eliminated. Moreover, because the vertical surfaces of the plate, perpendicular to the upper and lower surfaces facing the duct and cavity, are not covered by facesheets, the hexagonal cores are exposed to the air, making these surfaces a corrugated configuration. These corrugated surfaces, whose effect is also like that of the gap, always deteriorate the acoustic leakage, which is fatal to the performance of the plate-type wave reflector.

---

Therefore, although the honeycomb structure satisfies the experimental requirements, it still needs further improvement to reduce the influence of the acoustic leakage.

## **Chapter 5: Conclusions and future work**

### **5.1 Conclusions**

In the thesis, both numerical study using finite element and experimental study have been carried out to investigate the performance of the plate-type wave reflector. The plate-type wave reflector shares the same mechanism, sound reflection mechanism, with the drum-like silencer. But different from the drum-like silencer, the plate-type wave reflector uses the bending stiffness of the plate as the restoration force instead of the tension applied on the membrane, and hence overcomes some disadvantages of the drum-like silencer. The theoretical studies also show that the new silencer can achieve an even wider stopband in the low-frequency region.

In the numerical study, a coupled system, including an acoustics domain (duct and cavity) and a structural-mechanics domain (plate), is analyzed to obtain the performances of the plate with different boundary conditions. Two different two-dimensional models, mindlin-plate model and plane-stress model, are used. The performance of a plate with simply-supported boundaries, simulated in the mindlin-plate model, is compared with that of a plate with clamped boundaries, simulated in the plane-stress model, and the comparison shows that the former has a wider stopband. This is because the simply-supported boundary condition gives

---

less restriction on the portion of the plate near the edges. However, due to the difficulties in implementing the simply-supported boundary condition in practice, a new plate model, non-uniform plate with clamped edges, is introduced to approximate the performance of a simply-supported uniform plate. For the non-uniform plate, its thickness at the clamped edges is reduced, which greatly enhances its capability in sound reflection. Parametric studies, basing on the same density, show that by changing the length of the two thinner ends, four well-connected peaks appear in the low-frequency region, producing a wide stopband. Modal analysis is conducted for both the simply-supported uniform plate and the clamped non-uniform plate. It shows that the peaks within the stopband normally appear at the frequency where there is no interference between the even modes and the odd modes of the in-vacuo plate vibration. The energy flux of the sound reflected by the odd modes is simply added to that from the even modes.

In the three-dimensional model, numerical simulation is conducted about the leakage effect of the gap between the plate and the lateral duct walls, and the results show that if the gap size is smaller than about 0.5% of the duct width, its effect on the transmission loss is insignificant. Otherwise, serious leakage will lead to a fatal damage to the performance of the plate, making the result resemble an expansion chamber. To minimize the effect of lateral bending stiffness of the plate, two non-uniform plates are tested. Both have non-uniform thickness in the longitudinal direction, but one has uniform thickness in the lateral direction and

---

another is non-uniform in the lateral direction. Results show that neither of them has good performance, and it essentially results from the effect of the lateral bending stiffness of the plate.

To validate the theoretical models, experimental studies for both two-dimensional and three-dimensional models are conducted using a 3mm-thick uniform foam. Two methods, static method and dynamic method, are used to obtain the properties of the foam. The four-microphone, two-load method is used for the transmission loss measurement. The experimental results show that the performances of the 3mm-thick foam are not as satisfactory as the optimal theoretical predictions, and this is because the plate does not conform to the optimal parameters predicted by the theory. However, the experimental results do validate the theoretical findings corresponding to the actual material properties. Besides, experiments are also conducted for the two-dimensional model with the non-uniform Nomex honeycomb structure. The experimental results for the material properties show that its mass ratio and bending stiffness are both within the desired range, which means that the optimal material for the two-dimensional model is realistic. However, because of the difficulties in controlling the gap size, the measured transmission loss spectrum is like an expansion chamber, which is also in agreement with the former theoretical results.

## **5.2 Future work**

In the present studies, two models, two-dimensional model and three-dimensional model are introduced and studied.

In the two-dimensional model, the material/structure with low mass ratio but high bending stiffness is preferred. As described in the former sections, the Nomex honeycomb structure is a good choice for the practical implementation. However, to get a good performance, further modifications need to be done to the two free longitudinal edges to reduce the acoustic leakage caused by the unavoidable gap.

The three-dimensional model is easier to implement in practice. However, because it has the four fixed edges, the performance of the plate is greatly reduced by the negative effect of the lateral bending stiffness. To overcome this drawback, a sandwich plate with a corrugated core can be used in the future implementation. The shape of the plate can be modified with four thinner edges, and all the four edges are fixed since the lateral bending stiffness of the plate with corrugated core is negligible.

## References

- [1] Abe A., Kobayashi Y., Yamada, G. (1998). "Analysis of subharmonic resonance of moderately thick antisymmetric angle-ply laminated plates by using method of multiple scales," *Journal of Sound and Vibration* **217**, 467-484.
- [2] Chapman C. J., Sorokin S. V. (2005). "The forced vibration of an elastic plate under significant fluid loading," *Journal of Sound and Vibration* **281**, 719-741.
- [3] Cheng L. (1994). "Fluid-structural coupling of a plate-ended cylindrical shell: vibration and internal sound field," *Journal of Sound and Vibration* **174**, 641-654.
- [4] Choy Y. S., Huang L. (2002). "Experimental studies of a drumlike silencer," *Journal of the Acoustical Society of America* **112**, 2026-2035.
- [5] Doak P. E. (1973). "Excitation, transmission and radiation of sound from source distributions in hard-walled ducts of finite length (I): the effects of duct cross-section geometry and source distribution space-time pattern," *Journal of Sound and Vibration* **31**, 1-72.
- [6] Dowling A. P., J. E., Ffowes Williams (1993). *Sound and sources of sound* (Chichester: E. Horwood ; New York : Halsted Press).
- [7] Frendi A. (1994). "Coupling between plate vibration and acoustic radiation," *Journal of Sound and Vibration* **177**, 207-226.

- [8] Frommhold W., Fuchs H.V., Sheng S. (1994). "Acoustic performance of membrane absorbers," *Journal of Sound and Vibration* **170**, 621-636.
- [9] Fuchs, H. V. , Zha, X. (1995). "Application of micro-perforated plates as sound absorbers with inherent damping ," *Acustica* **81**, 107-116.
- [10] Gardonio P., Elliott S. J. (2000). "Passive and active isolation of structural vibration transmission between two plates connected by a set of mounts," *Journal of Sound and Vibration* **237**, 483-511.
- [11] Kang J., Fuchs H. V. (1999). "Predicting the absorption of open weave textiles and micro-perforated membranes backed by an air space," *Journal of Sound and Vibration* **220**, 905-920.
- [12] Haradine M., Birch T., Stevens J., Sheawood C. (1997). "A micro- machined loudspeaker for the hearing impaired," *Transducers'97, Chicago*, 429-432.
- [13] Hsieh W., Hsu T., Tai Y. (1997). "A micromachined thin-film Teflon Electret microphone," *Transducer'97, Chicago*, 425-428.
- [14] Horoshenkova K.V., Sakagami K. (2001). "A method to calculate the acoustic response of a thin, baffled, simply supported poroelastic plate," *Journal of the Acoustical Society of America* **110**, 904-917.
- [15] Howe M. S. (1994). "Structural and acoustic noise generated by turbulent flow over the edge of a coated section of an elastic plate," *Journal of Sound and Vibration* **176**, 1-18.
- [16] Huang L. (1999). "A theoretical study of duct noise control by flexible panels," *Journal of the Acoustical Society of America* **106**, 1801-1809.
-

- [17] Huang L. (2000). "A theory of reactive control of low-frequency duct noise," *Journal of Sound and Vibration* **238**, 575-594.
- [18] Huang L. (2002). "Modal analysis of a drumlike silencer," *Journal of the Acoustical Society of America* **112**, 2014-2025.
- [19] Huang L. (2004). "Parametric study of a drum-like silencer," *Journal of Sound and Vibration* **269**, 467-488.
- [20] Huang L., Choy Y. S. (2005). "Vibroacoustics of three-dimensional drum silencer," *Journal of the Acoustical Society of America*, to appear in vol. **118**(4).
- [21] Lau, J. H. (1981). "Stiffness of corrugated plate," *J. Eng. Mech.* **107**, 271-275.
- [22] Konishi Satoshi, Yoda Mitsuhiro, Sugiyama Susumu, Akishita Sadao (2000). "Tunable acoustic absorber using a micro acoustic hole array," *Electronics and Communications in Japan Part 2* **83**, 1-6.
- [23] Lee Hyeongill, Singh Rajendra (2005). "Acoustic radiation from out-of-plane modes of an annular disk using thin and thick plate theories," *Journal of Sound and Vibration* **282**, 313-339.
- [24] Lee Joong-Kuen, Kim Jaehwan, Rhee Chool-Jae, Jo Chul-Hee, Choi Seung-Bok (2002). "Noise reduction of passive and active hybrid panels," *Smart Materials and Structures* **11**, 940-946.
- [25] Lighthill M. J. (1978). *Waves in Fluids* (Cambridge U.P., Cambridge).
-

- [26] Maa, Dah-You (1998). "Potential of microperforated panel absorber," *Journal of Acoustical Society of America* **104**, 2861-2866.
- [27] Meunier S., Habault D., Canevet G. (2001). "Auditory evaluation of sound signals radiated by a vibrating surface," *Journal of Sound and Vibration* **247**, 897-915.
- [28] Michishita Kazutoshi, Sakagami Kimihiro, Morimoto Masayuki, Svensson U. Peter (2000). "Sound radiation from an unbaffled elastic plate strip of infinite length," *Applied Acoustics* **61**, 45-63.
- [29] Munjal M. L. (1987). *Acoustics of ducts and Mufflers* (Wiley, New York).
- [30] Munjal, M. L., Doige, A. G. (1990). "Theory of a two source-location method for direct experimental evaluation of the four-pole parameters of an aeroacoustic element," *Journal of Sound and Vibration* **141**, 323-333.
- [31] Richard A. Shimansky, Milind M. Lele (1995). "Transverse stiffness of a sinusoidally corrugated plate," *Mech. Struct. & Mach.* **23**, 439-451.
- [32] Sakagami Kimihiro, Kiyama Masakazu, Morimoto Masayuki, Takahashi Daiji (1996). "Sound absorption of a cavity-backed membrane: a step towards design method for membrane-type absorbers," *Applied Acoustics* **49**, 237-247.
- [33] Sakagami K.; Nakanishi, S.; Daido, M.; Morimoto, M.; Takahashi, D. (1997). "Reflection of a spherical sound wave by an infinite elastic plate with an air-back cavity," *Acta Acustica (Stuttgart)* **83**, 963-971.
-

- [34] Sgard Franck, Atalla Nouredine, Amedin Celse Kafui (2003). “Vibro-acoustic behavior of a plate coated with an heterogeneous porous material radiating in a rigid walled cavity,” *Acta Acustica (Stuttgart)* **89**, S55.
- [35] Shou Kaneda, Qiang Yu, Masaki Shiratori, Keiichi Motoyama (2003). “Structural design optimization for reducing sound radiation from a vibrating plate using a Genetic Algorithm”, *JSME International Journal, Series C: Mechanical Systems, Machine Elements and Manufacturing* **46**, 1000-1009.
- [36] Takahashi D., Tanaka M. (2002). “Flexural vibration of perforated plates and porous elastic materials under acoustic loading,” *Acoustical Society of America* **112**, 1456-1464.
- [37] Tang Wing Cheong, Lin Wei Zheng (2003). “Stiff light composite panels for duct noise reduction,” *Applied Acoustics* **64**, 511-524.
- [38] Tu Y., Fuller C. R. (2000). “Multiple reference feedforward active noise control Part II: reference preprocessing and experimental results,” *Journal of Sound and Vibration* **233**, 761-774.
- [39] Troitsky, M. S. (1976). *Stiffened Plates* (Elsevier Scientific Publishing Co.).
- [40] Yairi Motoki , Sakagami Kimihiro, Sakagami Eiji, Morimoto Masayuki, Minemura Atsuo, Andow Kei (2002). “Sound radiation from a double-leaf elastic plate with a point force excitation: Effect of an interior panel on the structure-borne sound radiation,” *Applied Acoustics* **63**, 737-757.

itemsborrowedbyFYP06.doc

To Alex Yeung & Co-workers (Feb. 2006)

Item#	Description	Returned?	R signed by T
1	T T/C with plug 1 no.		
2	T/C extension cords no.		
3	Omega Temperature Controller Set 1 no.		
4	13 A Electrical Earth Trip Set 1 no.		
5	CA flexible hose (home-made) 1 no.		
6	CA flexible hose 1 no.		
7			
8			
9			
10			
11			
12			
13			
14			
15			
16			
17			
18			
19			
20			
21			
22			
23			
24			
25			

Borrower Signature:

Date: